AD-A111 413 ADVISORY GROUP FOR AEROSPACE RESEARCH AND DEVELOPMENT--ETC F/G 4/1
MODELING THE LOWEST 1 KM OF THE ATMOSPHERE,(U)
NOV 81 W S LEWELLEN
UNCLASSIFIED AGARD-AG-267 NL

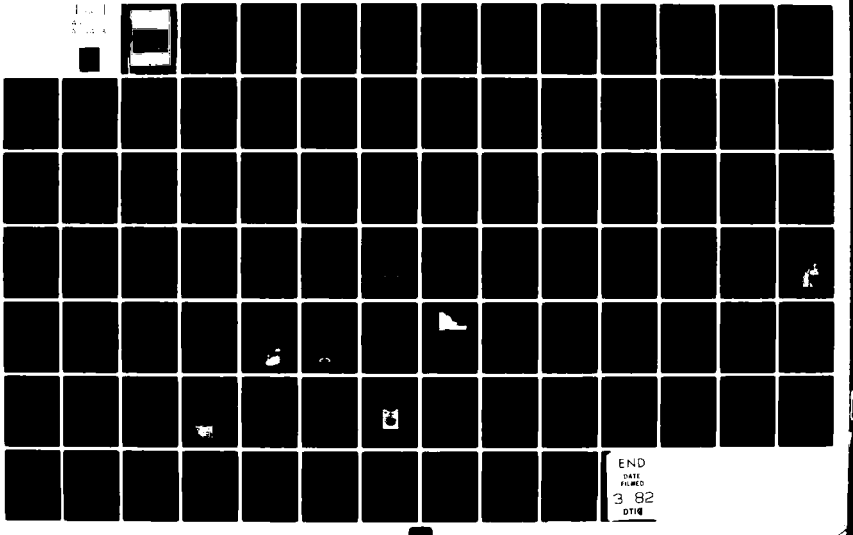

END
DATE FILMED
3 82
DTIC

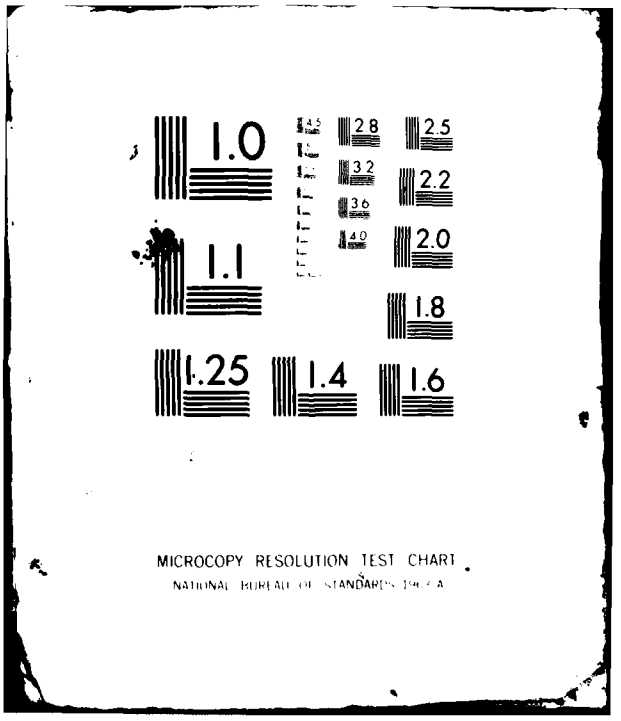
1.0
1.1
1.25
1.4
1.6
1.8
2.0
2.2
2.5
2.8
3.2
3.6
4.0
MICROCOPY RESOLUTION TEST CHART
NATIONAL BUREAU OF STANDARDS 1963-A

AGARDograph No. 267

Modeling the Lowest 1Km of the Atmosphere

NORTH ATLANTIC TREATY ORGANIZATION

ADVISORY GROUP FOR AEROSPACE RESEARCH AND DEVELOPMENT

(ORGANISATION DU TRAITE DE L'ATLANTIQUE NORD)

AGARDograph No.267

MODELING THE LOWEST 1 KM OF THE ATMOSPHERE

by

W.S.Lewellen
Aeronautical Research Associates of Princeton, Inc.
50 Washington Road, P.O. Box 2229
Princeton, New Jersey 08540
USA

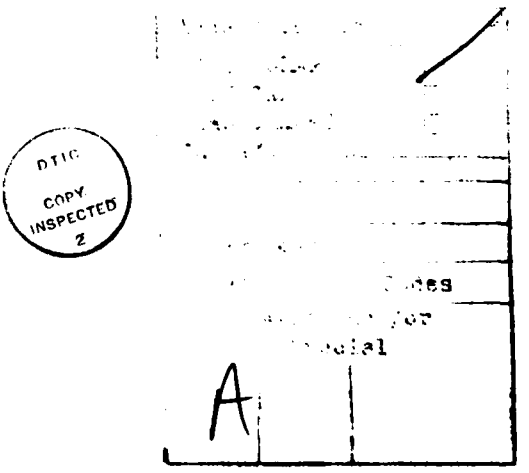

This AGARDograph was prepared at the request of the Fluid Dynamics Panel of AGARD.

THE MISSION OF AGARD

The mission of AGARD is to bring together the leading personalities of the NATO nations in the fields of science and technology relating to aerospace for the following purposes:

- Exchanging of scientific and technical information;
- Continuously stimulating advances in the aerospace sciences relevant to strengthening the common defence posture;
- Improving the co-operation among member nations in aerospace research and development;
- Providing scientific and technical advice and assistance to the North Atlantic Military Committee in the field of aerospace research and development;
- Rendering scientific and technical assistance, as requested, to other NATO bodies and to member nations in connection with research and development problems in the aerospace field;
- Providing assistance to member nations for the purpose of increasing their scientific and technical potential;
- Recommending effective ways for the member nations to use their research and development capabilities for the common benefit of the NATO community.

The highest authority within AGARD is the National Delegates Board consisting of officially appointed senior representatives from each member nation. The mission of AGARD is carried out through the Panels which are composed of experts appointed by the National Delegates, the Consultant and Exchange Programme and the Aerospace Applications Studies Programme. The results of AGARD work are reported to the member nations and the NATO Authorities through the AGARD series of publications of which this is one.

Participation in AGARD activities is by invitation only and is normally limited to citizens of the NATO nations.

Published November 1981

ISBN 92-835-1407-6

Printed by Technical Editing and Reproduction Ltd
Harford House, 7–9 Charlotte St, London, W1P 1HD

FOREWORD

This monograph provides a review of the state of the art of modeling the important processes of the transport of mass, momentum, and energy through the lower atmosphere from the personal perspective of one involved in turbulent transport modeling. No historical perspective of the vast literature published on this subject is attempted. Much of our understanding of atmospheric boundary-layer processes has come from careful observation. For a review of observational methods and programs, the reader is referred to the recent monograph by McBean, et al. (1979). The monograph also provides a very useful review of atmospheric-boundary-layer models. I use this fact, plus the existence of the books by Brown (1974), Plate (1971), Wipperman (1973), Longhetto (1980), and the AMS workshop proceedings edited by Haugen (1973) and by Wyngaard (1980), as justification for further specialization of this review to deal specifically with models having a basic theoretical foundation in turbulent transport modeling. Data and the results of other types of models will only be included herein to the extent that I feel they help to place the results of turbulent transport modeling in perspective.

The goal of this monograph is to describe the approach of turbulent transport modeling to low-level atmospheric dynamics in sufficient detail to permit a researcher to follow this route, to review the status of our current understanding of boundary-layer meteorology, and to describe some of the applications where turbulent transport modeling can be expected to have an important impact in the near future.

I wish to thank AGARD for this opportunity to organize my thoughts on modeling low-level atmospheric turbulence, and to acknowledge the following US Government Agencies; the Naval Air Systems Command, the Office of Naval Research, the Nuclear Regulatory Commission, the Environmental Protection Agency, and the National Aeronautics and Space Administration; and the Electric Power Research Institute for their original support of my personal work and that of my A.R.A.P. colleagues in this area over the past few years. Naturally, most of the examples covered in detail in this review are based on this work. I apologize to other boundary-layer modelers for not having worked harder to cover their work to the same depth.

CONTENTS

	Page
FOREWORD	iii
ABSTRACT and NOMENCLATURE	v
I. INTRODUCTION	1
II. MODEL FORMULATION	
2.1 Basic Equations	3
2.2 Approximate Scaling Relationships	4
2.3 Turbulence Closure	6
Dissipation Terms	7
Pressure Correlations	8
Third-Order Velocity Correlations	9
Modeled Equations	9
Scale Determination	10
III. SIMILARITY RELATIONSHIPS	
3.1 Monin-Obukhov Scaling in the Surface Layer	13
3.2 Neutral, Steady-State, PBL Scaling	15
3.3 Convectively Mixed Layer Scaling	17
3.4 The Stable Ekman Boundary Layer	21
3.5 Stability Variations	24
3.6 Flow within a Surface Canopy	25
IV. INTERACTION OF TURBULENT TRANSPORT WITH OTHER PHYSICAL MECHANISMS	
4.1 Diurnal Variations in the Planetary Boundary Layer	28
4.2 Influence of Baroclinicity	31
4.3 The Marine Boundary Layer	33
4.4 Moisture Change of Phase	34
4.5 Thermal Radiation	38
4.6 Fog	39
4.7 Boundary Layer with Stratus Cloud	42
V. ORGANIZED FEATURES WITHIN THE ATMOSPHERIC BOUNDARY LAYER	
5.1 Flow Over an Abrupt Change in Surface Conditions	46
5.2 Longitudinal Roll Vortices	47
5.3 The Thunderstorm Downdraft and Associated Gust Front	53
5.4 Tornado Boundary Layer	55
VI. EXAMPLE APPLICATIONS OF PARTICULAR INTEREST	
6.1 Dispersal of Industrial Plumes	59
6.2 Wind Shear Around Airports	62
6.3 Refractive Index Fluctuations	66
6.4 Dry Deposition	68
VII. CONCLUDING REMARKS	74
REFERENCES	75

Modeling the Lowest 1 Km of the Atmosphere

W.S. Lewellen
Aeronautical Research Associates of Princeton, Inc.
50 Washington Road, P.O. Box 2229
Princeton, New Jersey 08540

ABSTRACT

The interdependence between the turbulent transport of mass, momentum, and energy through the lower levels of the atmosphere, and the distribution of wind, temperature, and species within this layer are reviewed. Particular emphasis is placed on models, either analytical or numerical, which have a basic theoretical foundation in turbulent transport modeling. The results of example model solutions are used to discuss such micrometeorological problems as: wind shear and turbulence around airports; the prediction of low-level clouds and fog; the dispersion of industrial pollutants; the interaction of electromagnetic radiation with turbulent fluctuations in humidity and temperature; and the evolution of organized features within the boundary layer.

NOMENCLATURE

A	Model coefficient, see Eqs. (2.3.12 and 2.3.13)
b	Model coefficient, see Eq. (2.3.15)
C	Mean species concentration
c	Species fluctuation
C_p	Specific heat at constant pressure
d	Proportionality factor in Eq. 6.1.10
F_j	General force vector per unit mass
F^+, F^-	Upward and downward thermal radiation fluxes
f	Coriolis parameter due to earth's rotation
g	Gravitational acceleration
H	Mean value of mixing ratio of water to air
h	Fluctuation of water mixing ratio
H_ℓ, h_ℓ	Mean and fluctuating value of liquid water mixing ratio
H_s, h_s	Mean and fluctuating value of saturated water mixing ratio
H_v, h_v	Mean and fluctuating value of water vapor mixing ratio
H_*	Measure of the surface moisture flux, $\overline{wh}/U_*$
H_c	Height of vegetation canopy
k	Thermal conductivity
k_c	Species diffusivity
K,K_H	Effective eddy thermal diffusivity
K_E	Effective eddy diffusivity for moisture
K_g, K_s	Coefficients in the moist air model, see Eqs. (4.4.6 and 4.4.7)
L	Monin-Obukhov length
ℓ	Eddy viscosity length scale, see Eq. (2.3.1)
$\mathcal{L}$	Latent heat of vaporization
M	Baroclinic parameter, see Eq. (4.2.4)
P	Mean pressure
p	Pressure fluctuation
Q_θ	Heat source per unit mass
Q_c	Species source per unit mass
q	Root-mean square velocity fluctuation
R	Universal gas constant
Ri	Richardson number
R_v	Gas constant for water vapor
Ro	Rossby number
r	Radius
$\hat{r}$	Radius at which maximum swirl occurs
s	Model coefficient in the dissipation of temperature variance
T_o	Referenced background absolute temperature
t	Time
U_i, U_j, U_k	Mean velocity components
u_i, u_j, u_k	Fluctuating velocity components

U_g	Geostrophic wind
u_*	Friction velocity
U	Mean longitudinal velocity
u	Fluctuating longitudinal velocity
V	Mean transverse velocity
v	Fluctuating transverse velocity
W	Mean vertical velocity
w	Fluctuating vertical velocity
w_*	Characteristic velocity for free convection
x,y	Horizontal coordinates
z	Vertical coordinate
z_i	Height of mixed layer
z_o	Surface roughness height
α	Angle between the roll axis and the geostrophic wind
β	Volummetric expansion of fluid per unit increase in temperature
β_r	Radiation diffusivity factor
β_Γ	Logarithmic derivative of the saturation mixing ratio with respect to temperature
β_o	Derivative of the saturation curve with respect to θ_s, or direction of the geostrophic wind shear
γ	Temperature lapse rate
δ	Boundary layer thickness
δ_{ij}	Kronecker delta
ε	Rate of dissipation of turbulent kinetic energy
ε_{ijK}	Alternating tensor
Θ	Mean potential temperature
θ	Potential temperature fluctuation
θ_ℓ	Liquid potential temperature, see Eq. (4.4.1)
θ_s	Moist static energy, see Eq. (4.4.2)
θ_v	Virtual potential temperature, see Eq. (4.4.3)
θ_*	$-\overline{w\theta}/U_*$
κ	Von Karman's constant
Λ	Turbulent macroscale
λ	Wavelength of longitudinal vortex roll
μ	Stability parameter = U_*/fL
ν	Kinematic viscosity
ρ	Density
Σ	Radiation source function
$\hat{\sigma}$	Stefan-Boltzmann constant
σ_r	Spread of a plume as defined in Eq. (6.6.1)
σ_u	Root mean square variation of longitudinal wind velocity
σ_v	Root mean square variation of transverse wind velocity
σ_w	Root mean square variation of vertical wind velocity
σ_θ	Root mean square variation of the potential temperature
τ	Radiation transmission function
τ_v	Particle relaxation time
ϕ	Dimensionless wind shear in the surface layer
ϕ_H	Dimensionless temperature gradient in the surface layer
ψ	Stream function
Ω	Earth's rotation
ω	Frequency of pressure changes imposed on the boundary layer

I. Introduction

The processes of the transport of mass, momentum and energy through the lower atmosphere are of extreme importance to a large number of man's activities. Perhaps the most basic necessity of life for any species is the requirement of providing some means of energy flow through the individual members of that species. A majority of the species of life on earth depend upon motions in the lower levels of the atmosphere to provide for at least some part of either the input to the individual or the disposal of waste from it. This observation remains true for a majority of the machines invented by man. Thus, some model of motions in this part of the atmosphere is of interest to a variety of disciplines.

As a result of the widespread interest, a vast amount of literature has been published on this subject. No attempt will be made to review, even a reasonable sampling of this literature. Rather, we start by recognizing that it is the small scale turbulent motions which generally play the dominant role in interchanging mass, momentum, or energy between a surface and the air above or around it. The central problem has been to develop a viable means of modeling turbulent transport. Due to the wide range of scales involved, there is no rigorous, theoretical solution for turbulent flow. Turbulent transport models are a blend of scaling based on the physical conservation laws and empiricism. Also, it appears that the modeler frequently needs to apply a little art to cover the holes in the science.

The governing conservation equations for the turbulent transport of mass, momentum, and energy will be discussed and the turbulence closure problem reviewed. Emphasis is placed on second-order closure modeling, because I believe that this provides a firm physical framework for extending the empirical information gained from select experiments to much more general problems. While it is true that much, perhaps even most, of our present understanding of dynamics in the atmospheric boundary layer has come from simpler scaling laws applied to reliable field data, I believe that second-order closure has in recent years demonstrated that it will have a major impact on solving those problems where the turbulent fluxes or turbulent variances are the quantities of most interest. A rough review of the scales of the boundary-layer thickness over which the strongest interaction between the surface and the atmosphere occur is also given in Chapter 2. This monograph is entitled "Modeling the Lowest 1 Km of the Atmosphere", to emphasize that this is the region of most concern to us. However, the scaling analysis in the next chapter makes it evident that the turbulent boundary layer generated from the surface may exceed 1 Km in thickness under certain conditions and be much less than 1 Km under other conditions. In fact, under the conditions most often occurring in nature, there may be a number of layers governed by different dynamical behaviors superimposed at any one time. In discussing these idealized layers, we will deal with the complete layer, but keep in mind that we are most interested in that portion of the layer which falls within 1 Km height.

Next, we look in detail at some of the separate balances which can permit ideal similarity laws to exist in at least a portion of the lowest 1 Km altitude. The first of these is the surface layer which may only extend up a few meters or as much as a few hundred meters. It is these surface-layer, Monin-Obukhov, similarity laws which provide the most reliable information in current widespread use in micrometeorology. The assumptions necessary for validity of the surface layer functions are often fulfilled. This is not so often true of the other ideally similar layers. However, they do form a basis for our understanding the different types of dynamics which the lower atmosphere will support. In particular, they clearly show the role of the coriolis force in turning the wind vector through a significant angle within this height domain, the role of heat transfer between the surface and the atmosphere in either amplifying or damping the turbulence generated by the moving wind over the stationary surface, and the role of the structure of the surface canopy in defining the detailed interaction between the surface and the atmosphere. From these ideal similarity laws it is clear that, not only do the wind, temperature, and species control the interchange of mass, momentum, and energy between the surface and atmosphere, but it is just as valid to view the surface fluxes of mass (in the form of water vapor), momentum, and energy as predominantly controlling the motions of the atmosphere in the lowest 1 Km. These similarity laws have formed the basis for most of the currently used engineering methods for estimating such things as: the surface drag, the angle the wind at the surface departs from the direction of the wind at the top of the boundary layer, wind shear within this layer, surface heat transfer, and water evaporation from the surface.

In the real world, the interaction of turbulent transfer with other physical mechanisms modifies the limiting similarity solutions. Typical time variations of the surface heat transfer caused by the diurnal solar radiation delivered to the land drive the boundary layer between the strongly stable nocturnal layer and the buoyantly driven, well-mixed layer of the afternoon. A strong hysteresis effect exists with the morning "neutral" boundary layer quite distinct from the evening "neutral" layer. Other effects, such as small horizontal variations in temperature, of the order of 1°C per 100 Km, lead to important baroclinic gradients in the wind. Example calculations showing the influence of typical unsteady and spatial variability demonstrate that the steady state, spatially homogeneous, neutral planetary boundary layer seldom comes close to being realized in nature.

The lowest 1 Km of the atmosphere plays a key role in controlling the cycling of water through the atmosphere. On a global average basis, the turbulent transport of water vapor through this atmospheric layer must balance the average precipitation of liquid water, about 1 m per year (Coantic, 1978). While it is the small scale turbulent eddies which drive the transport of water vapor through the boundary layer, it is the release of latent energy transported with the water vapor which is responsible for fueling most of the larger scale atmospheric motions. These larger, synoptic scale meteorological motions are not analyzed herein, but instead are treated as boundary conditions at the top of the boundary layer. Latent energy release within the boundary layer in the form of low-level clouds or fog also directly affects the structure of the wind and temperature in this layer.

An indirect, but often even stronger, influence of condensed water vapor in the boundary layer is its interaction with thermal radiation. On the global scale, the energy to drive the atmosphere ultimately

traces back to the sun, with thermal radiation the principal mode of energy transfer through the atmosphere. Under clear conditions, the relative transparency of the atmosphere allows this radiant energy to pass through the lowest 1 Km without significant interaction. However, the presence of condensed water droplets in the air greatly reduces thermal radiation absorption depths and permits a strong interaction between turbulent transport and thermal radiation. Thus, the influence of thermal radiation must be incorporated in any boundary-layer model which seeks to simulate low-level cloudiness or fog.

The vertical variations normal to the surface are generally of most concern in modeling fluxes between the surface and the atmosphere, but the boundary layer contains a rich variety of three-dimensional flow features which are of increasing interest. In simulating the boundary layer it is necessary to decide when to seek to resolve particular features rather than to ensemble average over them as part of the turbulence. Chapter 5 considers a number of particular features involving two-dimensional symmetry, either planar or axisymmetric. Simulations of these features are computed by incorporating the boundary conditions for this particular 2-D feature into the boundary conditions for the mean variable while representing the smaller scale three-dimensional eddies with the turbulence closure modeling. The features simulated vary from a simple step change in surface roughness conditions, to the most violent eddy which occurs in nature, the tornado.

The simulation of the common longitudinal roll vortices which extend the full height of the boundary layer provide an opportunity to examine the relative contributions of the smaller scale random turbulence and the organized large scale rolls. Both play an important role in transporting mass, momentum, and energy through the lowest 1 Km of the atmosphere.

In particular engineering applications, it is generally desirable to work with the simplest model which provides a reliable answer to the question at hand. In Chapter 6, several particular applications are discussed which provide examples where the turbulent fluxes and variances are the quantities of most concern. This provides a sampling of areas where the relatively complex turbulent transport modeling reviewed herein is currently making contributions to engineering problems. The list is not intended to be all inclusive, rather an attempt was made to describe each individual application in sufficient detail to make it useful to the interested reader.

II. Model Formulation

2.1. Basic Equations

The basic equations governing the transport of mass, momentum, and energy in the atmospheric boundary layer have been well known for some time. They may be written as:

Mass continuity:
$$\frac{\partial U_i}{\partial x_i} = 0 \tag{2.1.1}$$

Momentum:
$$\frac{\partial U_i}{\partial t} + U_j \frac{\partial U_i}{\partial x_j} = -\frac{1}{\rho}\frac{\partial p}{\partial x_i} + F_i + \frac{\partial}{\partial x_j}\left(\nu \frac{\partial U_i}{\partial x_j}\right) \tag{2.1.2}$$

Energy:
$$\frac{\partial \theta}{\partial t} + U_j \frac{\partial \theta}{\partial x_j} = \frac{\partial}{\partial x_j}\left(k \frac{\partial \theta}{\partial x_j}\right) + Q_\theta \tag{2.1.3}$$

Species:
$$\frac{\partial C}{\partial t} + U_j \frac{\partial C}{\partial x_j} = \frac{\partial}{\partial x_j}\left(k_C \frac{\partial C}{\partial x_j}\right) + Q_C \tag{2.1.4}$$

The incompressible form of the continuity equation is appropriate for the atmosphere as long as we restrict attention to velocities much less than the speed of sound and to shallow convection, i.e., vertical motions which extend for a height much less than the scale height of the atmosphere. The most important effects of density changes in the boundary layer are those resulting in combination with gravity acceleration as first pointed out by Boussinesq (1903). This buoyant force term and the coriolis body force due to the earth's rotation are the primary terms which will be used in F_i. The source terms Q_θ and Q_C in the energy and species equations will generally be zero except for that due to thermal radiation flux divergence in Q_θ.

The temperature variable is chosen as the potential temperature

$$\theta = T - T_{ref} + \frac{g}{c_p} z \tag{2.1.5}$$

so that the temperature changes experienced by adiabatic expansion or compression accompanying vertical motions will be automatically incorporated.

The primary difficulty with Eqs. (2.1.1 - 2.1.4) is that although these equations may be solved rather straightforwardly with today's computing resources for simple boundary conditions, the large range of scales involved in the motions of the atmospheric boundary layer prohibits a complete detailed solution. Atmospheric motions range from small dissipative eddies, as small as 10^{-3} meters, to the synoptic weather features of order 10^6 meters. It appears essential to average over, at least, the lower end of this spectrum of scales. These smallest scale motions tend to be random in character and thus most susceptible to statistical analyses.

When Eqs. (2.1.1 - 2.1.4) are averaged over an ensemble of realizations the equations may be written as:

Mass continuity:
$$\frac{\partial U_i}{\partial x_i} = 0 \tag{2.1.6}$$

Momentum:
$$\frac{\partial U_i}{\partial t} + U_j \frac{\partial U_i}{\partial x_j} = -\frac{\partial \overline{u_i u_j}}{\partial x_j} + \frac{\partial}{\partial x_j}\left(\nu \frac{\partial U_i}{\partial x_j}\right) - \frac{1}{\rho}\frac{\partial P}{\partial x_i} + \beta g_i(\theta - \theta_0) - 2\varepsilon_{ijk}\omega_j U_k \tag{2.1.7}$$

Energy:
$$\frac{\partial \theta}{\partial t} + U_j \frac{\partial \theta}{\partial x_j} = -\frac{\partial \overline{u_j \theta}}{\partial x_j} + \frac{\partial}{\partial x_j}\left(k \frac{\partial \theta}{\partial x_j}\right) + Q_\theta \tag{2.1.8}$$

Species:
$$\frac{\partial C}{\partial t} + U_j \frac{\partial C}{\partial x_j} = -\frac{\partial \overline{u_j c}}{\partial x_j} + \frac{\partial}{\partial x_j}\left(k_C \frac{\partial C}{\partial x_j}\right) + Q_C \tag{2.1.9}$$

The dependent variables in Eqs. (2.1.6 - 2.1.9) have been split into an ensemble mean value, denoted by capitalization, representing the scales of motion to be resolved, and a fluctuating value, denoted by lower case symbols, representing the unresolved motions.

The price for averaging Eqs. (2.1.1 - 2.1.4) to reduce the range of scales to be resolved is high. Equations (2.1.6 - 2.1.9) do not form a complete set until the second-order correlations, $\overline{u_iu_j}$, $\overline{u_i\theta}$, and $\overline{u_ic}$ and $\overline{u_ic}$, can be determined or related to the mean variables. This is the central closure problem of turbulent transport theory. The larger the scales of motion included in the unresolved averages, the more sensitive the task of correctly relating the second-order correlations to the resolved flow field. On the other hand, the smaller the scales of motion included within the resolved motion, the more difficult the task of solving for this mean motion. The choice of the break between the resolved and unresolved scales calls for a compromise dictated by the particular application.

A closure scheme with general validity is highly desirable. A method of incorporating additional physical conservation relationships into the closure scheme is to begin with the equations for $\overline{u_iu_j}$, $\overline{u_i\theta}$, and $\overline{u_ic}$ derived from Eqs. (2.1.1 - 2.1.4). With the aid of Eqs. (2.1.6 - 2.1.9) and a fair amount of algebraic manipulation, these may be written as:

$$\frac{\partial \overline{u_iu_j}}{\partial t} + U_k \frac{\partial \overline{u_iu_j}}{\partial x_k} = - \overline{u_iu_k} \frac{\partial U_j}{\partial x_k} - \overline{u_ju_k} \frac{\partial U_i}{\partial x_k} + \beta g_i \overline{u_j\theta} + \beta g_j \overline{u_i\theta} - 2\epsilon_{ik\ell} \omega_k \overline{u_\ell u_j} - 2\epsilon_{jk\ell} \omega_\ell \overline{u_k u_i}$$

$$- \frac{\partial}{\partial x_k} (\overline{u_k u_i u_j}) - \overline{\frac{u_j}{\rho} \frac{\partial p}{\partial x_j}} - \overline{\frac{u_j}{\rho} \frac{\partial p}{\partial x_i}} + \nu \frac{\partial^2 \overline{u_iu_j}}{\partial x_k^2} - 2\nu \overline{\frac{\partial u_i}{\partial x_k} \frac{\partial u_j}{\partial x_k}} \qquad (2.1.10)$$

$$\frac{\partial \overline{u_i\theta}}{\partial t} + U_j \frac{\partial \overline{u_i\theta}}{\partial x_j} = - \overline{u_iu_j} \frac{\partial \theta}{\partial x_j} - \overline{u_j\theta} \frac{\partial U_i}{\partial x_j} + \beta g_i \overline{\theta^2} - 2\epsilon_{ijk} \omega_j \overline{u_k\theta}$$

$$- \frac{\partial \overline{u_iu_j\theta}}{\partial x_j} - \overline{\frac{\theta}{\rho} \frac{\partial p}{\partial x_i}} - \nu\theta \overline{\frac{\partial^2 u_i}{\partial x_j^2}} - k u_i \overline{\frac{\partial^2 \theta}{\partial x_j^2}} \qquad (2.1.11)$$

$$\frac{\partial \overline{u_ic}}{\partial t} + U_j \frac{\partial \overline{u_ic}}{\partial x_j} = - \overline{u_iu_j} \frac{\partial C}{\partial x_j} - \overline{u_jc} \frac{\partial U_i}{\partial x_j} + \beta g_i \overline{c\theta} - 2\epsilon_{ijk} \omega_j \overline{u_kc}$$

$$- \frac{\partial \overline{u_iu_jc}}{\partial x_j} - \overline{\frac{c}{\rho} \frac{\partial p}{\partial x_i}} - \nu c \overline{\frac{\partial^2 u_i}{\partial x_j^2}} - k_c u_i \overline{\frac{\partial^2 c}{\partial x_j^2}} \qquad (2.1.12)$$

As proposed by Lilly (1969) and Donaldson (1972, 1973), the physical constraints inherent within Eqs. (2.1.10 - 2.1.12) can provide strong guidelines for modeling turbulent transport in the atmosphere assuming the terms involving higher-order correlations can be represented in a consistent manner. A variety of models have been presented by researchers for closing the equations at this second order. Before proceeding to some of these models, let us discuss the scaling inherent in Eqs. (2.1.10 - 2.1.12) in order to outline the dependency of the boundary-layer thickness on the pertinent variables.

2.2. Approximate Scaling Relationships

When characteristic lengths L and δ, and characteristic velocities V and W are introduced for the horizontal and vertical components respectively, mass continuity, Eq. (2.1.6) shows that

$$W = O\left(\frac{\delta}{L} V\right) \qquad (2.2.1)$$

The further introduction of F for the characteristic body force, q for the characteristic turbulence velocity, and τ for the characteristic time, permits the momentum equation, Eq. (2.1.7), to be scaled as

$$\frac{V}{\tau} + \frac{V^2}{L} = O\left(F + \frac{q^2}{\delta}\right) \qquad (2.2.2)$$

To help interpret this equation, it is advantageous to add the Reynolds stress equation, Eq. (2.1.10)

$$\frac{q^2}{\tau} + \frac{Vq^2}{L} = O\left(\frac{q^2V}{\delta} + F_1 q - \frac{q^3}{\Lambda}\right) \tag{2.2.3}$$

A characteristic length Λ for the turbulence has been introduced into Eq. (2.2.3). It is reasonable to expect Λ to be some fraction of δ.

Equations (2.2.2) and (2.2.3) lead to a number of different possibilities. First, if the flow is steady and horizontally homogeneous, i.e., both z and $L \to \infty$, then from Eq. (2.2.2)

$$\delta \sim \frac{q^2}{F} \tag{2.2.4}$$

and from Eq. (2.2.3)

$$q \sim \frac{\Lambda V}{\delta} + \frac{F_1 \Lambda}{q} \tag{2.2.5}$$

If coriolis body forces are considered then $F \sim fV$, and thus

$$\delta \sim \left(\frac{\Lambda}{\delta}\right)^2 \frac{V}{f} \tag{2.2.6}$$

For typical values of $(\Lambda/\delta) \sim 0.1$, $V \sim 10$ m/sec, $f \sim 10^{-4}\text{sec}^{-1}$, this leads to $\delta \sim 1$ Km for the scale of the planetary boundary layer (PBL) under steady state, constant density, spatially homogeneous conditions. These ideal conditions seldom apply in the atmosphere.

Unsteady variations in F may be expected to reduce δ. For example, if the geostrophic wind is assumed to have a periodic variation with frequency ω, then the time scale should scale with ω^{-1} and Eq. (2.2.6) may be modified to

$$\delta \sim \left(\frac{\Lambda}{\delta}\right)^2 \frac{V}{(f+\omega)} \tag{2.2.7}$$

Thus the boundary layer associated with mesoscale features with time scales less than ≈ 3 hours, such as convective storms, should be expected to be thinner than the normal steady state values.

Small differences in air density also play a very important role through F_1 or F. If F_1 is taken to be order $g\Delta\theta/T_o$ while F remains order fV, then it appears possible to have

$$\delta \sim fV^3 \left(\frac{g\Delta\theta}{T_o}\right)^{-2} \tag{2.2.8}$$

It will be seen in Section 3.4 that this is appropriate for an equilibrium layer stabilized by negative buoyancy. In practice, this limit also appears to be only rarely reached. Instead, it is possible for Eq. (2.2.3) to balance on a shorter time scale than f^{-1}. In the stabilizing case, the boundary layer thickness determined by a balance of the 3 terms on the right-hand side of Eq. (2.2.3) is

$$\delta \sim \frac{\Lambda}{\delta} \frac{V^2 T_o}{g\Delta\theta} \tag{2.2.9}$$

In the unstable case, the last two terms in Eq. (2.2.3) attempt to balance, but if the lapse rate, $\partial\theta/\partial z$, remains negative, the turbulence will continue to grow unbounded. Under these conditions, Eq. (2.2.3) may be interpreted as only yielding the scale of q^2 for any δ,

$$q^2 \sim \frac{g\Delta\theta\delta}{T_o} \tag{2.2.10}$$

with δ growing compatibly with the mean potential temperature equation, Eq. (2.1.8), or more frequently limited by a capping stable temperature lapse rate.

When Eq. (2.2.9) is interpreted in terms of lapse rate, $\gamma \equiv \partial\theta/\partial z$, then

$$\delta \sim \left(\frac{\Lambda}{\delta}\,\frac{T_o}{g\gamma}\right)^{1/2} V \qquad (2.2.11)$$

Relatively small stable lapse rates ($\lambda\ 10^{-3}$°C/m) lead Eq. (2.2.11) to yield values of δ much lower than those obtained from Eq. (2.2.6). Under light wind conditions (~ 1 m/sec) and strong lapse rates (~ 10^{-1}°C/m), as may be set up in the early morning hours after a clear night of surface radiational cooling, δ can be as small as ~ 10 meters.

Spatial homogeneity, although still infrequent, is more readily obtained. It requires that

$$\frac{L}{\delta} \gg \frac{V^2}{q^2} \sim \left(\frac{\delta}{\Lambda}\right)^2 \sim 100 \qquad (2.2.12)$$

There are many places on earth where the surface is relatively homogeneous over distances of the order of 100 Km. A frequent obstruction to spatial homogeneity comes not from the surface roughness boundary conditions, but from thermal boundary conditions. Horizontal temperature gradients of the order of 1°C per 100 Km, or larger, lead to vertical variations in the pressure gradient driving the PBL which can significantly influence the flow. Likewise, horizontal variations in the free stream wind of the order of 1 m/sec per 100 Km which lead to horizontal divergence of the order of 10^{-5}sec^{-1} lead to vertical velocities of the order of 1 cm/sec at the top of the boundary layer. Although seemingly small, these vertical velocities are sufficiently large to have significant effects on the vertical gradients of velocity, temperature, and humidity at the top of the boundary layer.

As a way of summarizing the boundary layer scaling, it is possible to combine the previous equations in an approximate fashion and write

$$\delta \sim \frac{(\Lambda/\delta)^2 V}{[f + \omega + (\Lambda/\delta)^{3/2}\,(g\gamma/T_o)^{1/2} + V/L]} \qquad (2.2.13)$$

Whichever of the frequencies is largest; the coriolis f, the unsteadiness in the geostrophic winds ω, the frequency of the stable oscillations, $(\Lambda/\delta)^{3/2}(\gamma g/T_o)^{1/2}$, related to the Brunt-Vaisala frequency, or the frequency associated with the spatial inhomogeneity, V/L, will control the boundary layer thickness. If the density stratification is locally unstable, then δ will increase until it is capped by a stable layer. Although the largest frequency may be expected to control the thickness over which the strongest adjustments between surface and free stream conditions occur, in nature we can expect these thin adjustment layers to coexist in the form of young shallow boundary layers occurring within older deeper layers.

2.3. *Turbulence Closure*

A complete review of the various approximations used by different researchers to close the set of equations given in Section 2.1 is beyond the scope of this monograph. Some reviews of this subject appearing in the literature are those by Mellor and Herring (1973), Reynolds (1976), Lewellen (1977), Lumley (1979, 1980), Launder, et al. (1975), and Zeman (1981). It currently remains an area of active research. What I will attempt to do is provide a flavor of some of the different approaches and compromises being pursued and provide some guide posts to the literature for the reader who wishes to delve more deeply into this subject.

The basic compromise which must be made is between complexity to incorporate as true a representation of the physics inherent in Eqs. (2.1.10 - 2.1.11) as possible and simplicity to make model calculations possible for more problems of interest. It is, of course, not possible to equate complexity with physical rigor, but it does appear fairly universally true that practical models require a liberal use of judicious simplifying assumptions. The simplest models we wish to consider here are those that, at least, make some use of the physics involved in the Reynolds stress equations in parameterizing the flux relationships used to close the mean equations.

A table covering the wide variety of mixing length models that have been applied to the PBL problem is given in McBean, et al. (1979). The most popular of these involves formulae of the type

$$\overline{uw} = -\ell^2 f(Ri) \left[\left(\frac{\partial U}{\partial z}\right)^2 + \left(\frac{\partial V}{\partial z}\right)^2\right]^{1/2} \frac{\partial U}{\partial z} \qquad (2.3.1)$$

where $\ell(z/\delta)$ and $f\{Ri = [\beta g \partial\theta/\partial z]/[(\partial U/\partial z)^2 + (\partial V/\partial z)^2]\}$ are analytical fits to semi-empirical parameterizations. The conditions necessary for such a form to be consistent with Eq. (2.1.10) are interesting. First, it requires assuming the turbulence to be in local equilibrium so that the left hand side of the equation as well as the diffusion contributions of the higher-order terms on the right hand side are negligible. Second, it requires assuming an expansion about isotropic turbulent conditions. In spite of the fact that these two assumptions are somewhat contradictory, judicious choices of ℓ and f can permit this formulation to lead to useful results for many problems.

At the other end of the spectrum are the models (e.g., Andre, et al., 1976; Lumley, Zeman, and Siess, 1978) which carry the closure to third order to more correctly model the third-order terms appearing in Eq. (2.1.10). Such an approach should be expected to yield improvements in the dynamics of the turbulence, particularly in the representation of the third-order turbulent correlations. Our approach here is to describe a compromise which imposes a relatively simple closure approximation to allow Eqs. (2.1.10 - 2.1.12) to be carried. With this choice, we expect the computational results for the appropriate second-order correlations to approximate the observations of such quantities as the Reynolds stress, the heat flux, species flux and/or temperature variance for which we seek an engineering answer. We do not expect all the third-order correlations to be very well represented. With this compromise in mind, let us look at simple models for the higher terms in Eqs. (2.1.10 - 2.1.12).

The terms which must be modeled may be grouped as dissipation terms:

$$2\nu \overline{\frac{\partial u_i}{\partial x_k}\frac{\partial u_j}{\partial x_k}}, \qquad 2K \overline{\frac{\partial \theta}{\partial x_k}\frac{\partial \theta}{\partial x_k}}, \qquad 2K_c \overline{\frac{\partial c}{\partial x_k}\frac{\partial c}{\partial x_k}}, \qquad \nu\theta \overline{\frac{\partial^2 u_i}{\partial x_j^2}} + Ku_i \overline{\frac{\partial^2 \theta}{\partial x_j^2}}, \qquad \nu c \overline{\frac{\partial^2 u_i}{\partial x_j^2}} + K_c u_i \overline{\frac{\partial^2 c}{\partial x_j^2}} \tag{2.3.2}$$

terms involving interaction with the fluctuating pressure gradient:

$$\overline{\frac{u_i}{\rho}\frac{\partial p}{\partial x_j}} + \overline{\frac{u_j}{\rho}\frac{\partial p}{\partial x_i}}, \qquad \overline{\frac{\theta}{\rho}\frac{\partial p}{\partial x_i}}, \qquad \overline{\frac{c}{\rho}\frac{\partial p}{\partial x_i}} \tag{2.3.3}$$

and third-order correlations:

$$\frac{\partial}{\partial x_k}\left(\overline{u_k u_j u_j}\right), \qquad \frac{\partial}{\partial x_j}\left(\overline{u_i u_j \theta}\right), \qquad \frac{\partial}{\partial x_j}\left(\overline{u_j \theta^2}\right), \qquad \frac{\partial}{\partial x_j}\left(\overline{u_i u_j c}\right), \qquad \frac{\partial}{\partial x_j}\left(\overline{u_j c^2}\right) \tag{2.3.4}$$

Lumley (1979) views second-order-closure modeling as assuming that the length and time scales of the turbulence are small relative to the length and time scales characterizing the distributions of the mean quantities; i.e., that the flowfield is quasisteady and quasihomogeneous. Although this assumption permits the development of a consistent expansion procedure, it imposes a limitation which does not appear to be either necessary or desirable. It is exactly those situations where the length and time scales of both the turbulence and the mean flow are of the same order where first-order closure is most seriously in error and thus for which we look most urgently to second-order modeling for help. Since the limitation is only imposed if it is introduced as part of the technique for chosing the modeled terms, it seems to provide strong motivation not to rely too heavily on this otherwise elegant expansion procedure for determining model coefficients.

Dissipation terms. The dissipation terms measure the effect of molecular smoothing on the structure of the turbulent correlations. Even in high-Reynolds-number flow, we expect viscous dissipation to be the major loss mechanism for turbulent kinetic energy. Owing to the nonlinear terms in the Navier-Stokes equation, a reduction in viscosity is compensated by a reduction in scale of the smallest eddies in the flow. The dissipation eddies are much smaller than the eddies that receive their energy directly from the mean flow when the Reynolds number is large, and one may assume that they are statistically independent of the mean-flow geometry.

Just as the end of the cascade contains no information on the scale of the large eddies, the breakup rate of the large eddies should be independent of ν. Therefore, for high Reynolds number, it appears dimensionally correct to have

$$\varepsilon = \nu \overline{\frac{\partial u_i}{\partial x_k}\frac{\partial u_j}{\partial x_k}} \sim \frac{q^3}{\Lambda} \tag{2.3.5}$$

where q is the root-mean-square value of the total velocity fluctuation and Λ is a macroscale of the eddies. This corresponds to taking the Taylor microscale λ proportional to $\Lambda/(a + bq\Lambda/\nu)^{1/2}$, where a and b are constants, as suggested by Rotta (1951). Since the viscous dissipation process is an isotropic process, most investigators model the dissipation terms as an isotropic term, i.e.,

$$\nu \overline{\frac{\partial u_i}{\partial x_k}\frac{\partial u_j}{\partial x_k}} = C_1 \delta_{ij} \frac{q^3}{\Lambda} \tag{2.3.6}$$

An additional anisotropic term seems appropriate when low Reynolds numbers are permitted (Lewellen, 1977), but since the Reynolds number in the atmospheric boundary layer is almost always large, we will neglect it here.

The corresponding models for ε_θ and ε_c are

$$\nu\theta\,\overline{\frac{\partial^2 u_i}{\partial x_j^2}\frac{\partial^2\theta}{\partial x_j^2}} + k_\theta u\,\overline{\frac{\partial^2 u_j}{\partial x_j^2}\frac{\partial^2 c}{\partial x_j^2}} = 0 ;$$

$$\varepsilon_\theta = k_\theta\,\overline{\frac{\partial\theta}{\partial x_k}\frac{\partial\theta}{\partial x_k}} = C_\theta\frac{q\overline{\theta^2}}{\Lambda_\theta} ; \qquad \varepsilon_c = k_c\,\overline{\frac{\partial c}{\partial x_k}\frac{\partial c}{\partial x_k}} = C_c\frac{q\overline{c^2}}{\Lambda_c} ;$$

where Λ_θ and Λ_c need not equal Λ.

Several investigators prefer to calculate ε from a dynamic equation obtained by modeling its governing equation. This will be discussed later in connection with the scale equation since, through Eq. (2.3.5), it is equivalent to an equation for Λ.

Pressure Correlations. The correlations involving pressure fluctuations redistribute the turbulent energy produced by the production terms. This can perhaps be seen more readily by rewriting the velocity-pressure correlation as

$$\pi_{ij} = \overline{\frac{u_j}{\rho}\frac{\partial p}{\partial x_j}} + \overline{\frac{u_j}{\rho}\frac{\partial p}{\partial x_i}} = \frac{\partial\overline{u_i p}}{\partial x_j} + \frac{\partial\overline{u_j p}}{\partial x_i} - \overline{\frac{p}{\rho}\left(\frac{\partial u_i}{\partial x_j} + \frac{\partial u_j}{\partial x_i}\right)} \tag{2.3.7}$$

Since the flow is incompressible, there will be no contribution from the last term in Eq. (2.3.7) to the kinetic energy of the turbulence, $q^2/2 = \overline{u_i u_i}/2$. It contributes only to a redistribution of energy between the Reynolds stresses. A volume integral of the first two terms on the right-hand side of Eq. (2.3.7) over any finite region of turbulence bounded by laminar flow will yield zero. Thus these two terms tend to contribute to a spatial redistribution, i.e., are diffusion terms.

All investigators appear to follow Rotta (1951) in modeling at least one contribution of the pressure correlation as a return-to-isotropy term proportional to the extent to which the flow is anisotropic, i.e.,

$$\pi_{ij} = \frac{C_3 q}{\Lambda}\left(\overline{u_i u_j} - \delta_{ij}\frac{q^2}{3}\right) \tag{2.3.8}$$

The term in parentheses, the departure from isotropy, provides the correct tensor symmetry and q/Λ provides the correct dimensionality. Donaldson (1972, 1973) adds to this a spatial diffusion term with proper symmetry and dimensionality to represent the first two terms on the right-hand side of Eq. (2.3.7).

$$\pi_{ij} = \frac{C_3 q}{\Lambda}\left(\overline{u_i u_j} - \delta_{ij}\frac{q^2}{3}\right) + C_4\left[\frac{\partial}{\partial x_i}\left(q\Lambda\,\overline{\frac{\partial u_k u_j}{\partial x_k}}\right) + \frac{\partial}{\partial x_j}\left(q\Lambda\,\overline{\frac{\partial u_k u_i}{\partial x_k}}\right)\right] \tag{2.3.9}$$

Most investigators add terms simulating the pressure contributions in the interactions between mean shear and turbulence, and between buoyancy and turbulence. As given by Zeman (1981) these are

$$\pi_{ij(b)} = -2q^2\left[\frac{1}{5}S_{ij} + \frac{3}{7}\left(S_{ik}b_{kj} + S_{jk}b_{ki} - \frac{2}{3}S_b\delta_{ij}\right)\right] \tag{2.3.10}$$

$$\pi_{ij(c)} = -\frac{3}{10}\beta_\ell\left(\overline{\theta u_i}\,\delta_{\ell j} + \overline{\theta u_j}\,\delta_{\ell i} - \frac{2}{3}\overline{\theta u_\ell}\,\delta_{ij}\right) \tag{2.3.11}$$

where

$$S_{ij} = \frac{1}{2}\left(\frac{\partial u_i}{\partial x_j} + \frac{\partial u_j}{\partial x_i}\right)$$

$$b_{ij} = \frac{u_i u_j}{q^2} - \frac{1}{3}\delta_{ij}$$

The coefficients in Eq. (2.3.10) were determined by matching to so-called rapid-distortion calculations involving a linear expansion around an isotropic state. Unfortunately this model is inconsistent with the majority of boundary-layer data (Zeman, 1981) and various authors have altered the constants in some way to achieve agreement with the data of most interest to them. Lumley (1979) argues that the basic problem is that the constant C_3, in Eq. (2.3.8) is really a function of $b_{ij}\,b_{ij}$. Another approach for boundary layer flows is to add near-surface corrective functions representing the contribution of the surface effect on fluctuating pressure terms (Gibson and Launder, 1978).

It is not surprising that these pressure terms show a lot of variation for different flows, since these pressure terms involve spatial integrals over the domain of the pressure variation. Their parameterization in terms of local properties of the mean flow variables and second order turbulent correlations must allow for the complete myriad of turbulent structures possible. No "standard" treatments for these terms are available at present. Several of the calculations exemplified in the later chapters will involve setting the terms in Eqs. (2.3.10 - 2.3.11) to zero following Lewellen (1977) and Andre, et al. (1978). Such a model involves a compromise between known deficiencies in certain limits and the simplicity of allowing the model to remain invariant over a wide range of applications. Also the combination of the simple forms, Eqs. (2.3.6 and 2.3.8) can be shown to provide a model which always satisfies the realizability relations $[\overline{u_\alpha u_\beta} > 0$ for $\alpha = \beta$, $\overline{u_\alpha u_\beta}^2 \leq \overline{u_\alpha u_\alpha}\;\overline{u_\beta u_\beta}$, and let $|\overline{u_\alpha u_\beta}| > 0]$ (Schumann, 1977), while the more complex forms do not always satisfy these conditions.

If only the leading return-to-isotropy term is retained the corresponding temperature and species pressure terms may be modeled as

$$\overline{\frac{\theta}{\rho}\frac{\partial p}{\partial x_i}} = \frac{Aq}{\Lambda_\theta}\overline{u_i\theta} \tag{2.3.12}$$

$$\overline{\frac{c}{\rho}\frac{\partial p}{\partial x_i}} = \frac{Aq}{\Lambda_c}\overline{u_i c} \tag{2.3.13}$$

Third-Order Velocity Correlations. These terms represent a process by which the turbulent correlation is transferred from one part of the flow to another without any net production or loss. This can be demonstrated, as it was for the pressure diffusion term of Eq. (2.3.7), by integration over a finite volume. When the volume is bounded by either laminar or by homogeneous isotropic flow, the integral will vanish. The most popular modeling of this transport term is as gradient diffusion, although Bradshaw (1972) has suggested that it could well be algebraic.

A number of different gradient diffusion forms have been used as a model for this term. Donaldson (1972) proposed a form that satisfies the tensor symmetry of $\overline{u_k u_i u_j}$ with a scalar diffusion coefficient.

$$D_{ij} = \frac{\partial}{\partial x_k}\left(\overline{u_k u_i u_j}\right) = C_6\frac{\partial}{\partial x_k}\left[q\Lambda\left(\overline{\frac{\partial u_i u_j}{\partial x_k}} + \overline{\frac{\partial u_k u_i}{\partial x_j}} + \overline{\frac{\partial u_k u_j}{\partial x_i}}\right)\right]$$

Hanjalic and Launder (1972) used a form with tensorial diffusivity

$$D_{ij} = C_6\frac{\partial}{\partial x_k}\left[\frac{\Lambda}{q}\left(\overline{u_k u_\ell}\,\overline{\frac{\partial u_i u_j}{\partial x_\ell}} + \overline{u_i u_\ell}\,\overline{\frac{\partial u_j u_k}{\partial x_\ell}} + \overline{u_j u_\ell}\,\overline{\frac{\partial u_i u_k}{\partial x_\ell}}\right)\right]$$

They obtained this form by a "firm pruning" of the exact equation for $\overline{u_k u_i u_j}$. Others have included more information from the third order equations as reviewed by Zeman (1981). Andre, et al. (1978) carries 21 rate equations for third order correlations in their simulation of the atmospheric boundary layer.

The simplest possible form for all of the diffusion terms in Eq. (2.3.4) is given by

$$\frac{\partial}{\partial x_j}\left[u_j(\;)\right] = \nu_c\frac{\partial}{\partial x_j}\left[q\Lambda\frac{\partial}{\partial x_j}(\;)\right] \tag{2.3.14}$$

Although this form satisfies the tensor symmetry of D_{ij}, it does not satisfy the symmetry of $\overline{u_k u_i u_j}$ itself.

Modeled Equations. Our philosophy is to first attempt calculations with the simplest possible second-order closure models. We choose to use Eq. (2.3.6) for the dissipation term, Eq. (2.3.8) for the pressure-velocity interaction, and the pressure contribution to diffusion incorporated with the velocity diffusion for one diffusion term like Eq. (2.3.14):

$$\nu\overline{\frac{\partial u_i}{\partial x_k}\frac{\partial u_j}{\partial x_k}} = \frac{b\delta_{ij}q^3}{3\Lambda} \tag{2.3.15}$$

$$\overline{\frac{p}{\rho}\left(\frac{\partial u_i}{\partial x_j}+\frac{\partial u_j}{\partial x_i}\right)} = -\frac{q}{\Lambda}\left(\overline{u_i u_j}-\delta_{ij}\frac{q^2}{3}\right) \tag{2.3.16}$$

$$\frac{\partial}{\partial x_k}\left(\overline{u_k u_i u_j}\right)+\frac{\partial \overline{u_i p}}{\partial x_j}+\frac{\partial \overline{u_j p}}{\partial x_i} = v_c\frac{\partial}{\partial x_k}\left(q\Lambda\frac{\partial \overline{u_i u_j}}{\partial x_k}\right) \tag{2.3.17}$$

In this restatement of the modeled terms, C_3 has been set equal to unity by using Eq. (2.3.8) to define the macroscale Λ. The other coefficients have been assigned the symbols given by Lewellen (1977).

When similar terms are used in the heat-flux, species-flux, temperature-variance, and species-variance equations, the modeled set of second-order correlation equations may be written as

$$\frac{\partial \overline{u_i u_j}}{\partial t}+U_l\frac{\overline{u_i u_j}}{\partial x_k} = -\overline{u_i u_k}\frac{\partial U_j}{\partial x_k}-\overline{u_j u_k}\frac{\partial U_i}{\partial x_k}+\beta g_i\overline{u_j\theta}+\beta g_j\overline{u_i\theta}$$
$$+v_c\frac{\partial}{\partial x_k}\left(q\Lambda\frac{\partial \overline{u_i u_j}}{\partial x_k}\right)-\frac{q}{\Lambda}\left(\overline{u_i u_j}-\delta_{ij}\frac{q^2}{3}\right)-\delta_{ij}\frac{2bq^3}{3\Lambda} \tag{2.3.18}$$

$$\frac{\partial \overline{u_i\theta}}{\partial t}+U_j\frac{\partial \overline{u_i\theta}}{\partial x_j} = -\overline{u_i u_j}\frac{\partial\Theta}{\partial x_j}-\overline{u_j\theta}\frac{\partial U_i}{\partial x_j}+\beta g_i\overline{\theta^2}+v_c\frac{\partial}{\partial x_j}\left(q\Lambda\frac{\partial \overline{u_i\theta}}{\partial x_j}\right)-\frac{Aq}{\Lambda_\theta}\overline{u_i\theta} \tag{2.3.19}$$

$$\frac{\partial \overline{\theta^2}}{\partial t}+U_j\frac{\partial \overline{\theta^2}}{\partial x_j} = -2\overline{u_j\theta}\frac{\partial\Theta}{\partial x_j}+v_c\frac{\partial}{\partial x_j}\left(q\Lambda\frac{\partial \overline{\theta^2}}{\partial x_j}\right)-\frac{2bsq\overline{\theta^2}}{\Lambda_\theta} \tag{2.3.20}$$

$$\frac{\partial \overline{u_i c}}{\partial t}+U_j\frac{\partial \overline{u_i c}}{\partial x_j} = -\overline{u_i u_j}\frac{\partial C}{\partial x_j}-\overline{u_j c}\frac{\partial U_i}{\partial x_j}+\beta g_i\overline{c\theta}+v_c\frac{\partial}{\partial x_j}\left(q\Lambda\frac{\partial \overline{u_i c}}{\partial x_j}\right)-\frac{Aq}{\Lambda_c}\overline{u_i c} \tag{2.3.21}$$

$$\frac{\partial \overline{c^2}}{\partial t}+U_j\frac{\partial \overline{c^2}}{\partial x_j} = -2\overline{u_j c}\frac{\partial C}{\partial x_j}+v_c\frac{\partial}{\partial x_j}\left(q\Lambda\frac{\partial \overline{c^2}}{\partial x_j}\right)-\frac{2bsq\overline{c^2}}{\Lambda_c} \tag{2.3.22}$$

$$\frac{\partial \overline{c\theta}}{\partial t}+U_j\frac{\partial \overline{c\theta}}{\partial x_j} = -\overline{u_j c}\frac{\partial\Theta}{\partial x_j}-\overline{u_j\theta}\frac{\partial C}{\partial x_j}+v_c\frac{\partial}{\partial x_j}\left(q\Lambda\frac{\partial \overline{c\theta}}{\partial x_j}\right)-\frac{2bsq\overline{c\theta}}{\Lambda_c} \tag{2.3.23}$$

This set provides the minimum requirements of any second-order closure. The combination of terms in each of these equations provides a destruction term for each correlation which allows an equilibrium value to be reached in a time long compared with Λ/q, and a diffusion term which prevents any excessively sharp gradients from occurring. Rather than use models with a large number of coefficients that are finely adjusted to fit a few particular flows, we choose to work with a relatively small number. The appropriate values of the coefficients as evaluated by Lewellen (1977) are $b = 0.125$, $A = 0.75$, $s = 1.8$, and $v_c = 0.3$. Results from other variations of the second-order closure set will be referred to in relation to particular applications.

Scale Determination. To complete closure, it is necessary to provide some means for determining the turbulent scales Λ, Λ_θ, and Λ_c, involved in the modeled terms. This is approached in different ways by various investigators. It may be specified empirically based on the gross features of the particular flow geometry; or it may be predicted from a semiempirically modeled, dynamic differential equation. Each of these approaches has some advantages and disadvantages.

The macroscale Λ is defined by Eqs. (2.3.15 - 2.3.17). It is expected to be related to the integral scale but, owing to our choice of normalization, not equal to it. It is also related to the mixing length used in first order closure models. As such, there is empirical information that can be used in our

determination of this model parameter. It appears fairly clear that the scale cannot exceed some fraction of the total spread of the region of turbulence and that, in some neighborhood of the wall, it should be proportional to the distance from the wall. These two simple ideas, together with empirical information used to determine the two implied constants of proportionality, are sufficient to permit the system to close with relatively good numerical results for many problems (e.g., Donaldson, 1973; Lewellen, et al., 1974). Others (e.g., Shir, 1973; Wyngaard and Coté, 1974; Mellor and Yamada, 1974; Burk, 1977; Andre, et al., 1978; and Brost and Wyngaard, 1978) have specified a completely empirically determined distribution of Λ across the region of interest in the same manner as is done for first-order mixing length approaches.

In an attempt to remove some of the arbitrariness of the specification of Λ for different flows, a number of investigators have developed a modeled dynamic equation for Λ or its equivalent. The starting points for such attempts have varied widely. A two-point-velocity-correlation equation forms the basis for the work of Rotta (1972), Naot, et al. (1973), Donaldson (1972), and Rodi (1972). By forming an equation for the two-point velocity correlation $u_i(x)u_i(x+r)$ and integrating to form an integral scale, it appears appropriate to take

$$q^2\Lambda = c \iiint_V \overline{u_i(x)\, u_i(x+r)}\, \frac{dV}{r^2} \tag{2.3.24}$$

The difficulty with this approach is that none of the terms can be integrated exactly. All of the terms must be modeled. This is also true if one starts with the equation for the dissipation ε, as is favored by many (e.g., Lumley and Khajeh-Nouri, 1974; Harlow and Nakayama, 1967; and Hanjalic and Launder, 1972) or with the equation of vorticity fluctuations as suggested by Daly and Harlow (1970) or Wilcox and Alber (1972). With the model chosen in the section on Modeled Equations, $\varepsilon = bq^3/\Lambda$. Also the vorticity fluctuations can be taken as proportional to q/Λ. Thus, with the aid of the energy equation, any of these approaches may be reduced to an equation for Λ. As Bradshaw (1972), and Mellor and Herring (1973) have pointed out, all of the resulting Λ equations have the same form:

$$\frac{D\Lambda}{Dt} = -s_1 \frac{\Lambda}{q^2} \overline{u_i u_j} \frac{\partial U_i}{\partial x_j} - s_2 bq + \text{buoyancy terms} + \text{diffusion terms} \tag{2.3.25}$$

The major difference in the various expressions lies in the construction of the turbulent diffusion terms. Unfortunately, these turn out to be more important in the scale equation than in the Reynolds stress equation. The scale equation as proposed by Lewellen (1977) for use with the set of equations given in 2.3.18 to 2.3.23 is

$$\frac{D\Lambda}{Dt} = 0.35 \frac{\Lambda}{q^2} \overline{u_i u_j} \frac{\partial U_i}{\partial x_j} + 0.6\, bq + 0.3 \frac{\partial}{\partial x_i}\left(q\Lambda \frac{\partial \Lambda}{\partial x_i}\right) - \frac{0.375}{q}\left(\frac{\partial q\Lambda}{\partial x_i}\right)^2 + \frac{0.8\Lambda}{q^2} g_i \overline{u_i \theta} \tag{2.3.26}$$

It is immediately obvious that the scale equation contains much more arbitrariness than the Reynolds stress equations, where many of the terms were determined precisely without recourse to modeling or coefficients. With such a large number of coefficients in the scale equation, a correspondingly large number of different experiments must be matched concurrently if the resulting coefficients are to have any invariant validity.

There is also the question as to what extent it is really appropriate to have the integral quantity Λ determined by point values of the other variables. Spatial boundary conditions may be expected to play a much more important role in the determination of Λ than they do for the Reynolds stress.

Finally, in some applications it will be appropriate to take $\Lambda_\theta = \Lambda_c = \Lambda$ while in other applications this will not be true. A formulation for the scalar-covariance decay rate, equivalent to a $\Lambda_{c\theta}$ equation, is given by Lumley (1979).

The model given in the preceding sections is quite similar to Mellor and Yamada's level 4 model (1974). In most of their subsequent applications they have favored a condensed version (level 2.5) which assumes that

$$(\overline{uw}, \overline{vw}) = -q\ell\, S_m \left(\frac{\partial U}{\partial z}, \frac{\partial V}{\partial z}\right) \tag{2.3.27}$$

$$\overline{w\theta} = -q\ell\, S_H \frac{\partial \theta}{\partial z} \tag{2.3.28}$$

The contracted form of Eq. (2.3.18) is carried to determine q^2, and the functions S_m and S_H are obtained by assuming a high Reynolds number local equilibrium in the remaining components of the Reynolds stress and heat flux equations, i.e., all gradients of the turbulent correlations are dropped. This approximation should be valid whenever the time scale of the turbulence, Λ/q, is less than the

characteristic time scale of the mean flow. The resulting algebraic relationships between the second-order correlations and the gradients of the mean variables can then be manipulated to give

$$S_m = \frac{3A_1(\overline{ww} - c_1q^2)/q^2 + 9A_1A_2\,\ell\, g\beta\,\overline{w\theta}/q^3}{1 + 9A_1A_2\,\ell^2\, g\beta(\partial\theta/\partial z)/q^2} \tag{2.3.29}$$

$$S_H = \frac{2A_2\,\overline{ww}/q^2}{1 + 3A_2B_2\,\ell^2\, g\beta(\partial\theta/\partial z)/q^2} \tag{2.3.30}$$

with

$$\frac{w^2}{q^2} = \frac{1}{3} + \left(2\overline{uw}\,\frac{\partial U}{\partial z} + 2\overline{vw}\,\frac{\partial V}{\partial z} + 4\beta g\,\overline{w\theta}\right)\frac{A_1\ell}{q^3}$$

and

$$(A_1, B_1, A_2, B_2, C_1) = (0.92, 16.6, 0.74, 10.1, 0.08)$$

Note that Eqs. (2.3.29 and 2.3.30) are those given by Mellor and Yamada (1978). When the same procedure is carried out on Eqs. (2.3.18 - 2.3.23) the equivalent forms are

$$\frac{\Lambda S_m}{\ell} = \frac{\overline{ww}/q^2 + (4/3)\,\Lambda\,\beta g\,\overline{w\theta}/q^3}{1 + (4/3)\,\Lambda^2\,\beta g(\partial\theta/\partial z)/q^2} \tag{2.3.31}$$

$$\frac{\Lambda S_H}{\ell} = \frac{(4/3)\,\overline{ww}/q^2}{1 + 5.9\,\Lambda^2\,\beta g(\partial\theta/\partial z)/q^2} \tag{2.3.32}$$

with

$$\frac{\overline{ww}}{q^2} = \frac{1}{3} + \frac{\Lambda}{3q^3}\left(2\overline{uw}\,\frac{\partial U}{\partial z} + 2\overline{vw}\,\frac{\partial V}{\partial z} + 4\beta g\,\overline{w\theta}\right)$$

Plots for some other choices of S_m and S_H are given by Blackadar (1979).

III. Similarity Relationships

3.1. *Monin-Obukhov Scaling in the Surface Layer*

The best understood region of the atmospheric boundary layer is the layer next to the surface where the turbulent fluxes of mass, momentum, and energy are essentially constant. Rigorously this layer is bounded by the tops of any surface roughness features at low z and by an upper height that remains much less than either the ratio of the surface flux of momentum to the sum of all but the last term of Eq. (2.1.7), or the ratio of the surface heat flux to the sum of all but the last term of Eq. (2.1.8). Within this layer the mean momentum and energy equations may be replaced by the statement that $\overline{uw}$ and $\overline{u\theta}$ remain constant equal to their respective surface values which may be represented as $-u_*^2$ and u_*T_*. When this characteristic velocity, u_*, and characteristic temperature, T_*, are used to normalize all velocities and temperatures in the steady, homogeneous version of equations (2.3.18-2.3.20) the equations are found to be a function of only one variable provided the turbulent length scale is a function of the same variable and the modeled terms introduce no new parameters. This single variable may be written as $\eta = z\kappa gT_*/T_0u_*^2 \equiv z/L$. Physically, the variable $(-z/L)$ is equal to the ratio of the buoyant production of turbulent kinetic energy to the production by shear. The characteristic length L is known as the Monin-Obukhov length following the work of Monin and Obukhov (1953). The resulting set of ordinary differential equations as modeled by Lewellen and Teske (1973) may be written as:

$$-\overline{ww}\frac{\partial U}{\partial z} + \frac{g}{T_0}\overline{u\theta} - \frac{q}{\Lambda}\overline{uw} = 0 \tag{3.1.1}$$

$$\frac{2g}{T_0}\overline{w\theta} + 0.3\frac{\partial}{\partial z}\left(\Lambda q\frac{\partial\overline{ww}}{\partial z}\right) - \frac{q}{\Lambda}\left(\overline{ww} - \frac{q^2}{3}\right) - \frac{q^3}{12\Lambda} = 0 \tag{3.1.2}$$

$$0.3\frac{\partial}{\partial z}\left(\Lambda q\frac{\partial\overline{vv}}{\partial z}\right) - \frac{q}{\Lambda}\left(\overline{vv} - \frac{q^2}{3}\right) - \frac{q^3}{12\Lambda} = 0 \tag{3.1.3}$$

$$-2\overline{uw}\frac{\partial U}{\partial z} + 0.3\frac{\partial}{\partial z}\left(\Lambda q\frac{\partial\overline{uu}}{\partial z}\right) - \frac{q}{\Lambda}\left(\overline{uu} - \frac{q^2}{3}\right) - \frac{q^3}{12\Lambda} = 0 \tag{3.1.4}$$

$$-\overline{ww}\frac{\partial T}{\partial z} + \frac{g}{T_0}\overline{\theta^2} - 0.75\frac{q\overline{w\theta}}{\Lambda} = 0 \tag{3.1.5}$$

$$-\overline{uw}\frac{\partial\Theta}{\partial z} - \overline{w\theta}\frac{\partial U}{\partial z} + 0.3\frac{\partial}{\partial z}\left(\Lambda q\frac{\partial\overline{u\theta}}{\partial z}\right) - 0.75\frac{q\overline{u\theta}}{\Lambda} = 0 \tag{3.1.6}$$

$$-2\overline{w\theta}\frac{\partial\Theta}{\partial z} + 0.3\frac{\partial}{\partial z}\left(\Lambda q\frac{\partial\overline{\theta^2}}{\partial z}\right) - 0.45\frac{q\overline{\theta^2}}{\Lambda} = 0 \tag{3.1.7}$$

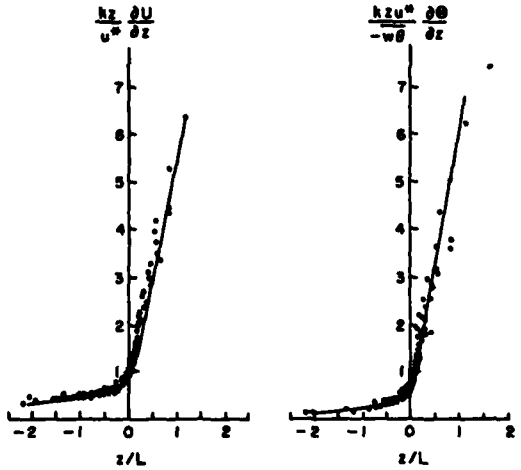

Figure 3.1.1 - Normalized atmospheric surface layer gradients as a function of stability. Model calculation from Lewellen and Teske (1973). Data from Businger, et al. (1971).

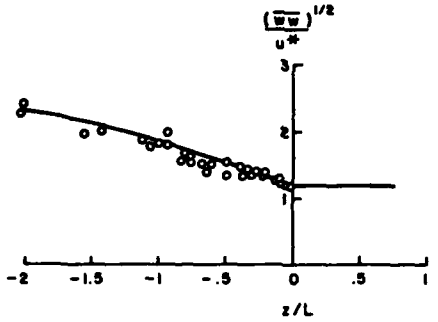

Figure 3.1.2 - Vertical velocity fluctuation in the atmospheric surface layer. Model calculation from Lewellen and Teske (1973). Data from Wyngaard, et al. (1971).

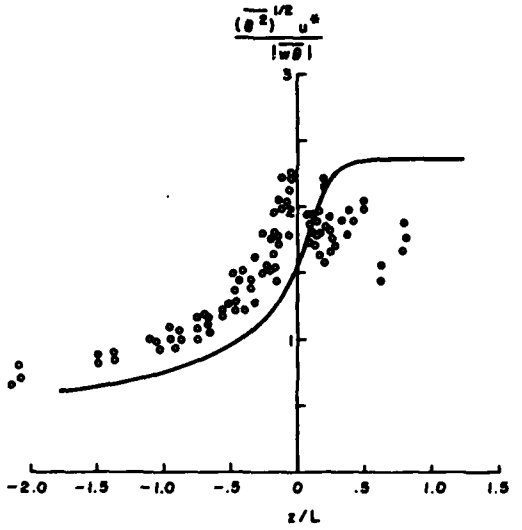

Figure 3.1.3 - Temperature fluctuation in the atmospheric surface layer. Model calculation from Lewellen and Teske (1973). Data from Wyngaard, et al. (1971).

These equations may be integrated to yield the seven normalized variables: $\varphi \equiv (\kappa z/u_*)(\partial U/\partial z)$, $\varphi_h \equiv (\kappa z/T_*)(\partial\theta/\partial z)$, σ_w/u_*, σ_U/u_*, σ_v/u_*, $\overline{u\theta}/u_*T_*$, and σ_θ/T_*. The resulting functions for some of these variables are compared with field observations in Figures 3.1.1 - 3.1.3. In these computations the turbulent scale Λ was set equal to $0.65z$, except it was not allowed to exceed an upper bound of $0.2L$ in stable flow. This particular bound on Λ was chosen to yield the observed critical Richardson number of 0.21. This bound was also used in determining the coefficient of the buoyant term in the scale equation, Eq. (2.3.26).

The normalized velocity and temperature gradients, Figure 3.1.1, show very good agreement between the model calculations and the data. A positive surface heat flux ($z/L < 0$) leads to increased turbulence and decreased gradients, while a negative surface heat flux ($z/L > 0$) leads to a damping of the turbulence and increased gradients. Under neutral conditions ($z/L = 0$), the ratio of the effective diffusivity for momentum to that for temperature is 3/4. In the model, this choice was determined by the value chosen for the model constant A in Eq. (2.3.12).

The vertical velocity and temperature fluctuations are compared with the data of Wyngaard, et al. (1971), in Figures 3.1.2 and 3.1.3. The agreement for the vertical velocity is very good but that for the temperature fluctuations leaves a bit to be desired. As pointed out by Wyngaard, et al. (1971), there is considerable uncertainty in $(v^2)^{1/2}u_*/w\theta$ at $z/L = 0$ because both variables go to zero.

Mellor (1973) made a somewhat similar calculation of these surface-layer similarity functions. The major difference is that Mellor eliminated the diffusion terms so that the differential equations reduce to an algebraic set. In this case the length scale may be normalized out of the problem, eliminating any need for, or any possibility of, incorporating an influence of stratification on the scale. His model coefficients must then be chosen so that they will match the critical Richardson number.

Although this surface layer similarity also leads to variations of σ_U and σ_v as a function of z/L, observations of these variables do not correlate with z/L. These horizontal wind variances are more dependent on variables which control the large eddy structure at larger heights above the boundary layer. This behavior can be incorporated within the surface layer similarity if the modeled higher order correlations in Equations (2.3.18-2.3.20) are allowed to be a function of two scales, rather than one. A model which allows the horizontal wind variance to be more a function of boundary layer thickness than it is of height z has been developed by Lewellen and Sandri (1980). The results of this model are compared with observations in the unstable layer (see Section 3.3) where the horizontal variance has been found to correlate with z_i/L.

Although the normalized velocity and temperature gradients in the surface layer can be completely determined by z/L only, the velocity and temperature at any height will also be a function of surface roughness. Useful analytic functions may be obtained by analytically fitting the empirical curves given in Figures 3.1.1 and 3.1.2 [e.g., Businger, et al. (1971)] and integrating as carried out by Paulson (1970) the resulting expressions for U and θ are:

$$\frac{U}{u_*} = \frac{1}{\kappa}\left(\ln\frac{z}{z_0} - \psi_1\right) \qquad (3.1.8)$$

$$\frac{z}{L} < 0$$

$$\frac{\theta - \theta_0}{\theta_*} = \frac{0.74}{\kappa}\left(\ln\frac{z}{z_0} - \psi_2\right) \qquad (3.1.9)$$

where

$$\psi_1 = 2\ln\left[\frac{1}{2}(1+x)\right] + \ln\left[\frac{1}{2}(1+x^2)\right] - 2\tan^{-1}x + \frac{\pi}{2}$$

with

$$x = \left(1 - 15\frac{z}{L}\right)^{1/4}$$

and

$$\psi_2 = \left\{2\ln\frac{1}{2}\left[1 + \left(1 - 9\frac{z}{L}\right)^{1/2}\right]\right\}$$

$$\frac{U}{u_*} = \frac{1}{\kappa}\left(\ln\frac{z}{z_0} + 4.7\frac{z}{L}\right) \qquad (3.1.10)$$

$$\frac{z}{L} > 0$$

$$\frac{\theta - \theta_0}{\theta_*} = \frac{1}{\kappa}\left[0.74\ln\frac{z}{z_0} + 4.7\frac{z}{L}\right] \qquad (3.1.11)$$

The species concentration may be expected to have a variation similar to the temperature.

Many variations on the formulation of scaling in the surface layer have been given in the literature, e.g., Blackadar, 1979; Bienkowski, 1979; Herbert and Panhaus, 1979; and, Panhaus and Herbert, 1979.

3.2. Neutral, Steady-State, PBL Scaling

The governing equations as given in Chapter II reduce in this case to the two components of the momentum equation:

$$0 = fV - \frac{\partial}{\partial z}(\overline{uw}) \qquad (3.2.1)$$

$$0 = f(U_g - U) - \frac{\partial}{\partial z}(\overline{vw}) \qquad (3.2.2)$$

and the six components of the Reynolds stress equation. Here the coordinate system has been aligned with the geostrophic wind so that $\partial P/\partial x = 0$ and $\partial P/\partial y = -fU_g$. The appropriate boundary conditions for this case are to have the mean wind approach the geostrophic wind, U_g, as $z \to \infty$ and to go to zero at the effective aerodynamic roughness height, z_0, while all the turbulent quantities go to zero as $z \to \infty$ and approach the surface layer similarity values given in Section 3.1 as $z \to z_0$.

Under these conditions, the governing equations can be normalized so that only one parameter, the Rossby number $Ro = U_g/z_0 f$, is needed to determine the flow. The resulting relative variation with respect to Rossby number shows how the flow responds to changes in geostrophic wind, surface roughness, and latitude which determines f. Figures 3.2.1 and 3.2.2 show the mean wind profiles normalized by the geostrophic wind as a function of the normalized height for different values of Ro as given by a numerical solution to the Reynolds stress equations as modeled in Eq. (2.3.18) (Lewellen and Williamson, 1976). The change in wind direction with height is less than it would be in an Ekman Spiral, which is the solution of the analogous laminar flow problem. The vertical velocity variance is shown in Figure 3.2.3 for the same conditions.

The vertical coordinate for these plots is normalized in such a way that for typical values of $f = 10^{-4}\text{sec}^{-1}$ and $U_g = 10$ m/sec, z may be read directly in Kms. For other values of U_g/f, the plot must be read as a dimensionless plot and the appropriate physical z determined. An increase in the geostrophic wind will increase Ro and reduce the dimensionless boundary layer thickness but the physical boundary layer thickness will increase since the effect in the coordinate transformation is much stronger than that produced by an equal change in Ro. Likewise the boundary layer will become thicker as the equator is approached, for equal values of U_g/z_0. Increases in the surface roughness always increase the boundary layer thickness in this limit.

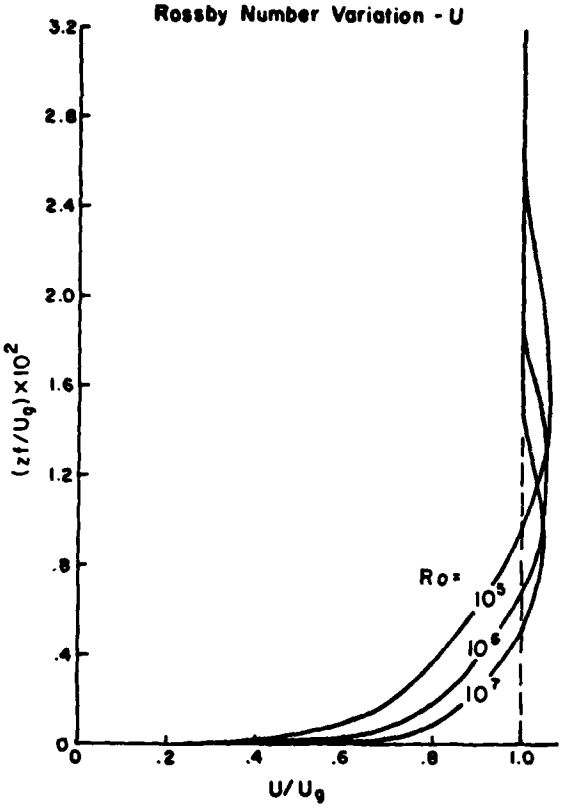

Figure 3.2.1 - Influence of Rossby number on the mean wind component in the direction of the geostrophic wind (normalized altitude converts to z in Km for $f = 10^{-4}sec^{-1}$ and U_g = 10 m/sec).

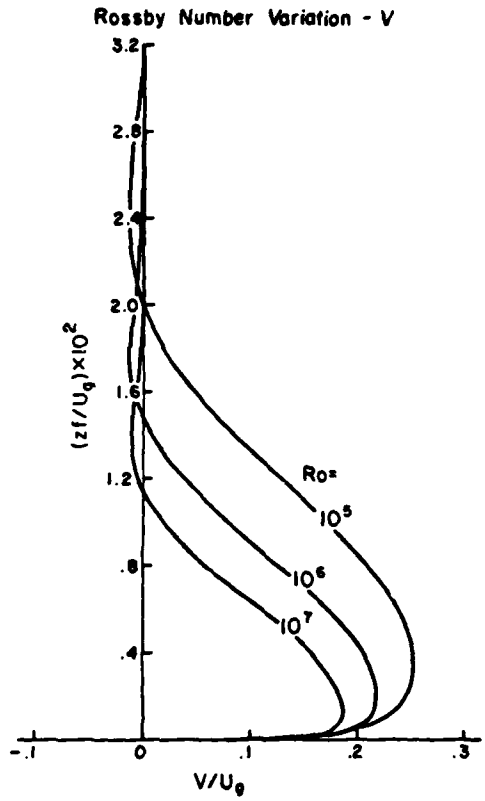

Figure 3.2.2 - Influence of Rossby number on the mean wind component in the direction normal to the geostrophic wind for the conditions of Figure 3.2.1.

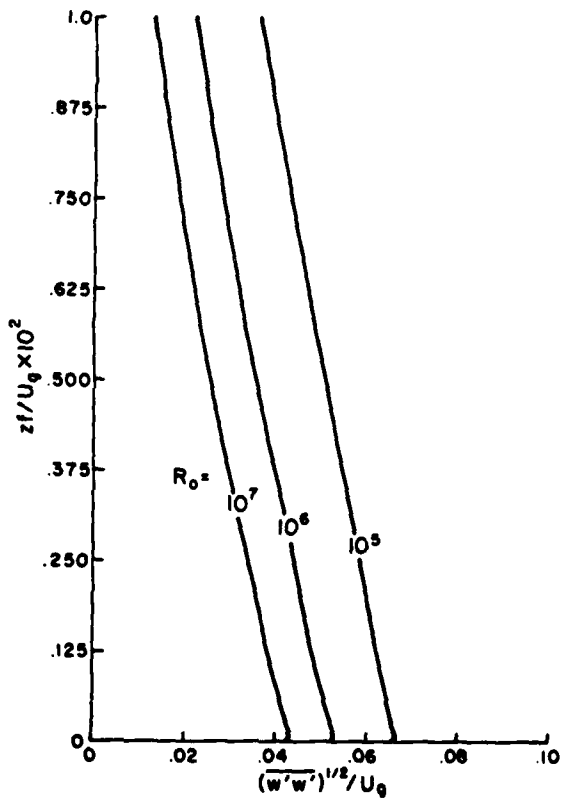

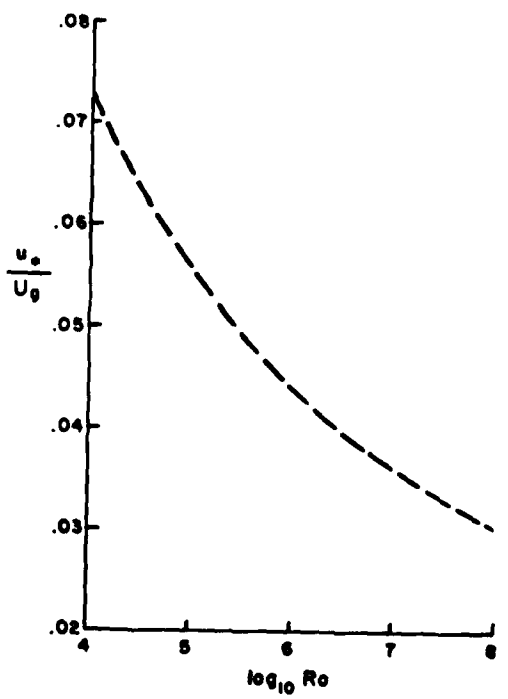

Figure 3.2.4 - Surface shear stress as a function of Rossby number for the neutral planetary boundary layer.

Figure 3.2.3 - Influence of Rossby number on the variance of the vertical velocity for the conditions of Figure 3.2.1.

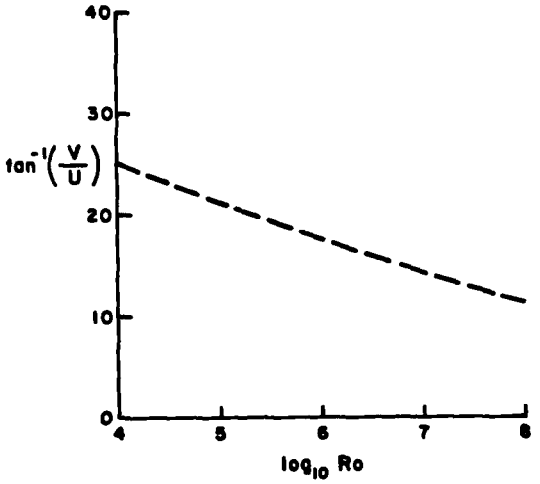

Figure 3.2.5. - Angle between the surface wind and the geostrophic wind as a function of Rossby number for the neutral planetary boundary layer

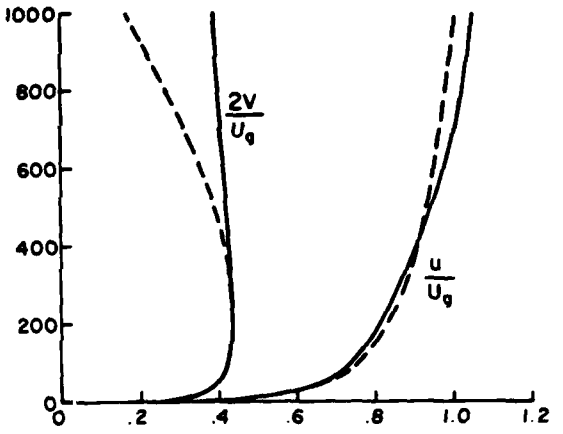

Figure 3.2.6 - Comparison of the solution predicted by Eqs. (3.2.3 and 3.2.4) (——) with that given for the complete second-order closure model in Figures 3.2.1 and 3.2.2. (– – –) ($z_0 = 0.1$, $U_g/fz_0 = 10^6$).

The surface drag coefficient, defined as U_*^2/U_g^2, is a function only of Ro in this limiting case. It is given in Figure 3.2.4 as predicted by the present model. A summary of empirical correlations for this variable is given by McBean, et al. (1979). The data show considerable scatter since the conditions necessary for this steady state, neutral profile are seldom completely satisfied in nature. The model result shown falls within the range of the empirical correlations. The slight decrease in drag coefficient with increasing Ro is consistent with a decreasing ratio of characteristic turbulent macroscale A to boundary layer thickness. As shown in Figure 3.2.5, the angle between the surface wind and the geostrophic wind also decreases with increasing Ro.

The logarithmic variation for wind speeds in the surface layer given by Eq. (3.1.8) under neutral conditions is valid to a much higher altitude for U than it is for V. The departure from $\ln z/z_0$ is forced by the geostrophic pressure gradient fU_g acting parallel to v. The logarithmic term is the first term in a consistent expansion for small z. When the expansion is continued to bring in the influence of the pressure gradient the two velocity components may be written as (Lewellen, 1977):

$$U = \frac{U_*}{\kappa[1 + (v_*/u_*)^4]^{1/4}} \ln \frac{z}{z_0} \tag{3.2.3}$$

$$V = \frac{1}{\kappa U_*[1 + (v_*/u_*)^4]^{1/4}} \left\{ V_*^2 \ln \frac{z}{z_0} - fU_g(z - z_0) + \frac{fu_*^2}{[1 + (v_*/u_*)^4]^{1/4}} \left[z \ln \frac{z}{z_0} - 2(z - z_0) \right] \right\} \tag{3.2.4}$$

Equations (3.2.3) and (3.2.4) agree with Figures 3.2.1 and 3.2.2 to heights well above that at which V_{max} occurs, as seen in Figure 3.2.6.

3.3. Convectively Mixed Layer Scaling

The unstable boundary layer which is dominated by buoyantly driven turbulence has proven to be amenable to a similarity description. In a series of publications involving analysis, numerical studies and experimental observations Deardorff and Willis (Deardorff, 1970a,b, 1972, 1974a,b; and, Willis and Deardorff, 1974) have shown that the mean temperature, and several of the turbulent correlations are functions only of z/z_i and of the characteristic convective velocity W_*. This characteristic velocity is defined as

$$w_* = \left(g \frac{\overline{w\theta_0}}{T_0} z_i \right)^{1/3} \tag{3.3.1}$$

where $\overline{w\theta_0}$ is the heat flux near the lower surface and z_i is the depth of the mixed layer. Such a similarity holds in the unstable PBL above the height -L, where L is the Monin-Obukhov length discussed in Section 3.1.

The similarity functions for this buoyantly driven turbulence may be obtained from Eqs. (2.3.18 - 2.3.20) by setting the mean velocity equal to zero, imposing a fixed surface heat flux at the bottom, and zero turbulence and a stable lapse rate at the top of the domain. The equations for this limit are

$$\frac{\partial}{\partial t}\left(\frac{\partial \theta}{\partial z}\right) = -\frac{\partial^2 \overline{w\theta}}{\partial z^2} \tag{3.3.2}$$

$$\frac{\partial \overline{w\theta}}{\partial t} = -\overline{ww}\frac{\partial \theta}{\partial z} + \frac{g\overline{\theta^2}}{T_0} + 0.3\frac{\partial}{\partial z}\left(q\Lambda \frac{\partial \overline{w\theta}}{\partial z}\right) - 0.75\frac{q}{\Lambda}\overline{w\theta} \tag{3.3.3}$$

$$\frac{\partial \overline{ww}}{\partial t} = \frac{2g}{T_0}\overline{w\theta} + 0.3\frac{\partial}{\partial z}\left(q\Lambda \frac{\partial \overline{ww}}{\partial z}\right) - \frac{q}{\Lambda}\left(\overline{ww} - \frac{q^2}{3}\right) - \frac{q^3}{12\Lambda} \tag{3.3.4}$$

$$\frac{\partial q^2}{\partial t} = \frac{2g}{T_0}\overline{w\theta} + 0.3\frac{\partial}{\partial z}\left(q\Lambda \frac{\partial q^2}{\partial z}\right) - \frac{q^3}{4\Lambda} \tag{3.3.5}$$

$$\frac{\partial \overline{\theta^2}}{\partial t} = -2\overline{w\theta}\frac{\partial \theta}{\partial z} + 0.3\frac{\partial}{\partial z}\left(q\Lambda \frac{\partial \overline{\theta^2}}{\partial z}\right) - 0.45\frac{q}{\Lambda}\overline{\theta^2} \tag{3.3.6}$$

$$\frac{\partial \Lambda}{\partial t} = 0.075q + 0.3\frac{\partial}{\partial z}\left(q\Lambda \frac{\partial \Lambda}{\partial z}\right) - \frac{0.375}{q}\left(\frac{\partial q\Lambda}{\partial z}\right)^2 + \frac{0.8\Lambda}{q^2}\frac{g}{T_0}\overline{w\theta} \tag{3.3.7}$$

The resulting similarity functions as given by Lewellen, Teske and Donaldson (1976) are plotted in Figures 3.3.1 - 3.3.3.

Figure 3.3.1 compares the model predictions for the normalized vertical velocity fluctuations with the experimental observations. The model predictions assume no mean velocity and a constant surface heat flux to simulate the laboratory experiment. The agreement between predictions and observations is heartening, particularly since no model constant adjustments were involved.

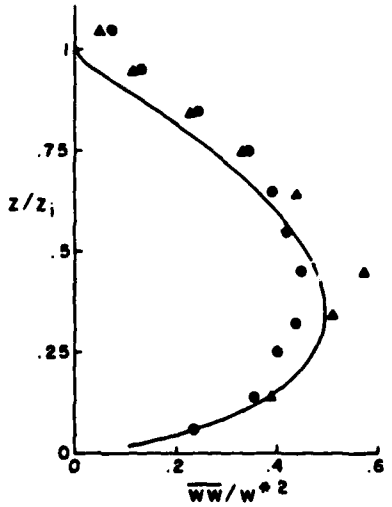

Figure 3.3.1 - Similarity profiles of vertical velocity fluctuation in an unstable mixed layer; model calculation from Lewellen, Teske, and Donaldson (1976); data from Willis and Deardorff (1974).

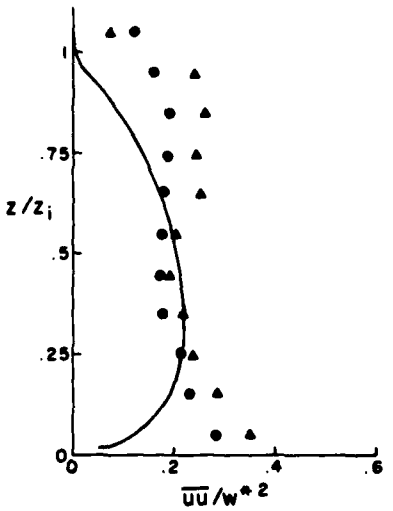

Figure 3.3.2 - Similarity profiles of horizontal velocity fluctuations for the conditions of Figure 3.3.1.

The horizontal velocity fluctuations are given in Figure 3.3.2. Here the comparison with experiment not as close since the observations show a peak near the lower surface that is not evidenced in the model results. The distributions of temperature fluctuations are shown in Figure 3.3.3. The agreement between model and experiment is very good except near the top of the mixed layer where the observations show a much stronger local maximum than is predicted. This is, at least in part, due to the existence of internal gravity waves in this region.

Favorable comparisons between model results and observations exist in Figures 3.3.1 - 3.3.3 in spite of the fact that the modeled vertical flux of kinetic energy is significantly different from the experimental observations, as shown in Figure 3.3.4. This is consistent with our basic assumption that the second-order correlations calculated from their conservation equations are given more accurately than the accuracy to which the third-order correlations are approximated.

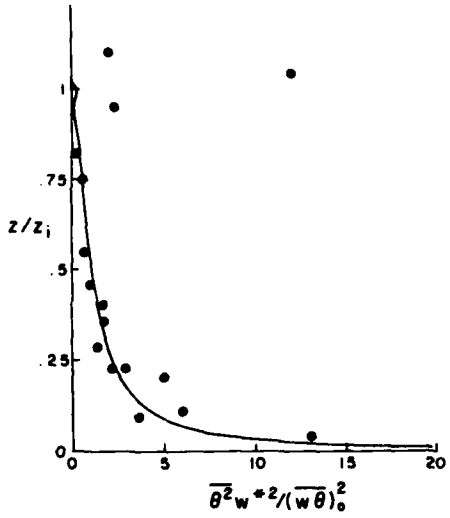

Figure 3.3.3 - Similarity profiles of temperature fluctuations for the conditions of Figure 3.3.1.

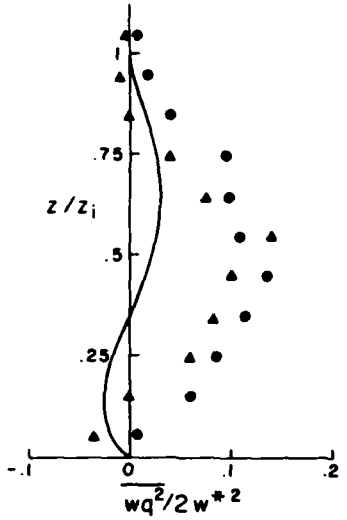

Figure 3.3.4 - Similarity profiles of vertical flux of kinetic energy for the conditions of Figure 3.3.1.

As shown in Figure 3.3.5, Zeman and Lumley (1976) obtain much better agreement between predictions of the flux of kinetic energy and the observations of this third-order quantity, using their second-order model designed specifically for buoyancy driven mixed layers. However, the comparisons for the second-order correlations, shown in Figures 3.3.6 - 3.3.7 are not substantially different from that obtained with the simpler model. The significant discrepancy between model results and observations in the horizontal fluctuations near the surface is unaffected by the more rigorous modeling of the third-order terms. Similar results for the second-order correlations of turbulence in the convectively mixed layer have also been obtained by Mellor and Yamada (1978), and Sun and Ogura (1980).

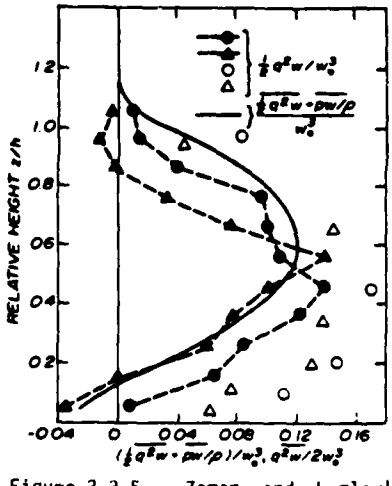

Figure 3.3.5 - Zeman and Lumley's (1976) predicted fluxes of turbulent energy compared with data: solid circles and triangles, Willis and Deardorff (1974); open circles and triangles, Lenschow (1970, 1974) and Lenschow and Johnson (1968); and squares, Telford and Warner (1964).

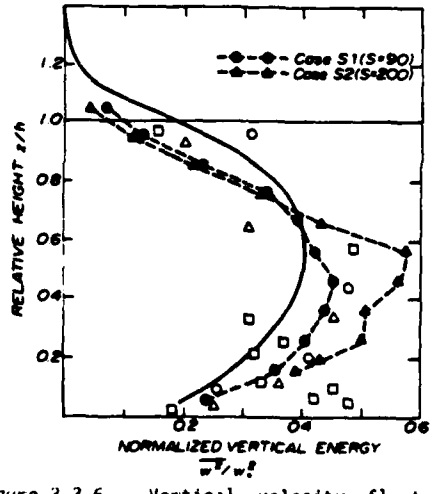

Figure 3.3.6 - Vertical velocity fluctuations as calculated by Zeman and Lumley (1976) compared with data: solid circles and triangles, Willis and Deardorff (1974); open circles and triangles, Lenschow (1970, 1974) and Lenschow and Johnson (1968); and squares, Telford and Warner (1964).

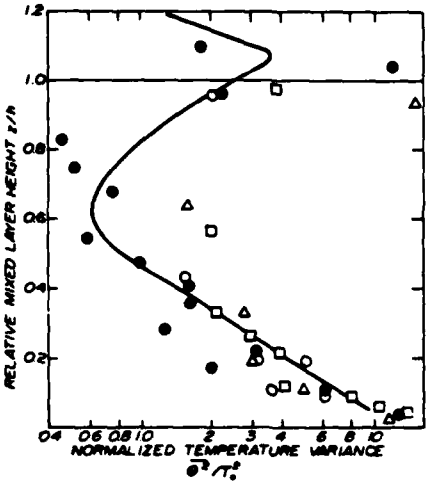

Figure 3.3.7 - Zeman and Lumley's (1976) predicted temperature variance compared with data: solid circles, Case S1 Willis and Deardorff (1974); open circles and triangles, Lenschow (1970, 1974); squares, Telford and Warner (1964).

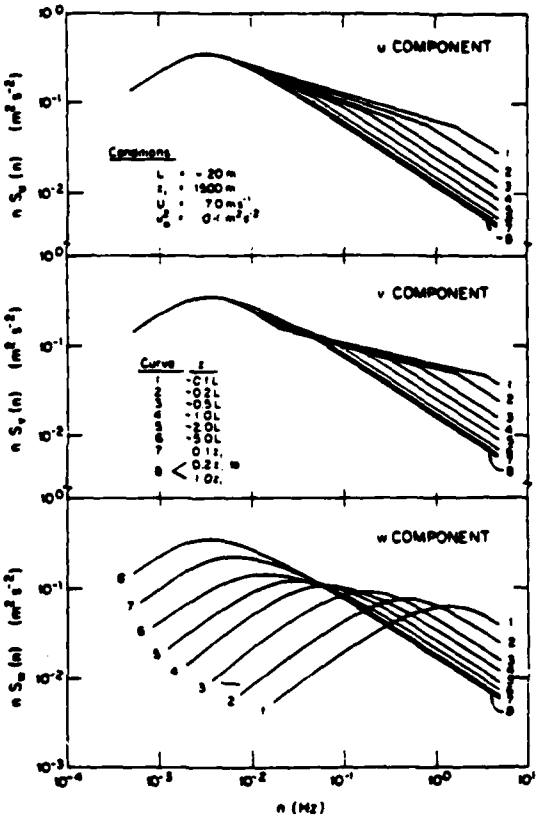

Figure 3.3.8 - Evolution of the velocity spectra with height as given by a composite plot of a number of experiments (Kaimal, 1978).

The principal difficulty with modeling the horizontal fluctuations appears to be the anisotropic nature of the turbulence scales, as mentioned in Section 3.1. This is demonstrated in the composite plot of the velocity spectra as a function of height given in Figure 3.3.8 from Kaimal (1978). The vertical velocity component clearly shows the scale of the eddies with the highest energy increasing in length proportional to increases in height, as assumed in Section 3.1. However, the corresponding scale of the horizontal velocity fluctuations shows almost no change with height. Instead, the horizontal velocity fluctuations appear to scale with the mixed-layer height, as exhibited by Wyngaard (1979).

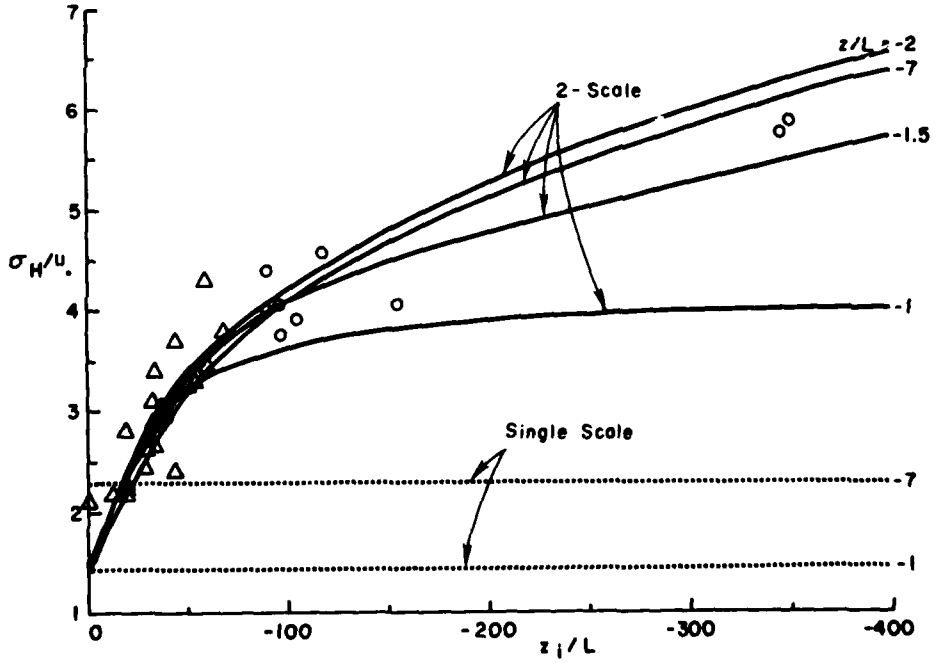

Figure 3.3.9 - Dimensionless rms horizontal velocity fluctuation as a function of the ratio of the mixed layer height to the Monin-Obukhov length. Two scale model calculation from Lewellen and Sandri (1980); data from Wyngaard (1979).

Lewellen and Sandri (1980) have attempted a modification to the model presented in Section 2.3 which permits the horizontal macro-length scale to be different from the vertical macro-length scale. The vertical scale is identified with the previous single scale as modeled in Section 2.3 and the horizontal scale is allowed to vary with the mixed-layer height.

The results of the 2-scale model for the horizontal velocity variance are contrasted with those of the single-scale model in Figure 3.3.9. The single-scale model predicts a variation with respect to z/L only, which is not observed in the data. Rather, the data are found to be relatively independent of z/L and to depend most strongly on z_i/L. The results of the 2-scale model are consistent with the data. The challenge of providing a consistent formulation for a general 2-scale model remains to be solved.

3.4. The Stable Ekman Boundary Layer

When the surface is cooler than the air above it a positive (stable) temperature gradient is typically established. This has a strong dynamical effect on the turbulent structure of the layer. The most important parameter governing these effects is a Richardson number which measures the ratio of buoyancy and inertia forces. Fundamental studies of shear flow in a stably stratified medium (e.g., Miles, 1961; and Howard, 1961) show that when

$$Ri \equiv \frac{g}{T_o} \frac{\partial\theta/\partial z}{(\partial U/\partial z)^2} > \frac{1}{4} \tag{3.4.1}$$

linear disturbances are damped out. When Ri is less than this critical value, turbulence may be expected to grow driven by the shear and Ri be increased by the decreases in gradients forced by the turbulence. When $Ri > Ri_{crit}$, turbulence may be expected to be damped by buoyancy which in the presence of any heat or momentum transport will lead to increased gradient and decreases in Ri. Thus, as suggested by Long (1975) natural stratified shear layers should tend towards an equilibrium at Ri_{crit}. If average values of the gradients are used, then

$$Ri_\delta = \frac{g}{T_o} \frac{\Delta\theta\,\delta}{U_g^2} \tag{3.4.2}$$

and setting this equal to Ri_{crit} leads to

$$\delta = \frac{1}{4} \frac{U_g^2}{(g/T_o)\Delta\theta} \tag{3.4.3}$$

consistent with the estimate of layer thickness given in Eq. (2.2.9). In general, Eq. (3.4.3) provides for an evolving boundary layer with $\Delta\theta$ and δ varying.

When $Ri_\delta = Ri_{crit}$ and δ satisfies the momentum equation so that $\delta \sim q/f$, then a steady equilibrium value of δ is possible. The thickness of this equilibrium Ekman layer may be given following Zilitinkevich (1972) as

$$\delta = \text{const}\ (u_* L/f)^{1/2} \tag{3.4.4}$$

It may be shown to be consistent with that given by Eq. (2.2.8).

The approach to a stable equilibrium, as given by Wyngaard (1975), using his version of second-order closure, is given in Figure 3.4.1 as a function of cooling rate. Three to six hours is the time required to reach the equilibrium state according to these calculations. This long transition time implies that such equilibrium stable layers will seldom be achieved because boundary conditions seldom remain constant this long in the atmosphere. Nonetheless, it is instructive to look at the wind and turbulence profiles expected under such steady conditions. Under such conditions the normalized profiles of wind, temperature, and turbulent correlations should be a function of only two parameters, the Rossby number, $U_g/z_o f$, and a stability parameter. The most frequent choice of the stability parameter is $\mu = u_*/fL$ (Zilitinkevich, 1972). In terms of this parameter, Eq. (3.4.4) may be written as

$$\delta = \text{const}\ \mu^{1/2} L \tag{3.4.5}$$

Near similarity can be achieved using $L\mu^{1/2}$ as a characteristic length to normalize the governing equations for the equilibrium case of strong stability. When u_* is used to normalize all turbulent velocities, θ_* to normalize all temperatures, and $u_*\mu^{1/2}$ to normalize the mean velocity the normalized Reynold's stress equation may be written as

$$0 = -\left(\widetilde{\overline{u_i u_k}}\,\frac{\partial \tilde{U}_j}{\partial \tilde{z}} + \widetilde{\overline{u_j u_k}}\,\frac{\partial \tilde{U}_i}{\partial \tilde{z}}\right)\delta_{k3} + \frac{1}{\kappa}\widetilde{\overline{u_j \theta}}\,\delta_{i3} + \frac{1}{\kappa}\widetilde{\overline{u_i \theta}}\,\delta_{j3}$$

$$+ 0.3\,\mu^{-1/2}\,\frac{\partial}{\partial \tilde{z}}\left(\tilde{q}\tilde{\Lambda}\,\frac{\partial \widetilde{\overline{u_i u_j}}}{\partial \tilde{z}}\right) - \frac{\tilde{q}}{\tilde{\Lambda}\mu^{1/2}}\left(\widetilde{\overline{u_i u_j}} - \delta_{ij}\,\frac{\tilde{q}^2}{3}\right) - \delta_{ij}\,\frac{\tilde{q}^3}{12\Lambda\mu} \qquad (3.4.6)$$

It is possible to show from the scale equation that Λ should be proportional to L under strongly stable conditions so that $\tilde{\Lambda} \sim \mu^{-1/2}$. Thus the diffusion term in Eq. (3.4.6) is the only term that keeps the Reynolds stress equation from becoming independent of μ, and Ro. For large μ the diffusion term should be negligible since it is order μ^{-1} in comparison with the other terms. Likewise the momentum equations can be made independent of μ and Ro. The derivative of the normalized equations may be written as

$$\frac{\partial \tilde{U}}{\partial z} + \frac{\partial^2 \widetilde{\overline{vw}}}{\partial z^2} = 0 \qquad (3.4.7)$$

$$\frac{\partial \tilde{V}}{\partial z} - \frac{\partial^2 \widetilde{\overline{uw}}}{\partial z^2} = 0 \qquad (3.4.8)$$

The appropriate boundary conditions for Eqs. (3.4.6 - 3.4.8) are also independent of μ and Ro.

$$@\ \tilde{z} \to 0\,, \qquad \frac{\partial \tilde{U}}{\partial \tilde{z}} \to \frac{4.7}{k}\,, \qquad \frac{\partial \tilde{V}}{\partial \tilde{z}} = 0$$

$$\widetilde{\overline{uw}} = 1$$

$$\tilde{q}^2 = 4\sqrt{2}$$

$$@\ \tilde{z} \to \infty\,, \qquad \frac{\partial \tilde{U}}{\partial \tilde{z}} = \frac{\partial \tilde{V}}{\partial \tilde{z}} = \widetilde{\overline{u_i u_j}} = 0\,. \qquad (3.4.9)$$

The only remaining requirement for similarity is that the thermal boundary conditions be specifiable in a manner which leaves the heat flux equation similar.

$$0 = -\widetilde{\overline{u_i u_j}}\,\frac{\partial \tilde{\Theta}}{\partial \tilde{z}}\,\delta_{j3} - \widetilde{\overline{u_j \theta}}\,\frac{\partial \tilde{U}_i}{\partial \tilde{z}}\,\delta_{j3} + \delta_{i3}\,\frac{\tilde{\theta}^2}{\kappa} + \frac{0.3}{\mu}\,\frac{\partial}{\partial \tilde{z}}\left(q\,\tilde{\Lambda}\mu^{1/2}\,\frac{\partial}{\partial \tilde{z}}\,\widetilde{\overline{u_i \theta}}\right) - 0.75\,\frac{\tilde{q}}{\tilde{\Lambda}\mu^{1/2}}\,\widetilde{\overline{u_i \theta}} \qquad (3.4.10)$$

$$0 = -2\widetilde{\overline{u_j \theta}}\,\frac{\partial \tilde{\Theta}}{\partial \tilde{z}}\,\delta_{j3} + \frac{0.3}{\mu}\,\frac{\partial}{\partial \tilde{z}}\left(\tilde{q}\,\tilde{\Lambda}\,\mu^{1/2}\,\frac{\partial \tilde{\theta}^2}{\partial \tilde{z}}\right) - 0.45\,\frac{\tilde{q}\,\tilde{\theta}^2}{\tilde{\Lambda}\mu^{1/2}} \qquad (3.4.11)$$

The only difficulty lies with the energy equation

$$\frac{\mu^{1/2} L}{u_*}\,\frac{\partial \tilde{\Theta}}{\partial t} = -\frac{\partial \widetilde{\overline{w\theta}}}{\partial \tilde{z}} \qquad (3.4.12)$$

which cannot be independent of time and still satisfy boundary conditions which permit the heat flux to have a zero value at $\tilde{z} \to \infty$. However, this can nearly be achieved by postulating a fixed cooling rate which allows the heat flux to vary linearly with $\tilde{z}$ across the bulk of the boundary layer.

The resulting distributions for the Reynolds stresses for this "equilibrium" stable layer are given in Figure 3.4.2 as calculated by Wyngaard (1975). The thickness of the boundary layer, i.e., the constant in Eq. (3.4.5), is fairly sensitive to the details of the model. Wyngaard obtained a value of approximately 0.2. The corresponding values of this constant from other models are 0.55 (Businger and Arya, 1974), 0.4 (Brost and Wyngaard, 1978), 0.27 (Rao and Snodgrass, 1979), and approximately (0.5) from the model given in Eqs. (3.4.6 - 3.4.12). Attempts to determine this number from observations have not been successful, presumably due to the scatter caused by such phenomena as advective effects, radiative flux divergence, baroclinicity, or unsteady influences to be discussed in Chapter IV. There is also some arbitrariness in the definition of δ. For the preceeding analysis δ has been defined as the height at which the shear stress falls to 5% of its surface value. This height is well below the height at which the velocity goes to the geostrophic value due to its oscillatory approach to ∞.

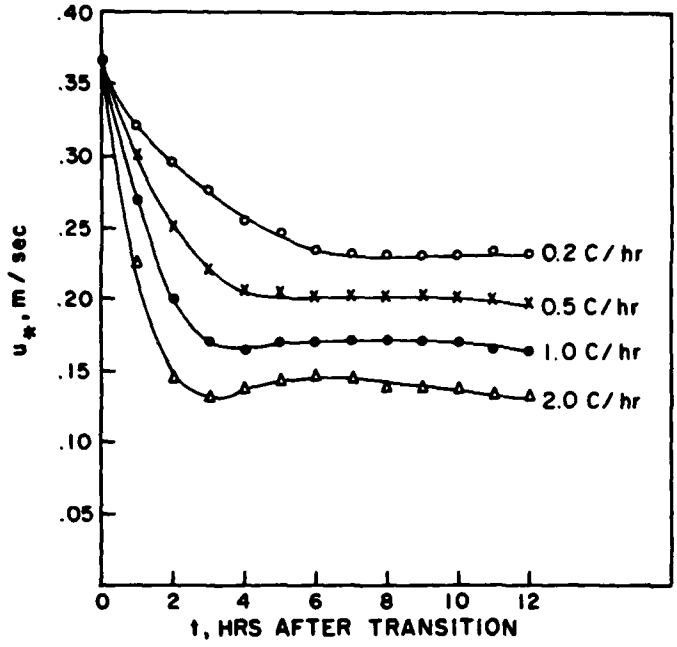

Figure 3.4.1 - The behavior of u* in an evolving nocturnal PBL, as predicted by the numerical model of Wyngaard (1975). Various cooling rates of the near-surface air were used, as shown.

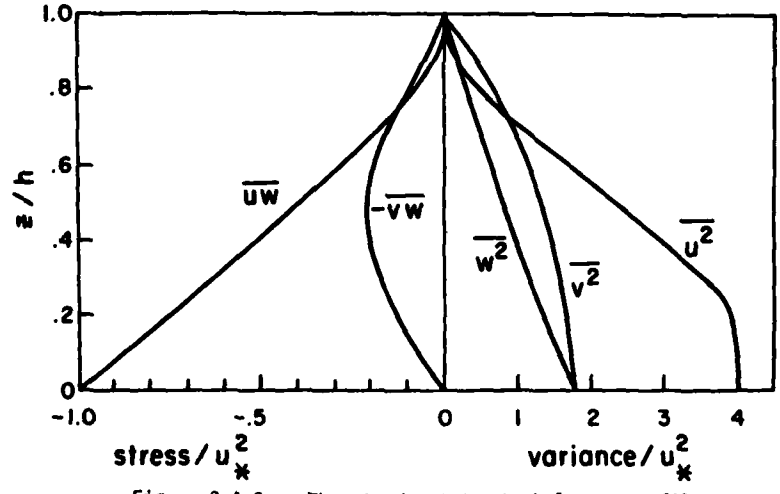

Figure 3.4.2 - The steady-state turbulence profiles in the nocturnal PBL, as found from the model calculations of Wyngaard (1975) (Northern Hemisphere).

Although the turbulence correlations can be presented in a normalized plot independent of μ and Ro, the wind profiles themselves cannot. They remain a function of both Rossby number and stability. Wind profiles for particular values of these parameters are given in Section 3.5.

It must be recognized that this treatment of the stable layer is based on a gross simplification of its true dynamics, since it ignores any role of internal gravity waves. Recent reviews of internal gravity waves in the stable boundary layer have been given by Chimonas (1980) and Einaudi (1980). Such waves can transport momentum vertically across the layer or horizontally within the layer and interact strongly with the turbulence. The model presented in Chapter II is based on ensemble averaging over fluctuations in the flow. Equations (2.1.10 - 2.1.12) are as valid for wave fluctuations as they are for turbulent fluctuations. However, the modeled terms in Eqs. (2.3.18 - 2.3.23) have been specifically modeled for fully turbulent flow and thus cannot be expected to be valid for coherent wave fluctuations. This remains a challenge for the future to generalize the modeling to represent both wave and turbulent fluctuations.

3.5. Stability Variations

Although we expect the dynamics of the changing boundary conditions to be important for most real stability variations in the atmosphere, we will first consider the quasi-steady case where the surface heat flux is held constant. Figures 3.5.1 and 3.5.2 show the wind profiles for four different stability conditions with Ro held constant at 10^6.

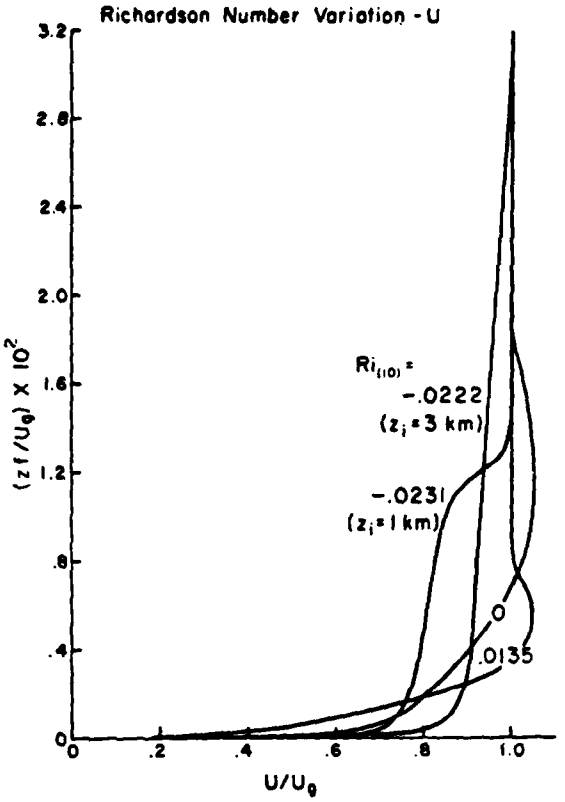

Figure 3.5.1 - Influence of Richardson number on the quasi-steady distributions of mean wind component in the direction of the geostrophic wind (Ro = 10^6); Lewellen and Williamson (1976).

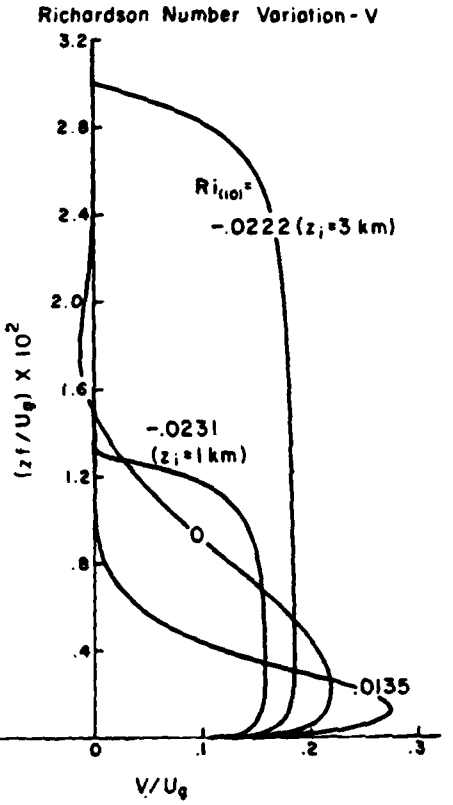

Figure 3.5.2 - Influence of Richardson number on the quasi-steady distributions of mean wind component in the direction normal to the geostrophic wind for the conditions of Figure 3.5.1.

A measure of the stability which is sometimes more convenient than μ is that of a bulk Richardson number based on the temperature and velocity differences between the surface and an arbitrary height such as 10 meters.

$$Ri_{10} = \frac{g(\theta_{10} - \theta_0)\, 10\,m}{T_0\, U_{10}^2} \qquad (3.5.1)$$

From Eqs. (3.1.10 and 3.1.11) it is possible to see that the most stable value possible for Ri_{10} in the surface layer is $(4.7)^{-1} = 0.21$, the critical Richardson number given by this model. Larger values of Ri_{10} mean that the surface layer is less than 10 meters thick. When the bulk Richardson number defined by Eq. (3.5.1) is positive, the flow is stable and the turbulence is damped. As shown in Figures 3.5.1 and 3.5.2, $Ri_{10} = 0.0135$ produces a boundary layer which is significantly smaller than the neutral case of $Ri_{10} = 0$, as should be expected for damped turbulence. This also produces a stronger transverse wind component, as seen in Figure 3.5.2. Although the wind shear at the surface is reduced by the increase in stability, the wind shear a short distance above the surface is significantly increased. Thus, from the point of view of the wind shear which an aircraft may encounter, an increase in Ri_{10} is quite likely to be associated with increased wind shear, as will be discussed in Section 6.2.

As outlined in Section 3.3, the specification of Ri_{10} alone is not sufficient to determine the unstable profile ($Ri_{10} < 0$) even in the quasi-steady case. Figures 3.5.1 and 3.5.2 show two wind profiles for nearly the same negative value of Ri_{10} and two quite different values of the inversion height. The unstable layer, driven by a positive surface heat flux, must be capped by a stable temperature inversion layer if the boundary layer is to reach a quasi-steady state. The figures show that in addition to the shear layer at the surface, a shear layer is also developed in the vicinity of the temperature inversion. As may be noted in the discussion of the boundary conditions in Section 3.3, z_i is not a rigid lid, but is defined as the altitude at which the maximum values of θ^2 occur as the temperature inversion is asymptotically approached. Between the surface shear layer and the inversion layer, the layer is relatively uniformly mixed.

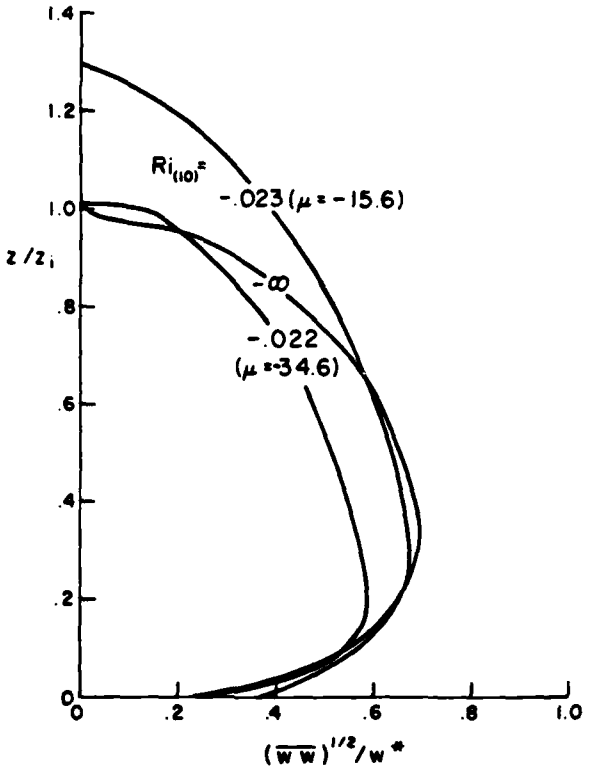

Figure 3.5.3 - Vertical velocity variance for unstable conditions compared with the limiting profile for free convection. Lewellen and Williamson (1976).

The vertical velocity variance is shown in Figure 3.5.3 for the unstable cases, but with the normalization which is appropriate for free convection when there is no mean wind shear. The limiting profile for $Ri_{10} \to -\infty$ was shown, in Section 3.3, to agree very well with laboratory simulations of this limit. Figure 3.5.3 shows that it does not require a very negative Ri_{10} to approach this limiting distribution. The corresponding values of the Zilitinkevich parameter, μ, are also given.

3.6. Flow within a Surface Canopy

A canopy of vegetation presents a complex lower boundary for atmospheric flows. For flow well above this canopy, it is usually adequate to characterize the boundary in terms of only an aerodynamic roughness, z_0. But when one is interested in the flow within the canopy or immediately above it, a more detailed representation is required.

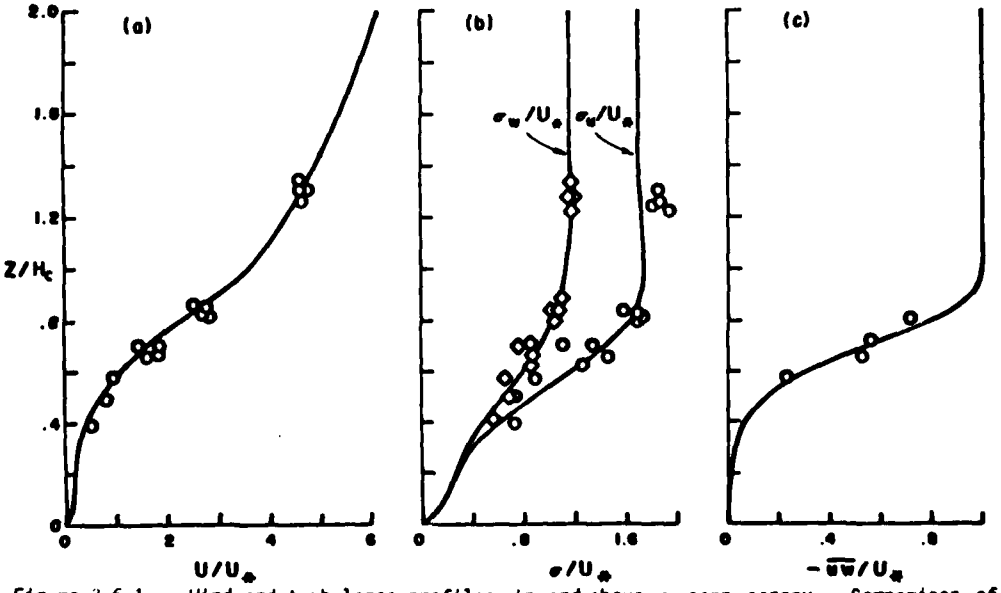

Figure 3.6.1 - Wind and turbulence profiles in and above a corn canopy. Comparison of model predictions (Lewellen and Sheng, 1980) with data from Shaw, et al. (1974).

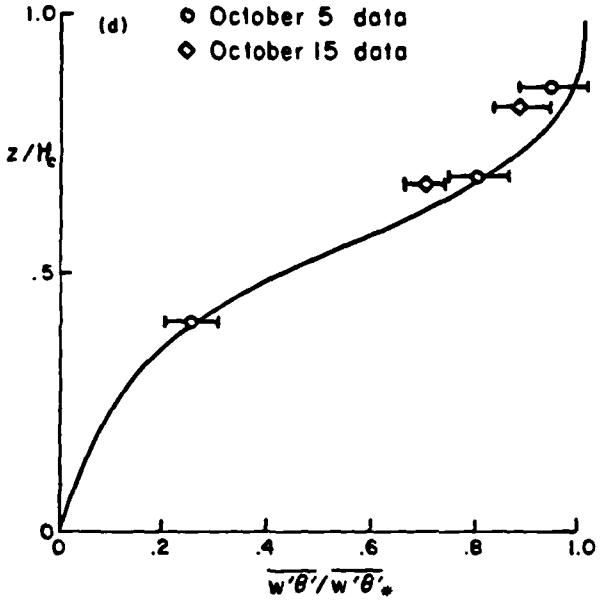

Figure 3.6.1 - Wind and turbulence profiles in and above a corn canopy. Comparison of model predictions (Lewellen and Sheng, 1980) with data from Shaw, et al. (1974).

Second-order closure models for canopy flow have recently been given by Wilson and Shaw (1977), and Lewellen and Sheng (1980). The principal difference between these two models is that the latter consider heat and species transport as well as momentum transport. They also use a somewhat more general representation of the drag per unit volume of the vegetation. The model is designed to predict the variation in surface layer heat and species transport as a function of surface Reynolds number ($U_* z_0/\nu$), Prandtl number, K/ν, Schmidt number, K_c/ν, and plant area density distribution. The comparison of the mean distributions of velocity, Reynolds stress and velocity variance predicted by Lewellen and Sheng (1980) are compared with some limited data for a corn canopy (Shaw, et al., 1974) in Figure 3.6.1.

The distributions shown in Figure 3.6.1 are only appropriate for vegetal canopies with plant area distribution similar to that of a mature corn field. If the plant area distribution is thicker near the top of the canopy, the effective displacement height of the mean wind will be increased. While a less dense canopy, such as a winter deciduous forest, will lead to larger values of u_* with a smaller displacement height. An approximately similar way of presenting the wind profiles for quite different canopy structures is given in Figure 3.6.2 where $(U - U_h)/u_*$ is plotted as a function of $(z - d)/(h - d)$. Both model calculations and field data show approximately similar shapes when presented this way.

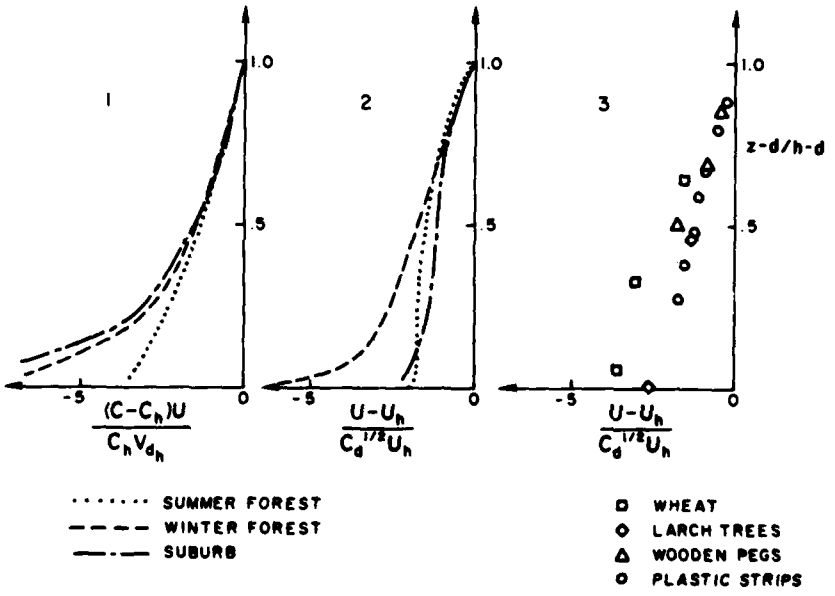

Figure 3.6.2 - Similarity profile of gaseous concentration (1) and wind velocity (2) predicted by Lewellen and Sheng (1980) and measured wind velocity as given by Cionco (1971).

More details on the flow within particular canopies are given in the two volumes edited by Montieth (1975) on vegetation and the atmosphere. Other information may also be found in the work of Cionco (1972) and Raupach and Thom (1981).

The surface layer formulation given in Section 3.1 is generally expected to hold above the canopy with z measured from the effective displacement height within the canopy. However, as shown by Figure 3.6.3, when d is chosen as the displacement height for momentum, the inverse gradient functions, $\varphi_{H,E}^{-1}$, may show considerable variation from the typical behavior. These data show effective $K_{H,E}$ which are double their expected values above a forest under slightly unstable conditions. The data shown were

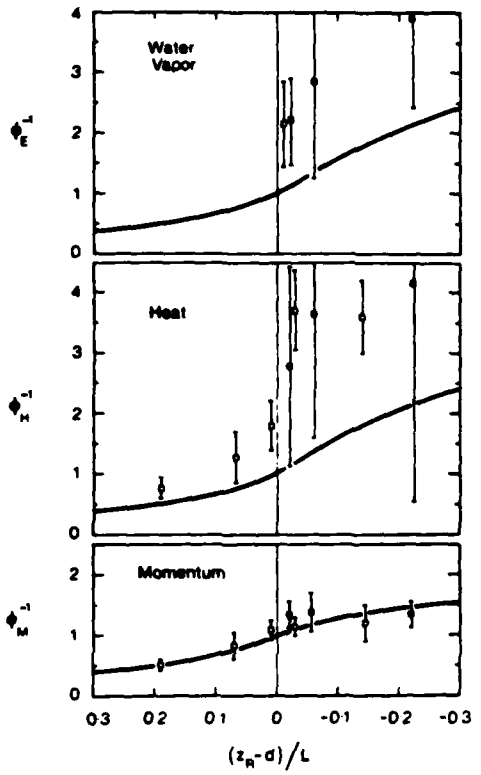

Figure 3.6.3 - Stability dependence of inverse influence functions $\varphi_{M,H,E}^{-1}$, measured over Thetford forest (□) and Uriarra forest (■). The smooth curves represent typical inertial-sublayer behavior. Raupach and Thom (1981).

taken approximately 5 meters above two different forests of height h ≈ 16 m and a mean tree spacing of 2 to 3 m. This indicates that the distribution of sources and sinks for momentum, heat, and water vapor may be quite different within a forest leading to characteristic length scales for the fluctuations of heat and water vapor different from those for the fluctuations of momentum. Thus one must be very cautious in applying simple scaling laws to flow within, or just above, real canopies.

IV. Interaction of Turbulent Transport with other Physical Mechanisms

4.1 Diurnal Variations in the Planetary Boundary Layer

Over homogeneous terrain, the atmospheric boundary layer may be considered a function of time and altitude only, when horizontal variations in the boundary conditions at the top of the boundary layer are considered negligible. Under such ideal conditions, the boundary layer may be expected to pass through the stability conditions considered in the last chapter during the course of a typical day. Since thermal energy is principally received and emitted from the surface, we expect unstable conditions to dominate in the afternoon hours and stable conditions to dominate during the late night hours. The results of calculations for a fixed geostrophic wind and upper level temperature lapse rate with a cyclic surface heat flux approximating conditions over the Midwestern plains during summer were presented by Lewellen, et al. (1974). These results were obtained using the quasiequilibrium approach outlined in Section 2.3, and the gross feature approach to the scale. Results obtained using the full equations were presented by Lewellen (1977). There is relatively little difference in the numerical results.

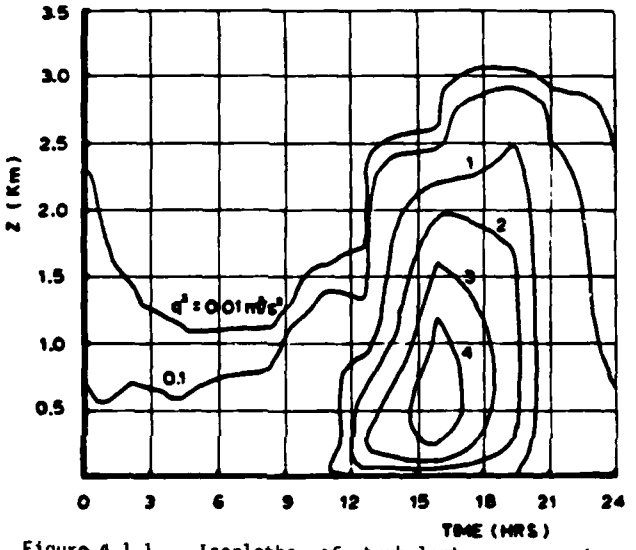

Figure 4.1.1 - Isopleths of turbulent energy in diurnal boundary layer. Lewellen (1977).

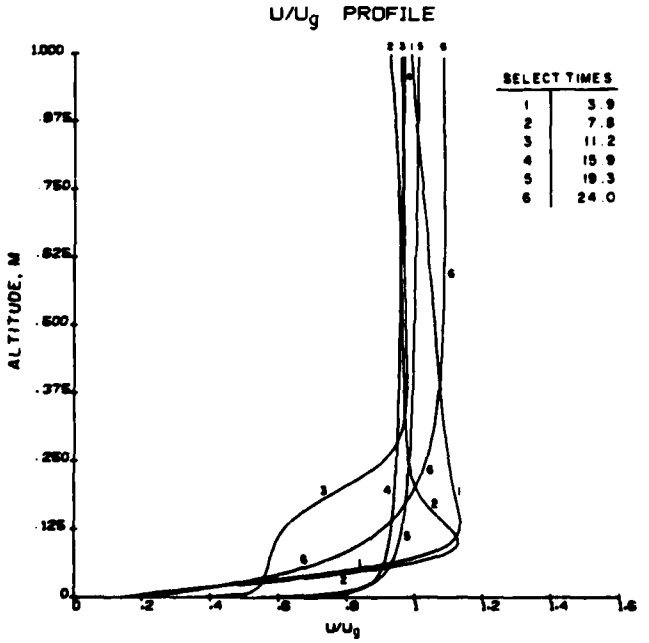

Figure 4.1.2 - Vertical distributions of U taken at select times from a model simulation of a midwestern summer day. Lewellen, et al. (1974).

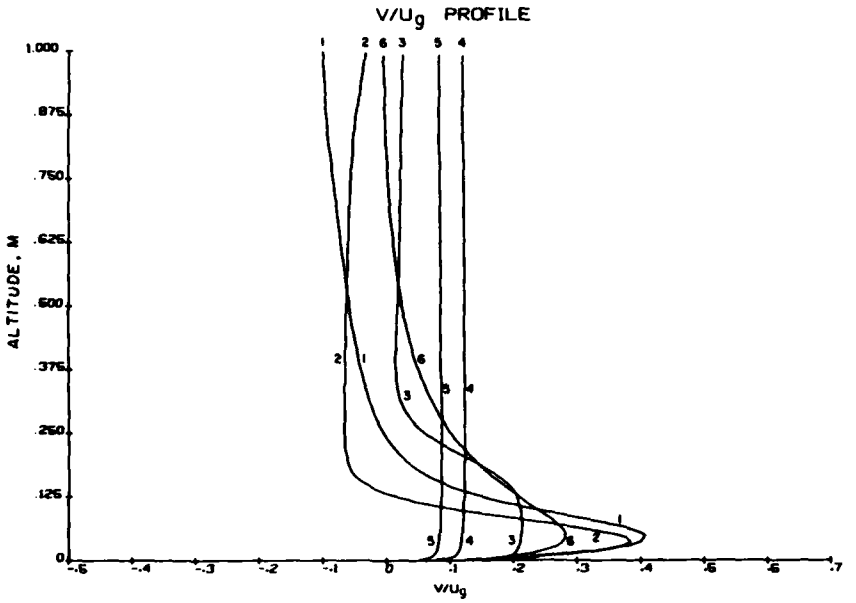

Figure 4.1.3 - The vertical distribution of V taken at the same select times as in Figure 4.1.2.

The predicted contours of constant turbulent fluctuations are presented in Figure 4.1.1 as a function of time and altitude. The boundary-layer thickness grows during the day and shrinks during the evening and morning hours as expected. The turbulent kinetic energy reaches a maximum of 4.8% of the geostrophic mean kinetic energy in the midafternoon at an altitude of approximately 500 m. As the sun sets, the turbulence begins to decay until in the early morning hours the maximum kinetic energy is $\approx 0.25\%$ of the mean kinetic energy. The biggest difference between the results presented in Figure 4.1.1 and those presented by Lewellen, et al. (1974) occurs during the early morning hours. The full equations with a dynamic scale predict a slower decay of q^2 and consequently considerably larger q^2 in the altitude range from 100 m to 1 km in the morning hours. But even this larger value is still quite small compared with afternoon values. Both model representations predict such features as the temperature inversion and local wind jet observed to occur nocturnally at low levels. Figures 4.1.2 and 4.1.3 show the vertical profile of the wind components at selected times for the lowest 1 km altitude. In the plots given in Sections 3.4 and 3.5 for quasi-steady conditions, it was possible to present results in terms of a dimensionless height, zf/U_g. However, in the present case, since the dynamics of the diurnal variation are important in determining the height of the layer at any given time, this nondimensionalization is no longer valid. For Figures 4.1.2 and 4.1.3 the geostrophic wind was held constant at $U_g = 10$ m/sec, the upper level temperature gradient was held constant at $(\partial\theta/\partial z)|_\infty = 3°C/km$, the surface roughness constant at $z_0 = 0.01$ m, and the surface heat flux was allowed to follow an experimentally observed distribution (Wyngaard, 1973). Between sunset and sunrise, the heat flux is a negative constant (-0.025°C m/sec) and between approximately 8:00 am and 8:00 pm, the heat flux is positive and nearly follows a sine wave with a maximum of 0.25°C m/sec. Over the 24-hour cycle, there is a net positive heat flux to the atmosphere which must be removed (in simulation of long wave radiation) in order to achieve a periodic solution with no long-term heating of the boundary layer. In the present run, this was accomplished by assuming Q_r distributed uniformly over the night hours with the following assumed vertical distribution:

$$\dot{Q}_r = -0.703 \times 10^{-4} \cos(\pi z/6000\,\text{m})\,(°C/\text{sec}) \qquad z < 3000\,\text{m}$$

$$\dot{Q}_r = 0 \qquad z > 3000\,\text{m}$$

Figures 4.1.2 and 4.1.3 show the wind shear to be a maximum in the early morning hours when the turbulence, as shown in Figure 4.1.1, is a minimum. There is a low-level nocturnal jet which exceeds the geostrophic wind by 14% at a little above 100 m altitude. The wind at this time drops from 11.4 m/sec to 3 m/sec at 10 m altitude at the same time as the principal wind direction is shifting by 40 degrees.

Surface shear stress is plotted as function of the stability variable $\kappa u^*/fL$ in Figure 4.1.4. Data points for $Ro \simeq 10^7$, as taken from Tennekes' (1973) summary, are included on the plot. The model predictions show a hysteresis loop with the surface shear stress significantly larger when the surface heat flux is decreasing rather than increasing. The data show considerable scatter but tend to be biased toward the upper bounds. The factor of 2 difference in u^* at neutral conditions demonstrates the influence of unsteady dynamics on the atmospheric boundary layer.

A boundary layer data set collected at Wangara, Australia by Clarke, et al. (1971) has been used by a number of investigators to test their model simulations of diurnal variations in the boundary layer. The data set consists of the time and height variation of the two mean velocity components, the mean virtual potential temperature, and the mean water vapor mixing ratio. Profiles of the turbulence quantities are not included. Figure 4.1.5 shows the comparison between observations and computed results for the diurnal variations of the mixed layer height as given by Yamada and Mellor (1975). The qualitative comparison is

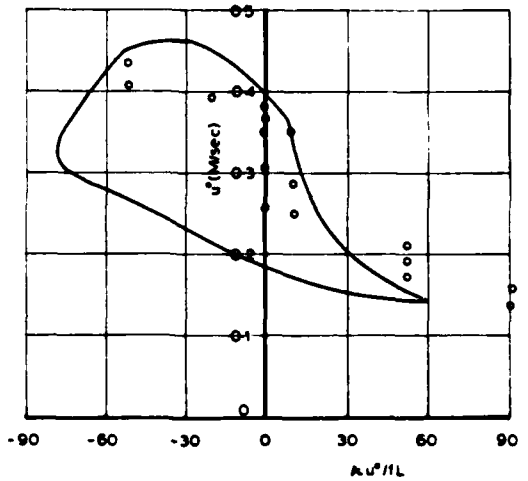

Figure 4.1.4 - Surface shear velocity vs. stability for diurnal planetary boundary layers. Model calculation from Lewellen, et al. (1974); data from Tennekes (1973).

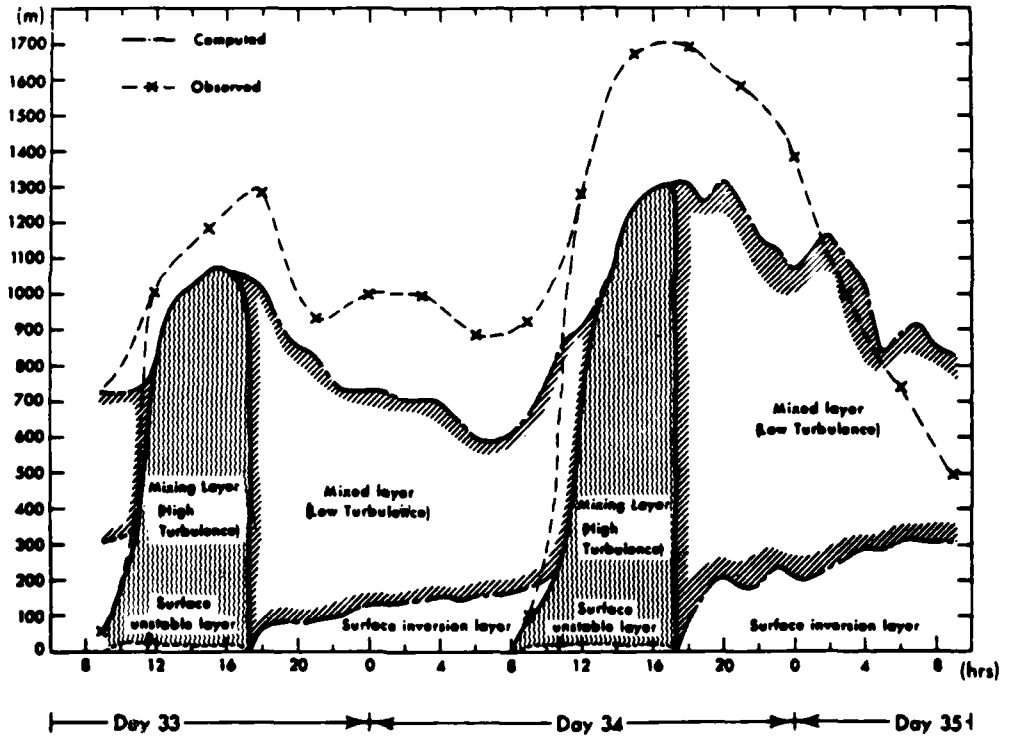

Figure 4.1.5 - Time evolution of the computed and observed mixed layer height as given by Mellor and Yamada (1975).

good, with the strong afternoon turbulence responsible for the observed high penetration of the mixed layer at these times. Mellor and Yamada report that the approximate 300 m discrepancy between the observed and computed boundary-layer depth could probably be attributed to the uncertainties in the observed values of the mean vertical wind which served as input to the model. They concluded that fairly accurate data on both the thermal wind and the mean vertical wind are necessary to obtain realistic simulations of the mean variables.

Andre, et al. (1978) also simulated the Wangara data using their third-order closure model. Comparison between the computed and observed horizontal wind profile during night 33-34 is shown in Figure 4.1.6. The most important feature is the development of the low-level nocturnal jet whose magnitude increases from 9 m/sec at 2100 to 12.5 m/sec at 0300 and then decreases. The behavior is qualitatively reproduced by the model except the low-level jet is approximately 100 m too low. They attribute this discrepancy to uncertainty in the aerodynamic roughness, z_o, since the height of the low-level jet is dependent on the turbulence produced at the surface. They also show that radiative heat transfer becomes more important than turbulent transport above approximately 100 m during nocturnal hours. This will be discussed in Section 4.5.

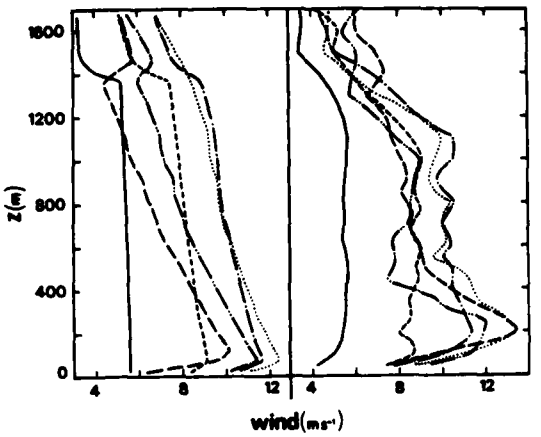

Figure 4.1.6 - Comparison of model calculations by Andre, et al. (1978) with Wangara data. Computed (left) and observed (right) profiles of mean horizontal wind during Night 33-34: ——, t = 18 h; ----, t = 21 h; –·–·–·, t = 00 h; ····, t = 03 h; –··–··–··, t = 6 h; _ _ _ , t = 08 h.

Bodin (1980) claims that fairly simple turbulent closure models such as his turbulent kinetic energy model and Long and Shaffer's (1975) eddy viscosity model do as good a job at simulating the Wangara data as do the more complicated models. This probably is more a reflection of the importance of such diverse phenomena as advection, thermal wind, and radiation in this data set, than it is a verification of the simple turbulent models.

4.2 Influence of Baroclinicity

The approximation of horizontal, spatial homogeneity is seldom completely realized in the atmosphere. One effect which is often encountered is that of horizontal temperature gradients. Fortunately, this effect can be incorporated within a one-dimensional model by permitting the pressure gradient, represented in Eqs. (3.2.1 and 3.2.2) in terms of geostrophic velocities, to vary with altitude. This "thermal wind" variation in the geostrophic wind can be obtained directly from the geostrophic balance by differentiating and using the equation of state

$$\frac{\partial U_g}{\partial z} = -\frac{g}{fT_o}\frac{\partial \theta}{\partial y} \tag{4.2.1}$$

$$\frac{\partial V_g}{\partial z} = \frac{g}{fT_o}\frac{\partial \theta}{\partial x} \tag{4.2.2}$$

with x in the direction of U_g at the top of the boundary layer. Temperature advection could also be included in the energy equation, through a source term of the form

$$\dot{Q} = -u\frac{\partial \theta}{\partial x} - v\frac{\partial \theta}{\partial y} = -\frac{fT_o}{g}\left(U\frac{\partial V_g}{\partial z} + V\frac{\partial U_g}{\partial x}\right) \tag{4.2.3}$$

but this is a less important term. Neglecting temperature advection, this introduces two parameters into the governing equations to specify the magnitude and direction of the geostrophic wind shear (Arya and Wyngaard, 1975). These will be taken herein as

$$M = \left[\left(\frac{\partial U_g}{\partial z}\right)^2 + \left(\frac{\partial V_g}{\partial z}\right)^2\right]^{1/2}\frac{z_i}{(U_g)_{@z=z_i}} \tag{4.2.4}$$

$$\alpha_o = \tan^{-1}\left(\frac{\partial V_g/\partial z}{\partial U_g/\partial z}\right) \tag{4.2.5}$$

Arya and Wyngaard (1975) show that when M and ϕ_0 are steady and the boundary layer is unstable, then most of the imposed thermal wind shear occurs at the top of the boundary layer. Even for only slightly unstable conditions the mean velocity components remain essentially uniform across the "mixed" layer with the wind shear occurring across or above the capping inversion layer. Under these conditions, the principal influence of adding the thermal wind is to increase the wind shear across the inversion layer. This should tend to enhance the potential for shear-wave instabilities above the inversion and a general thickening of this layer.

Conditions which lead to significant values of M in the boundary layer are generally not steady. Lewellen and Williamson (1976) show that whenever the time scale for the development of baroclinicity is of the order of a few hours, as it is likely to be in nature, then the time history of the baroclinicity affects the boundary-layer response. Figures 4.2.1 and 4.2.2 show results for a constant value of M (1.25) and periodic change in ϕ_0 between 0 and 2π over a period of 12 hours. The magnitude of M corresponds to a horizontal temperature change of 3°C in 100 km, a large but not uncommon value in nature. The time variation corresponds to a relatively fast moving temperature anomaly with the flow permitted to become periodic by allowing three full periods of variation before the results shown were recorded. The geostrophic wind was set at 10 m/sec, Ro = 10^6 and no surface heat flux, $Ri_{(10)}$ = 0. An upper level lapse rate of 3°C/km held the boundary-layer thickness to ≈ 1280 m altitude.

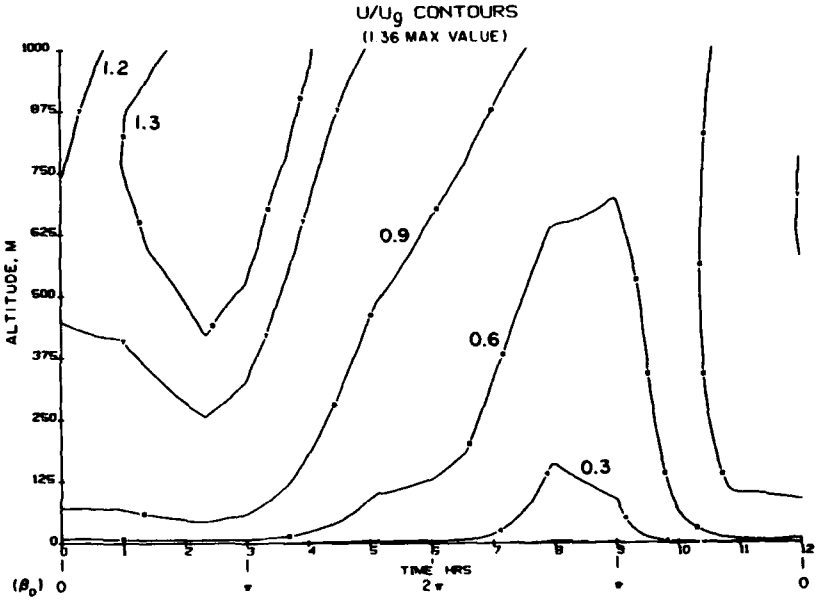

Figure 4.2.1 - Isolines of U for a thermal wind varying periodically in direction [Ro = 10^6, $\partial\theta/\partial z|_\infty$ = 3°C/km, M = 1.25, $Ri_{(10)}$ = 0]. Lewellen and Williamson (1976).

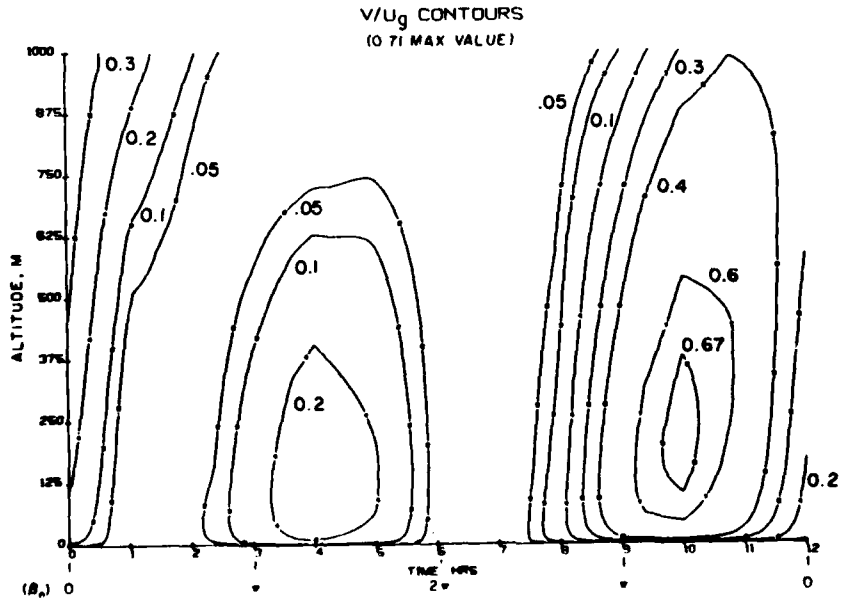

Figure 4.2.2 - Isolines of V for a thermal wind varying periodically in direction [Ro = 10^6, $\partial\theta/\partial z|_\infty$ = 3°C/km, M = 1.25, $Ri_{(10)}$ = 0]. Lewellen and Williamson (1976).

From Figure 4.2.1 it is seen that the maximum U velocity, 13.5 m/sec, occurs approximately 3 hours after the thermal wind is directed in the direction of the geostrophic wind ($\beta_0 = 0$). however, 3 hours after the thermal wind is next directed in the same direction ($\beta_0 = 2\pi$), U is near a minimum. Actually, from Eq. (3.2.1) and Eq. (3.2.2), we see that the U velocity responds to variations in V_g and, since $\partial V_g/\partial z$ follows sin βt, this contributes a positive pressure gradient between $0 < \beta_0 < \pi$ and a negative pressure gradient between $\pi < \beta_0 < 2\pi$. Thus it is consistent for a maximum to occur in U when β_0 passes through π as it is increased, and for a minimum to occur in U when β_0 passes through π as it is decreased. This particular time variation of driving conditions is not expected to occur long enough in nature to make the real flow periodic, but it does demonstrate how important the time history of the flow is in determining the response of the flow to instantaneous values of the driving conditions.

The maximum value of V, 7 m/sec, occurs near the ten-hour mark after the combination of a relative minimum in U and a maximum in U_g has produced a favorable pressure gradient [see Eq. (3.2.2)] for a period of time. There is a region of slightly negative V (approximately -1 m/sec) between 1000 m and 1250 m altitude which does not show in Figure 4.2.2. The turbulence isolines (Lewellen and Williamson, 1976) show no strong variation over the period.

The maximum wind shear at or above 10 m altitude computed by taking the square root of the sum of the squares of $\partial U/\partial z$ and $\partial V/\partial z$ gives a value of 0.14 sec^{-1}, somewhat less than the maximum value (0.18 sec^{-1}) that occurs in the typical diurnal day calculations of the Section 4.1. However, in this case the shear occurs over a somewhat wider altitude range. In the earlier figures the strong local stability caused by surface cooling was the dominant mechanism while, in the present case, there is a neutral, vertical temperature variation in the region of maximum shear. This exemplifies two different ways in which the wind shear may be increased: either by increasing the horizontal wind gradients to increase the driving thermal winds, or by applying a vertical temperature gradient which increases the stability of the flow under the same driving pressure gradients.

In any attempt to simulate conditions in the baroclinic atmospheric boundary layer at a given time and place, it appears desirable to trace the development of the boundary layer for some time prior to the desired time.

4.3 The Marine Boundary Layer

The marine boundary layer, recently reviewed by Lemone (1980), differs in several respects from that over land. The sea surface tends to be quite uniform with relatively slow changes in temperature. Although there are exceptional areas where regions of upwelling, special currents, or coastal influence may permit horizontal temperature gradients of several degrees over a few kilometers, temperature differences over spatial dimensions of the order of tens of kilometers and over diurnal time scales are typically less than a degree. The sea is a fluid lower boundary which interacts with the atmosphere to determine in a coupled manner the effective aerodynamic roughness of the surface. Also the marine boundary-layer air is typically quite moist. In fact the surface buoyancy flux is often determined as much or more by the moisture flux as it is by the temperature flux.

For the marine boundary layer, it is desirable to replace the potential temperature by the virtual potential temperature defined as

$$\theta_v = \theta + 0.61\, T_0\, h \qquad (4.3.1)$$

As long as there is no condensation or evaporation of water within the boundary this replacement permits all the previous equations to be applied to the marine boundary layer. Change of phase will be considered in Section 4.4.

The air-sea surface interaction could rightfully be the subject of another monograph (see, e.g., Coantic, 1978). Many details of this interaction, particularly under conditions of significant sea spray, have not been quantitatively analyzed. The simplest relation with some, at least approximate, general validity is to use Charnock's (1955) Froude number scaling to relate the effective surface roughness to the surface shear stress. When Wu's (1969) data correlation is used to evaluate the constant, this gives.

$$z_0 = 0.016\, u_*^2/g \qquad (4.3.2)$$

The type profiles which typically occur in the marine boundary layer are shown in Figure 4.3.1 from Lemone (1980). A slightly unstable mixed layer capped by a weak inversion is common. Comparison between the heat flux and moisture flux measured by aircraft on one of these days and the results of calculations by the model described by Eqs. (2.3.18 - 2.3.23) are given in Figure 4.3.2 as given by Lewellen, et al. (1977). These comparisons were used to show that the model is roughly consistent with the data. A careful assessment of the accuracy of the model would require a more detailed specification of the experimentally observed boundary layer as it evolves in time.

The most sophisticated attempt at calculating the marine boundary layer is that by Sommeria (1976) and Sommeria and Lemone (1978), using a three-dimensional simulation of the turbulent processes in a manner similar to the calculations of Deardorff (1972, 1974). The biggest difference between their model results and that of the one-dimensional, second-order closure result of Lewellen, et al. (1977), appeared to be a significant difference in liquid water content condensed in the clouds. The role of moisture change of phase is quite important in the marine boundary layer. This is discussed in Section 4.4.

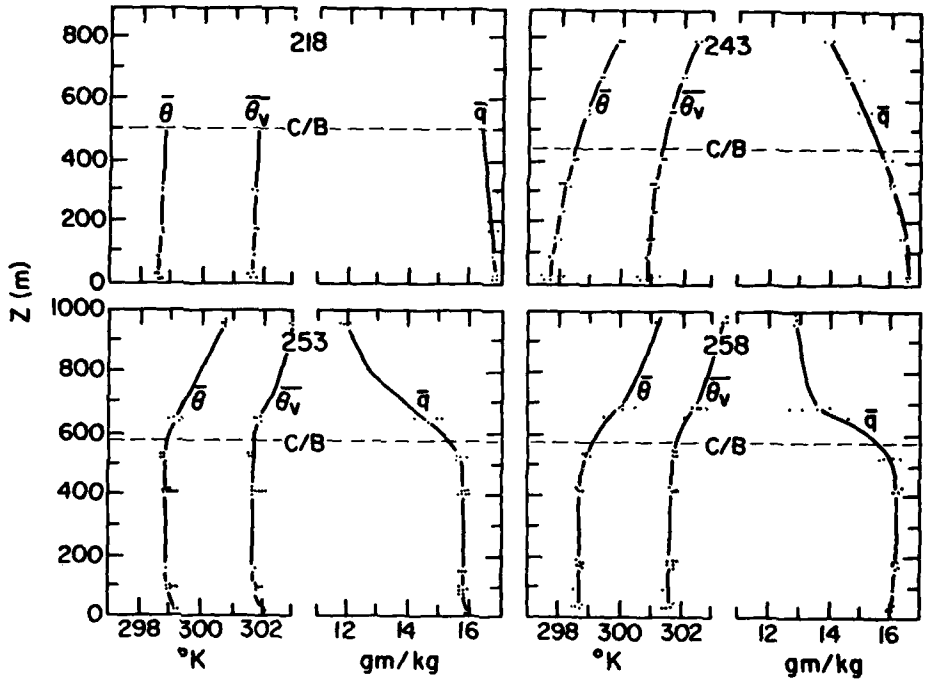

Figure 4.3.1 - Profile of potential temperature, θ; virtual potential temperature, θ_v; and specific humidity, q; for 4 days in GATE, 1974 (Day 218 = 6 Aug.; Day 243 = 31 Aug.; Day 253 = 10 Sept.; Day 248 = 15 Sept. (LeMone, 1980).

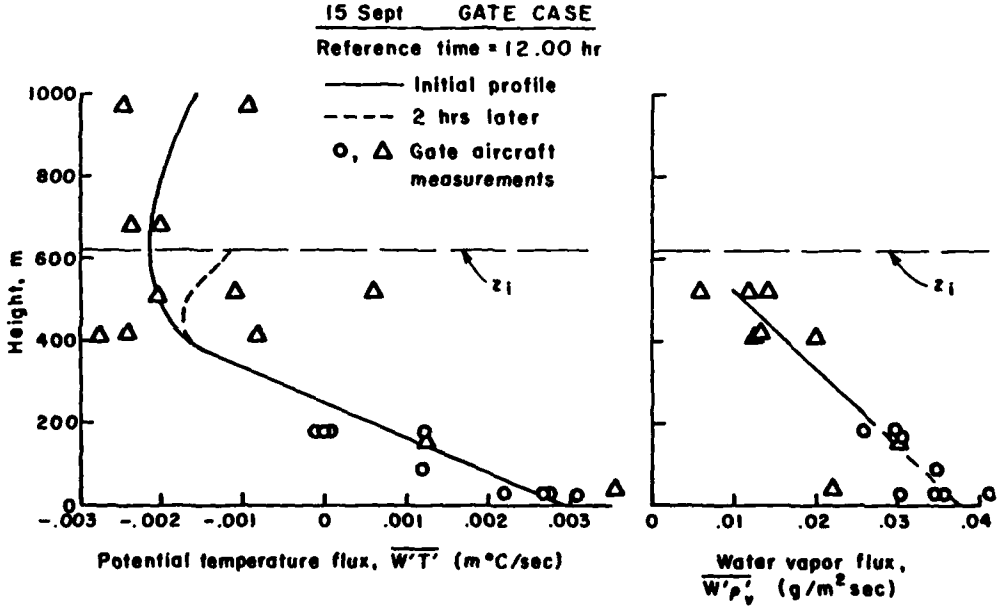

Figure 4.3.2 - Virtual potential temperature and humidity fluxes as calculated by a second-order closure model (Lewellen, et al., 1977), and compared with the GATE measurements (LeMone, 1980).

4.4 Moisture Change of Phase

The latent energy transported through the boundary layer in the form of water vapor is ultimately responsible for fueling most of the large scale atmospheric motions. On a global average basis, the turbulent transport of water vapor through the atmospheric boundary layer must balance the average precipitation of liquid water, about 1 m per year (Coantic, 1978). Even if only a small fraction of the energy released by condensation of the water vapor occurs directly in the boundary layer, this is sufficient to interact strongly with the turbulent structure of the boundary layer when it does occur. The other reason for being interested in the interaction of turbulence with moisture change of phase in the boundary layer is that the phenomena of fog and low-level clouds represent a primary goal of many models.

In the presence of moisture change of phase, the potential temperature is not always the most convenient variable to use in the energy equation, since it is not a conserved quantity. One choice for a conserved quantity is the liquid potential temperature (Betts, 1973, 1974).

$$\Theta_\ell = T - T_0 + \frac{g}{c_p} z - \frac{\mathcal{L}}{c_p} H_\ell \tag{4.4.1}$$

An alternative is the moist static energy.

$$\Theta_s = T - T_0 + \frac{g}{c_p} z + \frac{\mathcal{L}}{c_p} H_v \tag{4.4.2}$$

The difference between Θ_s and Θ_ℓ is the latent energy of the total water content. As long as the total water content is also a conserved quantity, the two are equivalent. In the presence of precipitation, Θ_s is conserved but Θ_ℓ is not.

The buoyancy term in the momentum equation is proportional to the virtual potential temperature defined as

$$\Theta_v = T - T_0 + \frac{g}{c_p} z + (0.61 H_v - H_\ell) T_0 \tag{4.4.3}$$

Thus

$$\Theta_v = \Theta_s + \left(0.61 T_0 - \frac{\mathcal{L}}{c_p}\right) H + \left(\frac{\mathcal{L}}{c_p} - 1.61 T_0\right) H_\ell \tag{4.4.4}$$

so that even with both Θ_s and H conserved, a change of phase of part of H from H_v to H_ℓ leads to a source of Θ_v.

Because of the extensive role Θ_v plays in the turbulent flux equations [Eqs. (2.3.18 - 2.3.21) with Θ_v replacing Θ], Oliver, et al. (1978) chose to stick with Θ_v as a primary variable and introduce the necessary source terms. The energy equation is then replaced by

$$\frac{D\vartheta_v}{Dt} = -\frac{\partial}{\partial x_j}\left(\overline{u_j \vartheta}\right) - K_s \dot{Q}_{rad} + K_g \frac{g}{c_p} W \sigma_{j3} \tag{4.4.5}$$

where K_s and K_g are coefficients generated from the vapor saturation function

$$K_s = \begin{cases} 0 \\ \dfrac{(1 + 1.61 H_s \beta_T)}{[1 + (R_v/c_p) H_s \beta_T]} \end{cases} \tag{4.4.6}$$

$$K_g = \begin{cases} 0 \\ 1 + 1.61 H_s \dfrac{c_p}{R_m} - \dfrac{(1 + 1.61 H_s \beta_T)}{[1 + (R_v/c_p) H_s \beta_T]} \end{cases} \tag{4.4.7}$$

The upper values of K_s,K_g apply for unsaturated conditions and the lower values for saturation conditions. R_v and R_m are gas constants for water vapor and air, respectively. The parameter β_T is the logarithmic derivative of the saturation mixing ratio with respect to temperature. If the saturation formation is given by the Clapeyron relationship

$$H_s = H_{s_\infty} \frac{p_\infty}{p} \exp \frac{\mathcal{L}}{R_v}\left(\frac{1}{T_\infty} - \frac{1}{T}\right) \tag{4.4.8}$$

where the subscript ∞ denotes reference values, then β_T is given by

$$\beta_T = \frac{\mathcal{L}}{R_v T} \tag{4.4.9}$$

Additional terms also need to be added to the heat flux, temperature variance, and temperature-humidity covariance equations. These are:

$$\frac{D}{Dt}\overline{u_i \theta_v} = \ldots + K_g \frac{g}{c_p}\overline{u_i w} \tag{4.4.10}$$

$$\frac{D}{Dt}\overline{\theta_v^2} = \ldots + 2K_g \frac{g}{c_p}\overline{w\theta_v} \tag{4.4.11}$$

$$\frac{D}{Dt}\overline{c_q \theta_v} = \ldots + K_g \frac{g}{c_p}\overline{w c_q} \tag{4.4.12}$$

These additional terms play the role of reducing the effective vertical temperature gradient in the production terms in these equations, i.e., the effective vertical temperature gradient appearing in each of these equations is $[\partial\theta_v/\partial z - K_g(g/c_p)]$. The presence of intense turbulence will force the ambient environment towards a lapse rate of $(K_g - 1)g/c_p$, which is the moist adiabatic lapse rate under saturated conditions, or the dry adiabatic lapse rate under unsaturated conditions. Just as the dry adiabatic lapse rate ($\approx$ -9.8 °C/km) marks the boundary between stable and unstable considerations in a dry environment, the moist adiabatic lapse rate ($\approx$ -3.5 °C/km) marks the stability boundary under saturated conditions. If the ambient virtual potential temperature gradient falls between these two stability boundaries, then a conditional instability exists. As long as the flow remains unsaturated, the flow will remain stable, but if there is a disturbance of sufficient amplitude to allow saturation to be reached at some point, then this disturbance will become unstable.

Just as moisture change of phase has a strong input on buoyantly generated turbulence, turbulence may be expected to have a strong interaction with the microphysics of phase change. A discourse on cloud microphysics is beyond the scope of the present monograph (e.g., see Pruppacher and Klett, 1978), although I believe it is an area where turbulence modeling could fruitfully be applied. The simplest approximation is to assume equilibrium condensation so that the vapor mixing ratio H_v and the liquid mixing ratio H_ℓ are given by

$$H_v + h_v = H + h + (H_s + h_s - H - h)\mathcal{H}(H + h - H_s - h_s) \tag{4.4.13}$$

$$H_\ell + h_\ell = (H + h - H_s + h_s)\mathcal{H}(H + h - H_s - h_s) \tag{4.4.14}$$

when $\mathcal{H}$ is the Heaviside function and $H_s(p,T)$ the saturation mixing ratio given by Eq. (4.4.8).

It is fairly apparent that the ensemble average liquid water content given by

$$H_\ell = \overline{(H + h - H_s + h_s)\mathcal{H}(H + h - H_s - h_s)} \tag{4.4.15}$$

is not equal to the simple form

$$H_\ell = (H - H_s)\mathcal{H}(H - H_s) \tag{4.4.16}$$

because liquid water content is physically a positive definite quantity. The exact specification of the average liquid water content depends on the joint probability distribution factor, $f(H,H_s)$. Sommeria and Deardorff (1977) and Mellor (1977) assumed a joint Gaussian distribution about the mean for the 2 conserved quantites θ_s and H to obtain a result which may be parameterized as

$$H_\ell = \begin{cases} 0 & Q_2 \leq -1.6 \\ \sigma_2 \times (Q_2 + 1.6)^2/6.4 & -1.6 \leq Q_2 \leq 1.6 \\ Q_2 & Q_2 \geq 1.6 \end{cases}$$

where

$$\sigma_z \approx \overline{[(h - h_s)^2]}^{1/2}$$

and

$$Q_z \approx (H - H_s)/\sigma_z$$

Oliver, et al. (1978) adopted a somewhat more approximate procedure. They approximated the average liquid water content as

$$H_\ell = \begin{cases} H - H_s & \Delta < |H - H_s| \\ \frac{1}{2}(H - H_s + \Delta) & \Delta \geq |H - H_s| \end{cases} \tag{4.4.17}$$

where Δ is a characteristic measure of the size of the fluctuations which may be partially saturated and partially unsaturated:

$$\Delta = \overline{(h^2)}^{1/2} + \overline{(h_s^2)}^{1/2} \tag{4.4.18}$$

The functions H_ℓ/σ_z and H_ℓ/Δ are quite similar functions of Q_z and $[H - H_s)/\sigma$, but $\Delta \geq \sigma_z$ so that the latter approach leads to a broader transition region and more liquid water content over most of the transition layer.

Water droplets are diffused by turbulence in the same manner as a gaseous species as long as the particle is sufficiently small that it can faithfully follow all of the turbulent eddies. This will be true whenever the relaxation time of the particle τ_v, the time required by a particle to reduce its velocity relative to the gas by e^{-1} when acted upon by the fluid drag only, is much less than the eddy time scale Λ/q. Table 4.4.1 gives some values of τ_v for different size particles with a density of 1 gm/cm^3. Since Λ grows proportional to z near the surface, it is possible to estimate the height at which $q\tau_v/\Lambda = 1$ for a given value of q (1 m/sec). At large distances above this height, there should be no difference between the turbulent diffusion of a particle and the turbulent diffusion of a gaseous species. For cloud droplets with diameters less than approximately 10 microns, the table indicates that the only region where the particulate nature will generally make any difference to diffusion is within the surface sublayer. When the droplet stopping distance is of the order of the turbulent microscale, or larger, efficient deposition of fog droplets on the surface may be expected. It can also be seen from Table 4.4.1 that the gravitational settling contribution to deposition velocity will only be important for droplets of the order of 10 μm or larger.

Table 4.4.1. Aerosol Transport Properties

(Spherical particles with $\rho_A = 1$ gm/cm^3 in air at 20°C, 1 ATM; and q = 1 m/sec)

Particle diameter $2a$ (μm)	Relaxation time τ_v† (sec)	Terminal velocity $\tau_v g$ (cm/sec)	Height at which $q\cdot\tau_v/\Lambda = 1$ (m)	Stopping distance microscale $q^2\tau_v/2\nu$
0.1	8.8×10^{-8}	8.6×10^{-5}		2.9×10^{-3}
0.5	1.0×10^{-6}	1.0×10^{-3}		3.3×10^{-2}
1.0	3.6×10^{-6}	3.5×10^{-3}		0.12
5	8.0×10^{-5}	7.8×10^{-2}	12.3×10^{-5}	2.7
10	3.2×10^{-4}	3.1×10^{-1}	5×10^{-4}	10.6
50	7.7×10^{-3}	7.58	0.012	2.6×10^{2}
100	3.1×10^{-2}	30.3	0.048	1.0×10^{3}

† Friedlander (1977)

4.5 Thermal Radiation

The principal mode of transport of energy through the atmosphere is via thermal radiation, but the relative transparency of the general atmosphere allows this energy to typically pass through a layer of the order of 1 km thick without a strong interaction. Of course, the thermal radiation balance always plays an important role in controlling the surface temperature and thus, at least indirectly, plays a deciding role in determing the stability of the boundary layers as discussed in Chapter III. However, under some conditions, particularly those involving fog or low-level clouds, thermal radiation absorption depths may be greatly reduced and permit a strong interaction between turbulent transport and thermal radiation within the atmospheric boundary layer. Also under nocturnal, clear sky conditions, the radiation flux divergence may be stronger than the divergence of the turbulent heat flux. Thus, a general model of the atmospheric boundary layer needs to at least include thermal radiation in the mean energy equation. The extent to which radiative terms need to be included in the temperature correlation equations remains unresolved. Andre, et al. (1978) argue that a radiative dissipation term in the temperature variance equation is important for simulating the nocturnal boundary layer under even clear conditions as long as there is sufficient water vapor present.

In formulating a description of radiant heat transfer, it is convenient to separate the direct solar (short wavelength) from the terrestrial (long wavelength) fields. Each of these fields may be described in terms of the one-dimensional (z) upward and downward frequency and angular averaged radiation intensities F^+, F^-. These intensities are governed by the upward and downward transport equations in integral form (Goody, 1964):

$$F^+(z) = [F^+(z_0) - \mathcal{E}(z_0)]\,\tau(z_0,z) + \mathcal{E}(z) - \int_{z_0}^{z} \tau(z',z)\,\frac{\partial \mathcal{E}}{\partial z'}\,dz' \tag{4.5.1}$$

$$F^-(z) = [F^-(z_h) - \mathcal{E}(z_h)]\,\tau(z_h,z) + \mathcal{E}(z) - \int_{z_h}^{z} \tau(z',z)\,\frac{\partial \mathcal{E}}{\partial z'}\,dz' \tag{4.5.2}$$

The boundary values at the surface $z = z_0$ and boundary layer "top" $z = z_h$ are $F^+(z_0)$ and $F^-(z_h)$, respectively. The radiative cooling rate, Q_r is given in terms of F^+, F^- for either radiation field as

$$Q_r = \frac{\partial}{\partial z}(F^+ - F^-) \tag{4.5.3}$$

and the total radiant heat flux is the sum of the direct solar heat flux and the terrestrial heat flux.

The absorption, scattering, and emissive properties of the atmosphere must be embedded in the source function $\mathcal{E}(z)$ and the transmission function $\tau(z_1,z_2)$ between two levels z_1,z_2. A simple analysis neglecting scattering of direct solar radiation was given by Oliver, et al. (1978). Their analysis demonstrates that the influence of liquid water on the transmission function τ is quite different for solar radiation than it is for terrestrial radiation. For solar radiation the transmission function τ is modeled after Manabe and Strickler (1964) for water vapor and CO_2. To account for liquid water, a transmission $\tau^S_{liq}(z_1,z_2)$ was included as a factor in the total transmission τ of the form

$$\tau^S_{liq}(z_1,z_2) = \exp(-\beta_r \alpha^S m) \tag{4.5.4}$$

where m is the absorbing mass

$$m = \int_{z_1}^{z_2} H_\ell\,dz \tag{4.5.5}$$

β is the diffusivity factor, and α^S is the specific absorption coefficient for direct solar radiation by water droplets. Feigel'son (1964) notes the solar absorption is not sensitive to droplet size for wavelengths < 2 μm. Integrating the spectral liquid water absorption coefficient tabulated by Feigel'son over the direct solar spectrum, gives

$$\alpha^S = 16\ \text{cm}^2\text{g}^{-1}$$

For the terrestrial field, the transmission function for water vapor and CO_2 follows that of Feigel'son (1970) with the liquid water transmission included as a factor in the transmission τ of the form

$$\tau^T_{liq} = \exp(-\mathcal{a}^T m) \tag{4.5.6}$$

Here $\mathcal{a}^T$ is the averaged liquid water absorption coefficient for terrestrial radiation which depends strongly upon the droplet size distribution ranging in value from 200 to 1700 $cm^2 g^{-1}$ (Feigel'son, 1970) for spectral width average drop size radii ranging from 4.5 to 7 μm. The droplet size effect on radiative absorption may be maintained as a parameter through $\mathcal{a}^T$. Detailed inclusion of variation with droplet size requires prediction of the droplet number density within a cloud or fog as well as the liquid water content. Experimental evidence (Mack, et al. 1974) does not validate the simplifying assumption of uniform droplet density in space. Their observations indicate an order of magnitude variation in droplet number density through the boundary layer while mean droplet size varies by about 30%. A characteristic value of $\mathcal{a}^T$ for fog and stratus (mean drop radius ~ 6 μm) is 600 $cm^2 g^{-1}$.

The significant difference between the absorption coefficients $\mathcal{a}^S$ and $\mathcal{a}^T$ is noteworthy. The absorption coefficents may be represented in terms of absorption lengths as

$$\ell^T_{rad} = \frac{1}{\mathcal{a}^T \rho \langle H_\ell \rangle}, \qquad \ell^S_{rad} = \frac{1}{\mathcal{a}^S \rho \langle H_\ell \rangle}, \tag{4.5.7}$$

which are exhibited in Table 4.5.1 for various (spatial) average liquid water contents (H_ℓ). These values indicate that water is radiatively more active with the terrestrial spectrum than the direct solar spectrum for drops in the 4-10 μm range typical of fog and cloud. This sharp difference in radiative emission/absorption in the terrestrial and solar spectrum influences strongly the structure of cloud/fog cooling and the mechanism by which direct solar radiation evaporates away clouds or fog. These implications are discussed in the following sections.

Appropriate boundary conditions for terrestrial radiative transport are $F^- = 0$ at the upper boundary, and $F^+ = B_0$ (B_0 is the blackbody flux) at the surface. For direct solar radiation, F^- is specified as the incident downward solar flux at the upper boundary and $F^+ = \Gamma F^-$ at the surface, where Γ is the surface reflectance. If the upper boundary for radiative transport is set at the atmospheric scale height, the average liquid water content and average water vapor content of the atmosphere contained within the radiative boundary layer above the top of the atmospheric boundary layer must be specified.

Table 4.5.1. Radiative absorption depths for fogs and stratus.

$$\ell^{S,T}_{rad} = [\mathcal{a}^{S,T} H_\ell]^{-1}$$

	Average liquid water contents H_ℓ ($g\ kg^{-1}$)	Direct solar radiation ℓ^S_{rad} (m)	Terrestrial radiation ℓ^T_{rad} (m)
Tenuous fog	0.025	20,000	600
	0.1	5,500	167
	0.2	2,700	83
	0.4	1,350	41
Dense stratus tops	0.8	700	21
	1.0	500	16

4.6 Fog

Shallow fogs in which turbulent transport dominates radiative transport may be modeled as a straightforward extension of the surface layer analysis considered in Section 3.1. In the absence of radiation and precipitation, the equations for θ_s and H are similar to one another; both their mean equations and the turbulent correlation equations. Thus, the distribution of $\theta_s - \theta_{so}$ and $H - H_o$ as well as their turbulent correlations should be similar within the surface layer, and functions of z/L and z/z_o only. As essentially noted by Taylor (1917), all fluid states in the surface layer should map onto a straight line in the $H - \theta_s$ plane which passes through the surface (H_o, θ_{so}), and has a slope determined by the ratio of the surface humidity flux to the heat flux, H_*/θ_{s*}.

For saturated conditions at the surface, Oliver, et al. (1978) showed that surface fog is only possible for a cold surface,

$$\theta_{s_*} < 0 , \quad \text{if } H_*/\theta_{s_*} > \beta_0 \tag{4.6.1}$$

or for a warm surface

$$\theta_{s_*} > 0 , \quad \text{if } H_*/\theta_{s_*} < \beta_0 \tag{4.6.2}$$

where β_0 is the thermodynamic derivative with respect to θ_s of the saturation curve H_s.

$$\beta_0 = \left(\frac{\partial H_s}{\partial \theta_s}\right)_p = \frac{H_s}{T_r}\frac{\mathcal{L}}{R_v T}\left(1 + \frac{H_s}{c_p}\frac{\mathcal{L}^2}{R_v T^2}\right)^{-1} \tag{4.6.3}$$

The fog regimes defined by Eqs. (4.6.1-4.6.3) are exhibited in Figure 4.6.1 as a function of surface temperature and the relative humidity and temperature of the air at some distance above the surface.

An illustrative family of fog distributions as given by the similarity functions Eqs. (3.1.9) and (3.1.11) is shown in Figure 4.6.2. Of particular interest is the structure of the liquid water profiles in the fog layer for stable ($\zeta > 0$) and unstable ($\zeta < 0$) regimes. Stable fog layers have maximum H_ℓ close to the surface, and drop off sharply in liquid water content up to their maximum depth. Unstable layers are well-mixed and do not show a pronounced maximum except for very thin layers $\delta/L \ll 1$. Both families of fogs deepen, and their maximum liquid water contents increase as their flux ratios H_*/θ_{s_*} depart more from the critical value β_0.

Under what conditions will the surface fog layer be influenced by radiative as well as turbulent transport? The surface turbulent heat flux will be determined by the temperature gradient in the surface layer; but this gradient will also determine the maximum liquid water developed in the fog layer and hence, the radiative emission from the layer. For a radiatively thin fog layer ($\delta/l_{rad} \ll 1$), it is possible to estimate the radiative to turbulent heat flux for the fog layer as

$$\frac{q^{rad}}{q^{turb}} \approx \frac{4(\alpha^T \delta)(\hat{\sigma}T^4/C_p)(\beta_0 - H_*/\theta_{s*})\ \ell n(\delta/z_0)}{u_*} \tag{4.6.4}$$

For a nominal condition of a 300 K surface, $[\beta_0 - H_*/\theta_{s*}] \approx 2 \times 10^{-5}$, and $\alpha^T \approx 500$ cm^2/gm,

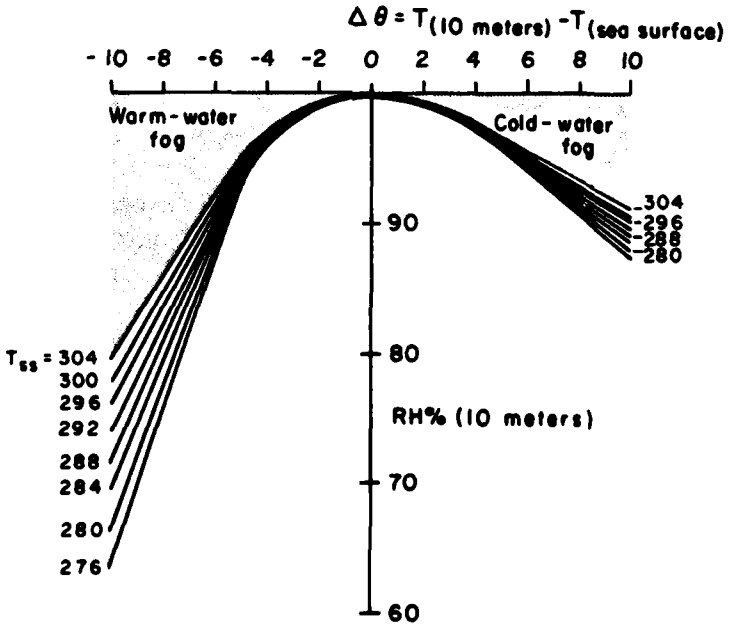

Figure 4.6.1 - Schematic showing the air relative humidity and air-sea temperature differences required for pure advective fogs.

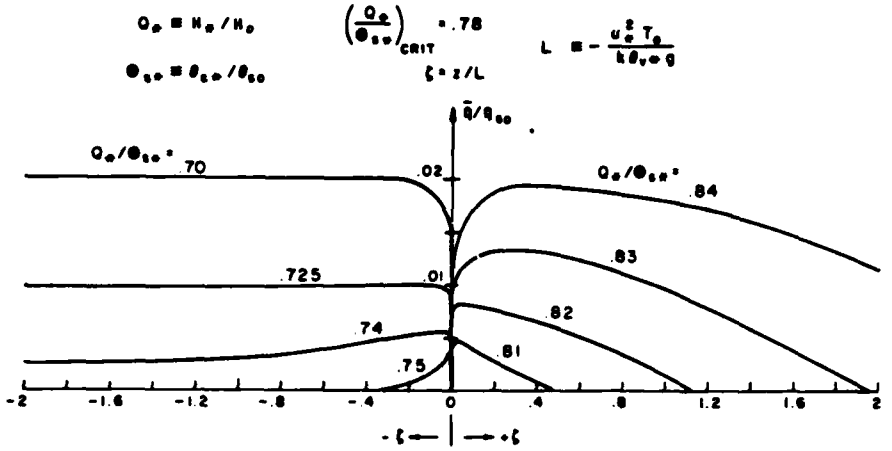

Figure 4.6.2 - Illustrative liquid water distribution in stable ($\zeta > 0$) and unstable ($\zeta < 0$) surface layer advective fogs, Oliver, et al. (1978).

$$\frac{q^{rad}}{q^{turb}} \approx \frac{\delta \ln(\delta/z_0)}{2000 u_*} \tag{4.6.5}$$

a result which depends only upon the strength of the wind and the depth of the fog. It takes a relatively strong wind to make q_{rad} negligible compared to q^{turb}. For δ = 10 m, and $z_0 = 10^{-3}$ m, a surface shear velocity of $u_* = 0.6$ m s^{-1} (corresponding to a neutral wind at 10 m, of 14 ms^{-1}) or greater is required to make q^{rad} less than 10% of q^{turb}. Thus, radiation plays a significant role in most surface fogs of depths greater than a few meters.

It is necessary to return to the full turbulent-radiative description to illustrate the general case of fog formation with both radiant and turbulent transport. Oliver, et al. (1978) used the model described in Sections 4.3 through 4.5 to predict the formation and structure of a commonly observed class of coastal fogs over water in which convection and radiation play equally important roles. Fogs are frequently found to occur in coastal regions subject to stong upwelling and nonuniform surface temperatures where winds bring the surface air from a region of cold water onto a region of warmer water (warm surface fog). Such fogs have been reported and documented by Mack, et al. (1973) and Leipper (1948). A stable, steady boundary layer running from constant temperature water to a region of linearly increasingly surface temperature provides an archetypal example of such advective-radiative fogs. As a result, an unstable mixed layer will be initiated, and fog may form in the newly developing layer.

The incident profiles for this illustration are characterized by a flux ratio of $H_*/\theta_{v*} = 0.00015$ under conditions where

$$\left(\frac{H_*}{\theta_{v*}}\right)_{crit} = 0.0006 .$$

The full profiles are determined by a wind velocity of 2.8 ms^{-1} and an absolute temperature difference of +1°C at z = 20 m elevation above the sea surface of T = 13°C. Thus, the incident flow is in the cold surface fog-free regime. Direct solar radiation was suppressed (simulating nighttime conditions). The surface humidity was maintained at its saturation value at the surface temperature. Surface temperature linearly increases from the origin by 0.5°C in 3 km. The response of this layer is shown in Figure 4.6.3. The combined action of increasing surface temperature and radiative cooling generates a fog layer which grows as the air is convected over the warmer water. Near the origin of the change in surface temperature (x = 100 m), a thin fog layer of about 18 m depth exists with maximum liquid water content just above the surface. At 1000 m the layer is 100 m deep. At this depth, the liquid water content has developed two relative maxima - one near the surface and one near the fog top. This is because the 100 m deep fog band is no longer radiatively thin, and fog-top radiative cooling is beginnning to dominate over surface radiative cooling. The early stages of a temperature inversion formation at the top of the fog band are also in evidence.

After the change from stable to unstable conditions, and the onset of radiative cooling, the local H_*/θ_{v*} shifts to a value of 0.0008. Such a flux ratio places a turbulent dominated layer in the warm surface fog-free regime. Fog, nevertheless, exists in such a layer because of the radiative cooling present. A convenient measure of the effect of radiation in a fog layer of thickness δ is an effective radiative flux θ_*^{rad} defined as

$$u_* \theta_*^{rad} = \frac{1}{\rho C_p} \int_0^{\delta} \frac{\partial q^{rad}}{\partial z} \, dz .$$

Direct comparison of θ_{*}^{rad} with θ_{s*} provides an assessment of the strength of radiation transport compared to turbulent transport in the fog layer. For this warm surface advection fog, $\theta_{*}^{rad}/\theta_{s*}$ is ~ 0.5. The role of radiation is therefore pivotal in its evolution.

The structure of radiative cooling in the fog is shown in Figure 4.6.4. In the first 1000 m, maximum radiative cooling is concentrated at the surface, but then begins to shift upward into the center and top of the cloud bank as it becomes radiatively thick to terrestrial radiation. The turbulence level depicted in Figure 4.6.5 shows a steady increase with x as the unstable mixed layer grows with the maximum turbulence levels concentrated in the center of the cloud bank.

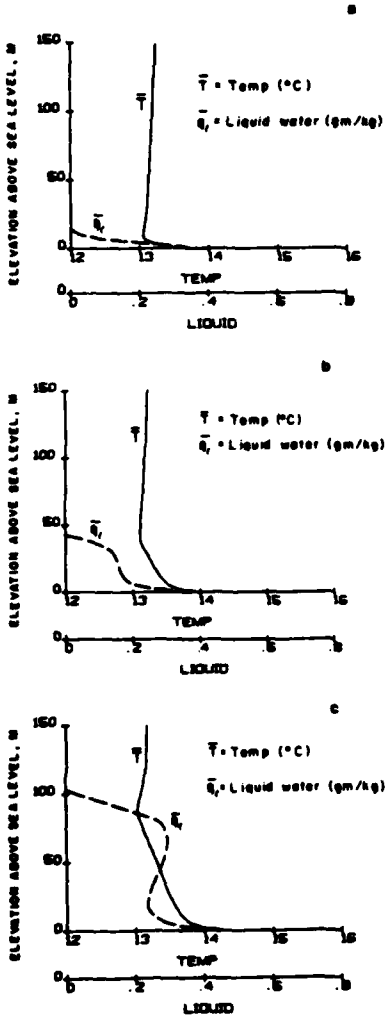

Figure 4.6.3 - Temperature and liquid water content profiles in an advective-radiative fog at x = 100 m (a), x = 1000 m (b), and x = 3000 m (c). Oliver, et al. (1978).

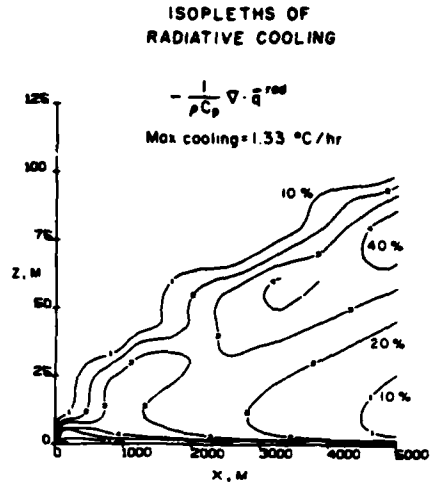

Figure 4.6.4 - Radiative cooling distribution in advective-radiative fog. Note shift of maximum cooling rate away from surface to top of cloud bank as fog bank becomes radiatively thick ($\delta \geq \ell_{rad}$). Oliver, et al. (1978).

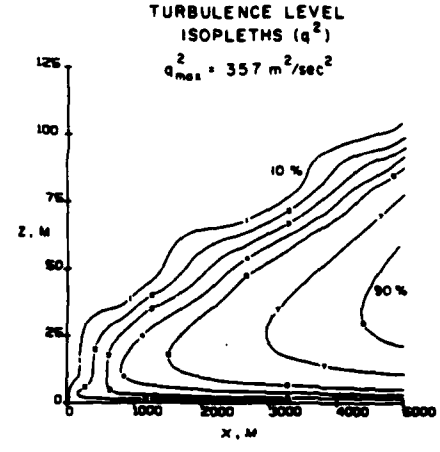

Figure 4.6.5 - Turbulence (q^2) distribution in advective-radiative fog of Figures 4.6.3 and 4.6.4.

4.7 Boundary Layer With Stratus Cloud

A boundary layer over a large expanse of water capped by a subsidence inversion will turbulently ingest moisture from the surface. Long-wavelength cooling of the water-vapor-laden air may then lead to condensation somewhere within the layer. Calculations using relatively similar turbulence closure models have been made by Oliver, et al. (1978), Yamada and Mellor (1980), and Moeng and Arakawa (1980). In an expansive basin or region influenced only by advection in the form of a steady subsidence, a periodic steady state may form in which a solar driven diurnal cycle exists about a mean boundary layer state with a steady mean inversion height controlled by the radiative conditions (season and latitude), surface temperature, and upper conditions (wind, water content and subsidence) set by the larger circulation. Such an episode was illustrated by Oliver, et al. (1978) for conditions approximating the summer stratus layer off the coast of California.

The conditions for this illustration were selected to generally conform to the conditions described by Neiberger (1944), and more recently observed by Mack, et al. (1974). Surface boundary conditions are established for a fixed temperature sea state of 17°C, surface water mixing ratio at saturation, and surface roughness determined by Froude scaling. Radiation conditions are for latitude 40°N at summer soltice. Geostrophic conditions set an upper level wind, Ug, of 10 ms^{-1} and subsidence whose characteristic value is 0.5 x 10^{-5} s^{-1} (Neiberger, et al. 1961; Lilly, 1968). Initial conditions (which will be lost after several days of simulation) were selected to correspond to a mildly stable temperature profile with a lapse rate $\partial\theta v/\partial z$ = 0.003°Cm^{-1} and a clear sky with an initial relative humidity of 0.9. The calculation is begun shortly before sunset the first day and runs for six days. Behavior during daylight hours must be considered somewhat approximate in this illustration, because droplet scattering of direct solar radiation which would reduce solar penetration into the cloud interior was neglected.

The quasi-periodic evolution of cloudiness in the boundary layer is shown in Figure 4.7.1. The stratus grows both downward and upward during nocturnal periods and thickens until sunrise, when the solar heating begins to disperse the stratus. Radiative cooling is dominant at the cloud top and produces an unstable lapse rate within the cloud. A correspondingly enhanced turbulence production is also maximum in nocturnal periods and in the upper portion of the cloud. The radiation cooling at the cloud top strengthens the capping inversion which oscillates up and down over the period of the diurnal cycle.

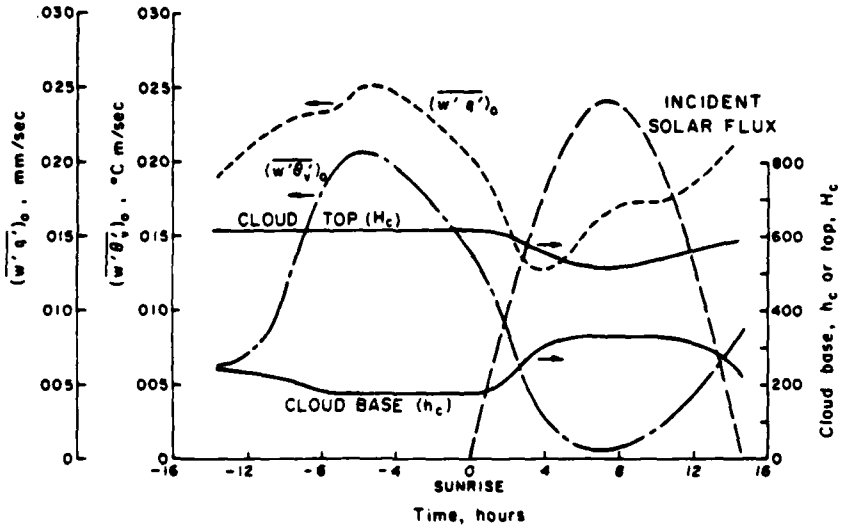

Figure 4.7.1 - Diurnal variation of cloud base and top and heat and moisture fluxes at surface. Oliver, et al. (1978).

We note that the predicted cloud base in these diurnal cycles is highest in late afternoon and lowest in early morning (Figure 4.7.1), while cloud top is highest in early morning and lowest in late afternoon. Correspondingly, the inversion height is highest in early morning and lowest in late afternoon - a result which is opposite to that in Section 4.1 for inversion height cycles driven by solar heating in the cloud-free boundary layer. This predicted result is in accord with the stratus observations of Neiberger (1944) as well as those of Mack, et al. (1974) in which they detected a diurnal variation of inversion height in the presence of California coastal stratus which regularly showed maxima in the early morning. It is, of course, the radiative-turbulent drive of cloud-top cooling which allows the radiating layer to propagate condensation upward during the night while turbulence cools the cloud interior below.

Some summary aspects of this illustration in comparison with the observations of Mack, et al. (1974) which guided the choice of boundary conditions are as follows. The typical liquid water content of the theoretically generated stratus was 0.1-0.2 g/kg compared to 0.1-0.3 g/kg observed. The average height of the stratus base was 50-200 m (theoretical) compared to 0-200 m (observed). The average height of stratus tops at maximum inversion were 600-800 m both predicted and observed. The theoretically predicted cooling rate 100 m below cloud top between 0100 and 0300 local time for the last two days of the simulation was 0.023°Ch^{-1} compared to values of 0.025°Ch^{-1} between 0100 and 0500 observed. The amplitude of the vertical diurnal motion of the cloud base was 100-150 m predicted, compared to observations of 50-150 m.

We have seen that radiative-turbulent coupling of subsidence capped stratus layers propagates the base downward during nocturnal cooling. If the base propagates completely to the ground, a fog is formed at the surface. This class of fog event is common in coastal California during periods of strong subsidence and has been described by Leipper (1948) and Mack, et al. (1974). Several atmospheric fluid mechanisms have been postulated to explain this class of fog event including vertical convection driven by the sea-breeze land-breeze cycle (Neiberger, 1944), and radiative cooling of stratus during the night (Mack, et al. 1974). The single necessary condition all observers note for this class of fog is the existence of the late afternoon or early evening inversion height at about 400 m or lower. The typical clear summer afternoon temperature profile is as indicated in Figure 4.7.2, as measured by Mack, et al. (1974). A strong upper inversion exists above the inversion height z_i with lapse rate γ_u typically about 0.04°Cm^{-1}. A transition region of thickness Δz=40 m exists above z_i with lapse rate of 0.01°Cm^{-1}, while below the inversion, the lapse rate is -0.015°Cm^{-1}. Figure 4.7.3 shows the resulting liquid water content contours of a calculation which begins with such an initial profile over a fixed sea surface state, as calculated by Oliver, et al. (1978). Initial relative humidity is 0.97 in the region up to the inversion falling off to a value corresponding to a mixing ratio of H = 0.001 over the region of the transition zone. The calculation was done for solar inclination at solstice and begun at 1900 local time.

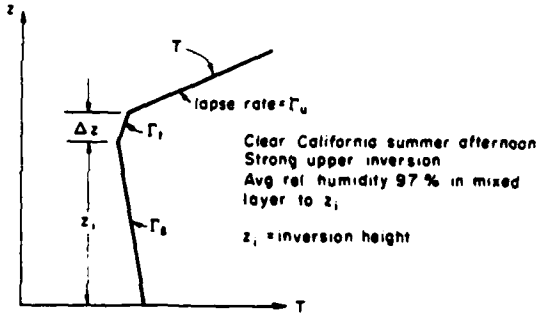

Figure 4.7.2 - Typical late afternoon temperature profile measured by Mack, et al. (1974).

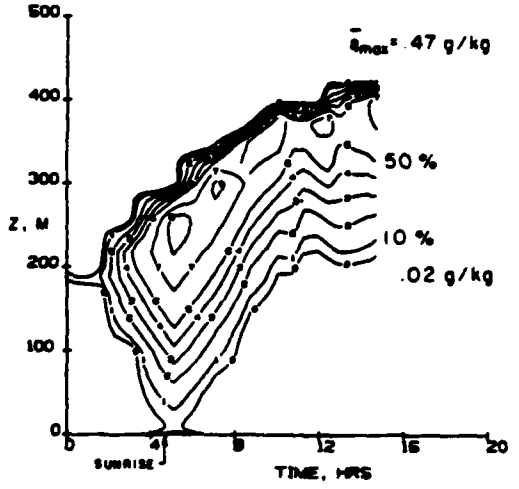

Figure 4.7.3 - Evolution of fog resulting from the lowering stratus. Fog shows some tendency to form at surface just before downward propagating stratus reaches the surface. Oliver, et al. (1978).

The measurements of Mack, et al. (1973) of liquid water content in stratus lowered to the surface and for conditions typical of the present calculation indicate liquid water content ranging from 0.1 to 0.2 g/kg and increasing from the surface upward into the cloud. This trend is consistent with the calculated results, although the calculated water content near the surface is less than measured most likely due to the presence of drizzle in the measured case.

There is a large difference between direct solar and terrestrial absorption lengths. Because of the strong terrestrial absorption and emission of the water droplets, the cloud top is in strong radiative cooling which dominated over solar heating even in daylight hours. Direct solar radiation is absorbed much deeper within the cloud interior. Evaporation by solar heating occurs rather uniformly throughout the cloud because of the long absorption length for solar radiation. Strong cloud-top cooling brought about by the short terrestrial absorption length provides the instability and turbulence production machinery for the cloud to turbulently transport the heat deposited by the sun in its interior. The details of this turbulent transfer can be seen in Figure 4.7.4 where the turbulent heat flux is shown directed from cloud base to cloud top. It should also be noted that heat flows turbulently downward above the cloud top to the strong radiatively cooling surface. This heat flux is supported by the turbulence which has diffused a few tens of meters above the cloud top into the strongly stable region above the cloud.

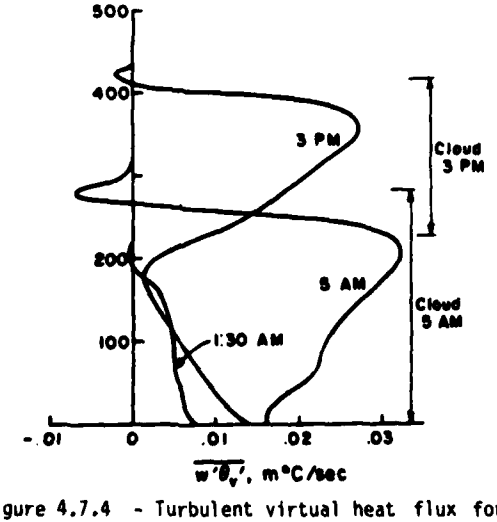

Figure 4.7.4 - Turbulent virtual heat flux for stratus lowering fog at time of stratus formation (0130), lowering to surface (0500), and lifted state (1500). Oliver, et al. (1978).

It is noteworthy that the corresponding turbulent moisture flux is always positive, representing a continuous flow of water from the sea surface upward into the cloud. At no time (after stratus formation) during the course of lowering and raising is the water flux negative, indicating a diffusion of water downward from the cloud to the region below the base. Hence, the relative downward flow of water from a radiatively cooling cloud could only take place by precipitation which is not included in the present calculation. Precipitation transport of water down to the subcloud region will enhance the liquid water level in that region. It also provides a mechanism for the removal of liquid water.

The calculations provide some insight as to the appropriateness of the entrainment hypotheses upon which simple cloud-top mixing models are based (e.g., Lilly, 1968; Schubert, 1976). In Figure 4.7.4, the distribution of the turbulent heat flux in diurnally varying stratus indicates that the virtual heat flux has a positive definite average over the layer and through the cloud top where a small region of negative flux exists. Thus, Ball's hypothesis that the average should vanish (Ball, 1960) and the corresponding maximum entrainment condition which follows from it, are not descriptive of a cloudy layer. This turbulent-radiative model indicates that, on average, radiative transport is as important as turbulent transport in the subcloud region.

The overall turbulence levels are shown in Figure 4.7.5. In the early morning when stratus covers only a small portion of the initial mixed layer, the turbulence levels have a typical dry mixed-layer structure. After the cloud base rises, the confinement of radiative cooling to the cloud top and the presence of heating in the cloud interior skews the distribution to concentrate and locate the maximum turbulence levels near the cloud top.

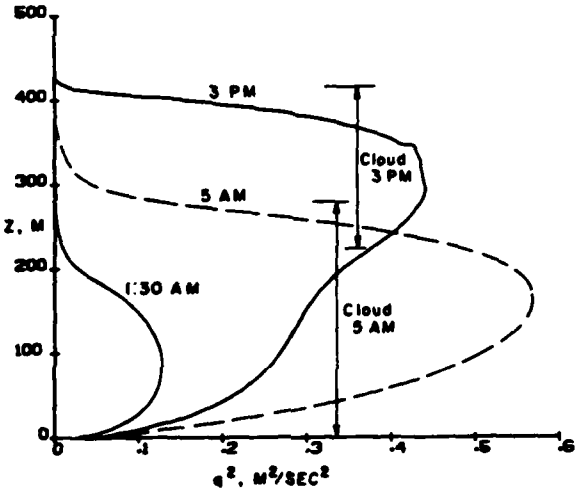

Figure 4.7.5 - Turbulence levels in a stratus lowering fog at the times and conditions of Figure 4.7.4.

This calculation indicates that radiation cooling and the corresponding turbulence production it effects at a stratus top, cools the atmosphere, and propagates the cloud top upward and cloud base downward. The effective region over which the cloud base may be propagated away from the top by turbulence production at the top during the nocturnal period is determined by the long-wavelength radiation absorption length and by the turbulent scale length over which turbulence may be diffused downward from the top of the base. For these typical stratus conditions used as the basis of the calculation, we find the region to be 350 m (Figure 4.7.3). The empirical observation that the downward propagating stratus base can reach the ground during nocturnal cooling, while the cloud top is at 400 m or lower, is quite consistent with this result.

Thermal radiation has been shown to play a significant role in atmospheric fog and stratus cloud events. Illustrations of the dynamics of a turbulent, radiatively coupled low-level atmosphere for warm water fog and subsidence-capped stratus show consistent quantitative features found in observations of such fog and cloud. Inversion heights with cloud in the boundary layer are predicted to have maxima in early morning and minima in late afternoon in contrast to the diurnal behavior of inversion heights in a dry boundary layer over land. Stratus is shown to propagate both downward and upward during nocturnal cooling periods under the influence of the radiant/turbulent driving mechanism located in the cloud top. If the late afternoon inversion height is low enough, the stratus is predicted to reach the surface.

V. Organized Features within the Atmospheric Boundary Layer

In even quite chaotic turbulent flow, it has long been recognized that individual organized features may be discerned if the flow is inspected carefully enough. Leonardo da Vinci's sketches of flow in the hydraulic channels of his day clearly show this. When simulating the atmospheric boundary layer, we must decide when to seek to resolve particular features rather than to ensemble average over them. Particular features may be resolved, using a model of the type discussed in Chapter 2, by incorporating the boundary conditions for the feature into the boundary conditions for the mean variables.

The most ambitious calculations of this type have been Deardorff's (1972, 1974a and b) completely 3-D, unsteady calculations of neutral and unstable planetary boundary layers. He found little difference between the results of his second-order closure calculation, and that using a simpler eddy viscosity approach. This is consistent with the premise that he was able to use a sufficiently fine mesh size in his calculation so that the major contributions to the turbulent correlations were resolved as part of the mean flow calculation. The small scale motion was needed to dissipate turbulent energy, but the details of how this energy was dissipated at this small scale appeared relatively unimportant to the dynamics of the larger scale motion. Our purpose herein is not to look at the flow in this great detail, but rather to consider a few situations where organization of the large scale flow is particularly important.

All of the examples considered in detail in this chapter involve a two-dimensional symmetry, either planar or axisymmetric, of the large scale flow. The three-dimensional, smaller scale flow must be represented by the closure modeling. Thus we expect closure to be less critical to these flows than it is to the strictly one-dimensional simulations, but more critical than it is to a fully three-dimensional simulation. The particular features chosen to be discussed in detail reflect a personal bias. Other features which may be fruitfully simulated in this 2-D manner are the coastal, sea-breeze, circulation (Pielke, 1974b; Lewellen and Teske, 1976b); frontal dynamical interaction with the surface, topography induced features (see review by Hunt, 1980); and internal wave dynamics in stable regions of the boundary layer.

Some features are inherently three dimensional. These continue to present a real challenge to the turbulent transport modeler. Generally, further compromises must be made in modeling the turbulence in order to permit the added numerical complexity inherent in fully 3-D, unsteady calculations. Yamada, in his 3-D simulations of flow in the neighborhood of a cooling pond (1979), of flow in a complex mountain terrain (1980), and of lake breeze circulations around Lake Michigan (1979), has used the one-dimensional turbulent transport model given in Eqs. (2.3.29 and 2.3.30). Pielke (1974a) and Tapp and White (1976) all use O'Brien's (1970) eddy viscosity parameterization in their 3-D simulations of the sea breezes over south Florida.

The brief sampling of analyses of organized boundary-layer features presented within this chapter are not meant to imply that most such features are well understood. Quite the opposite is true. Even under conditions typical of a "horizontally homogeneous" fair weather boundary layer , Barnes, et al. (1980) found up to 20% of the "turbulent" fluxes to be transported by eddies of the order of 10 km wide. Much remains to be learned about such features.

5.1. Flow Over an Abrupt Change in Surface Conditions

The simplest type of feature is that which regularly occurs whenever there is an abrupt change in surface conditions. An internal boundary is induced with it's thickness growing downwind of the surface change. Calculations have been made by Rao, et al. (1974) and by Lewellen, et al. (1974) of both the transition from rough-to-smooth and smooth-to-rough surfaces. The results of both calculations are compared, in Figure 5.1.1, with the surface data of Bradley (1968), who recorded velocities and surface

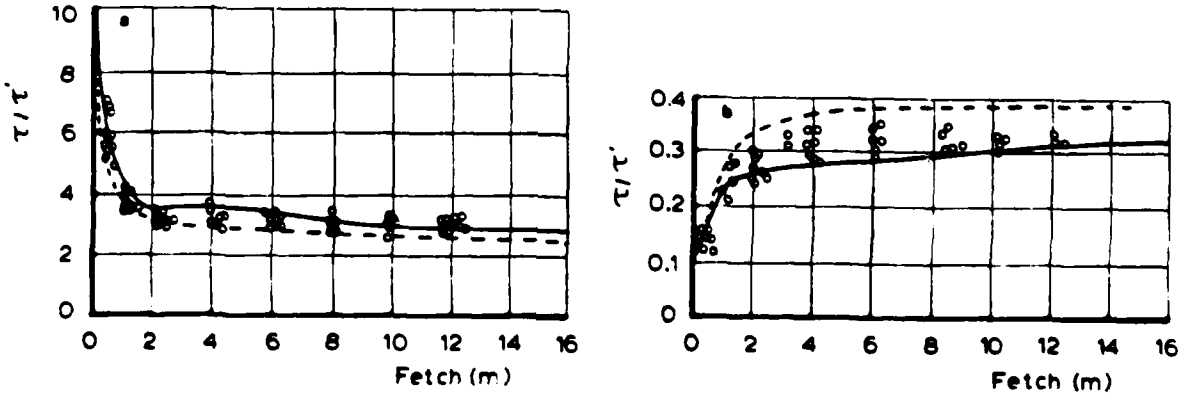

Figure 5.1.1 - Response of surface shear to step change in surface roughness. Lewellen (1977) (——); Rao, et al. (1974) (----). Data from Bradley (1968). (a) Smooth to rough $z_0' = 0.002$ cm, $z_0 = 0.25$ cm; (b) rough to smooth $z_0' = 0.25$ cm, $z_0 = 0.002$ cm.

shear stress at a little-used airfield in Australia. The calculations begin with the velocity and turbulence components in equilibrium for one value of aerodynamic roughness, z_o'. The surface boundary condition is changed to that appropriate for the new value of z_o at x = 0. When both runs are allowed to continue far downstream, the turbulence comes into equilibrium with the new value of z_o. Rao, et al. (1974) used the second-order closure model developed by Wyngaard and Cote (1974) which has somewhat different modeled terms than those given in Chapter II and used in the calculations by Lewellen, et al. (1974). Both calculations show reasonably good agreement with the observations. The major adjustment in surface shear stress is made within a few meters, but a distance of the order of a several tens of kilometers is required for the complete boundary layer to make its transition.

A similar sharp change in the boundary layer structure occurs when there is an abrupt change in surface temperature. This is often seen along shorelines where temperature differences between the land and water may easily exceed 10°C. This leads to what Lyons (1975) has termed a thermal internal boundary layer (TIBL). Relatively cold air flowing over a warmer surface leads to a growing layer of increased turbulence produced by buoyancy.

5.2 Longitudinal Roll Vortices

The type of large scale coherent structures which occur most often in the boundary layer are eddies which extend the full height of the mixed layer in the form of longitudinal roll vortices aligned close to the direction of the mean wind. An example of the clouds resulting from this motion are shown in Figure 5.2.1. When the boundary layer is treated as spatially homogeneous, the motion of these roll vortices must appear as part of the turbulence. To examine the relative contributions of the smaller scale random turbulence and the relatively organized large scale rolls, a two-dimensional calculation was performed in the (y,z) plane perpendicular to the axis of the rolls (Lewellen, et al. 1980). Periodic boundary conditions were applied so that the domain covers a wavelength λ in the y direction. The vertical domain extended from the surface (represented by an effective roughness z_o) to slightly above the capping inversion. The coordinate system permits the horizontal roll vortices to appear as part of the ensemble mean motion when calculating the unsteady flow in the unstable boundary layer.

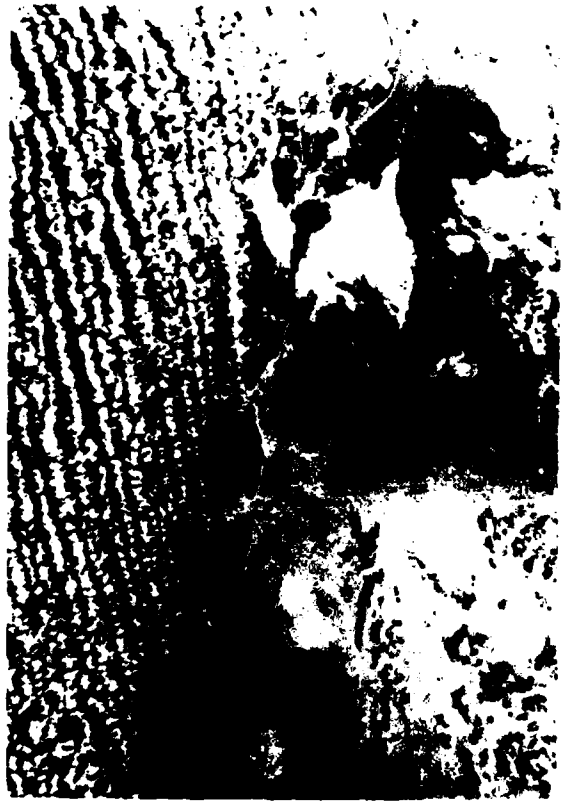

Figure 5.2.1 - Apollo photograph of Georgia Coast, 1700 Z from 125 miles high. From Brown (1974).

The numerical code partitions the energy between the mean background motion which is a function of the vertical coordinate only; the mean quasi-periodic, two-dimensional, roll vortex motion which is a function of z and y; and the more random turbulent motion which, although three-dimensional in character, is only a function of y and z in the mean. The energy in the organized roll motion varies with the ratio of the wavelength, λ, of the roll to the inversion height, z_i; the instability of the layer as measured by the ratio of the Monin-Obukhov length, L, to z_i; and the angle, α, between the roll axis and the geostrophic wind. Figure 5.2.2 illustrates the cross-sectional structure of the stream function of the roll motion for an angle of -10°, $\lambda/z_i = 3$ and $L/z_i \approx -0.1$ to approximate observations. Surface conditions are chosen appropriate for a sea surface at constant temperature. Results are scaled in terms of the characteristic velocity

$$w_* = \left(\frac{g}{T_0} \langle \overline{w\theta_v} \rangle z_i \right)^{1/3}$$

to minimize the influence of changes in $\overline{w\theta_v}$. (The angled bracket represents an average over y.) The geostrophic velocity is held at $U_g = 10$ m/s throughout the calculations.

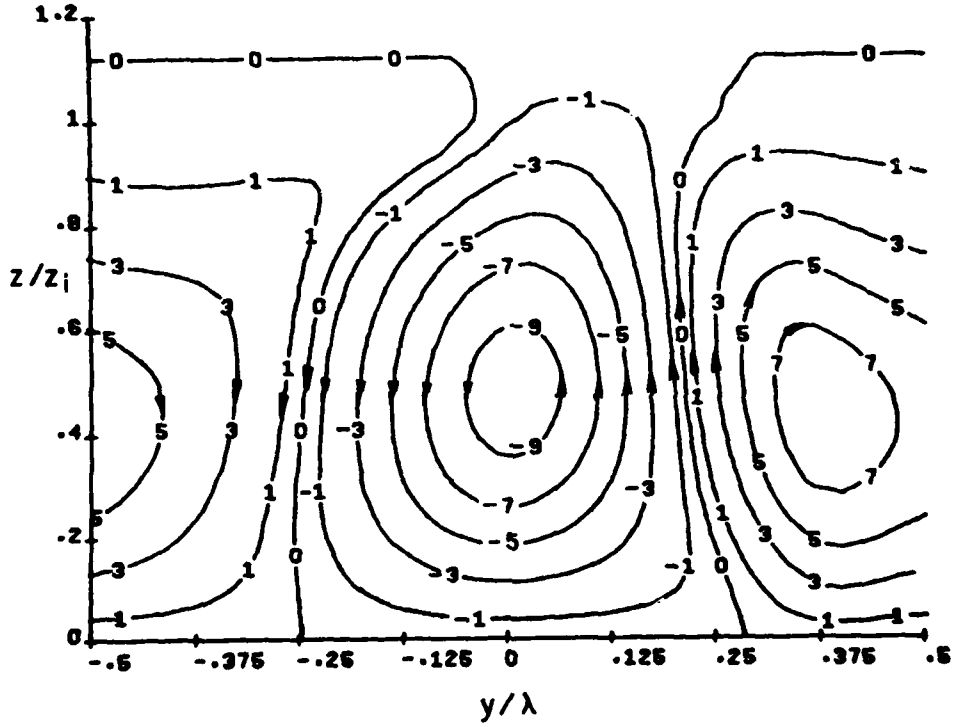

Figure 5.2.2 - Roll stream function contours for the example case of $\alpha = -10°$, $\lambda/z_i = 3$, $L/z_i = -0.1$. The profiles are normalized by a maximum value $\Delta v_{max}/w_* z_i = 0.287$ ($\Delta v = v - \langle v \rangle$), with ±9 denoting ±90% of maximum value; ±7, ±70%, etc. The arrows indicate flow direction. (Lewellen, et al., 1980).

The corresponding cross-sectional structure of the turbulent kinetic energy and the humidity are shown in Figures 5.2.3 and 5.2.4. The numerical results for the relative contributions of the mean roll motion and the roll modulated turbulence to the transport of momentum and heat compare reasonably (Teske and Lewellen, 1979) with the observations of LeMone (1976).

In Figures 5.2.3 and 5.2.4, the background levels have been removed; hence Δq^2 shows some regions of negative values. The updraft region shown in Figure 5.2.2 produces a band with a spread of about 0.25 λ which has greater than background C and q^2. The rest of the q^2 region is dominated by a much broader area of less than average values of Δq^2. Figure 5.2.4 shows a noticeable, almost jet-like character to ΔC. The heat flux is concentrated upward in the same region also, producing a temperature overshoot.

The vertical structure of the flux of a species such as humidity from the surface is shown in Figure 5.2.5. At the surface, the vertical transport is all carried by the small scale turbulence designated by $(\overline{wc})$, but at $z/z_i \approx 0.4$, approximately 2/3 of the vertical flux is contained in the mean roll motion designated by $\langle WC \rangle$. The heat flux structure is similar (Lewellen, et al. 1980) except for an undershoot in $\langle W\theta \rangle$ above $z/z_i \approx 0.75$ forced by the capping inversion.

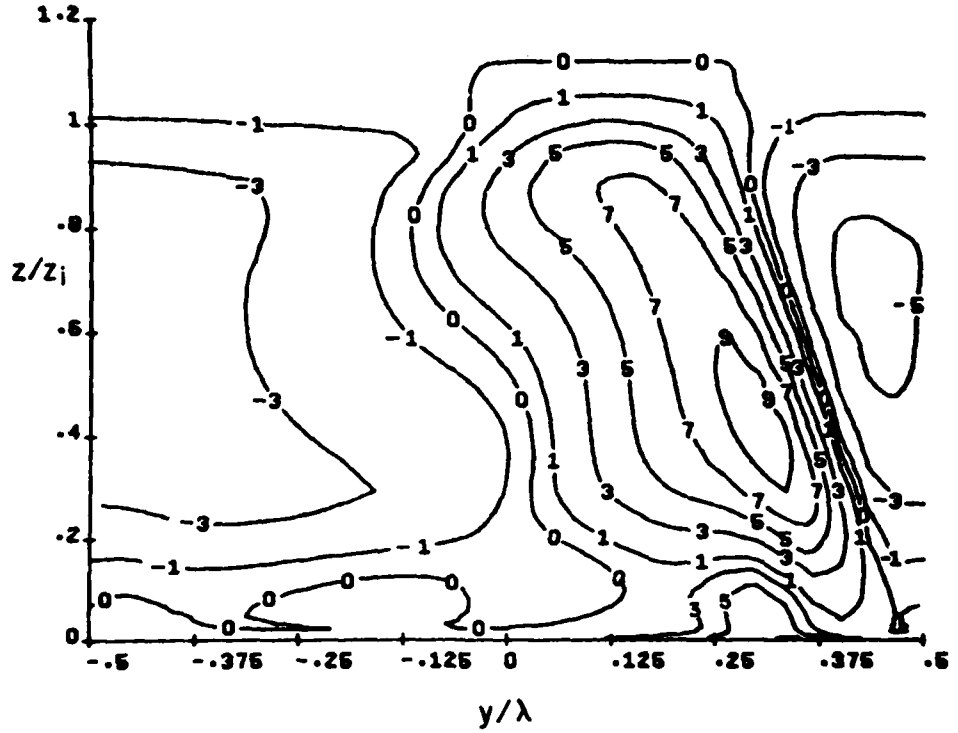

Figure 5.2.3 - Perturbation turbulence contours for the conditions given in Figure 5.2.2. Here $\Delta q^2_{max}/w_*^2 = 0.4$ is the normalizing maximum value.

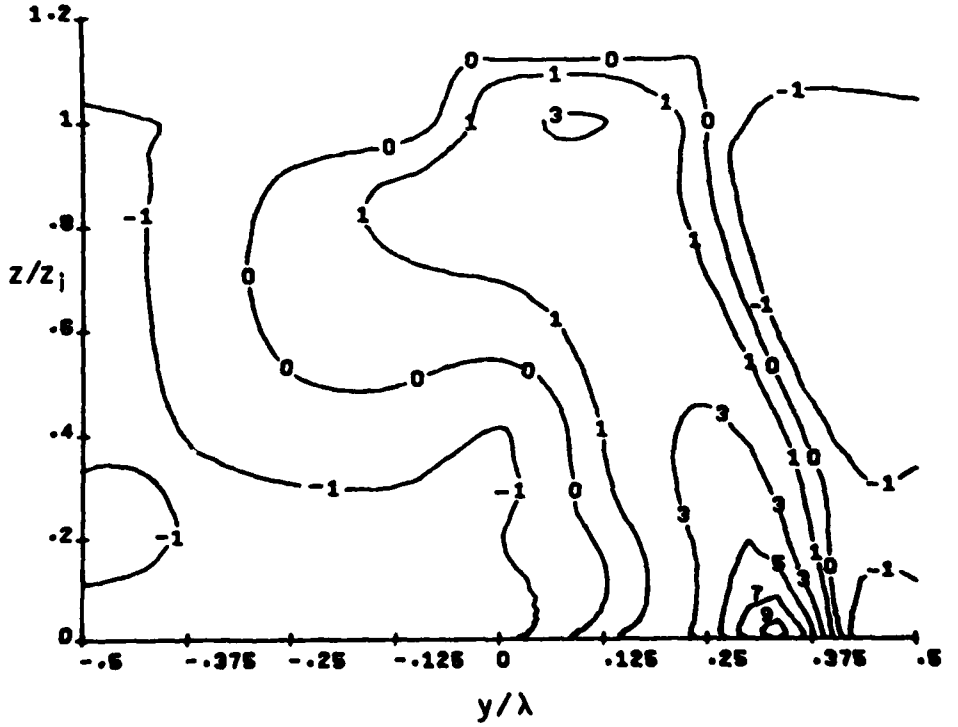

Figure 5.2.4 - Roll species contours for the conditions of Figure 5.2.2. The normalizing maximum value is $\Delta C_{max} w_*/\overline{cw_0} = 6.62$.

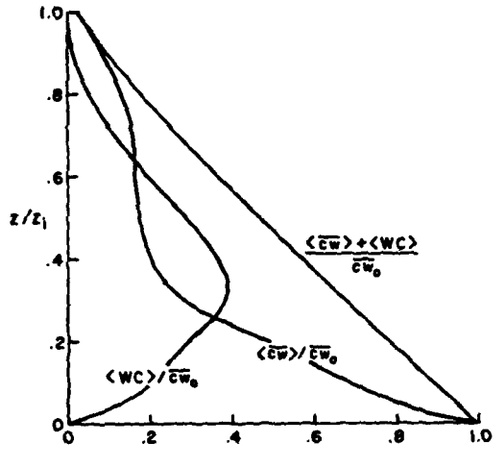

Figure 5.2.5 - Composite y-averaged variation of the vertical species flux in the rolls ⟨WC⟩ and the turbulence ⟨$\overline{wc}$⟩ for the conditions of Figure 5.2.2. Here $\overline{cw}_0$ is the species flux at z_0.

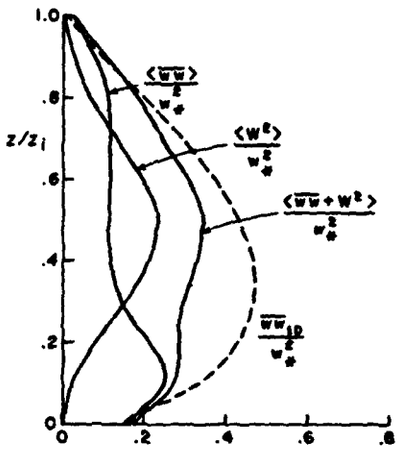

Figure 5.2.6 - Comparison between the *one-dimensional* and two-dimensional predictions for vertical velocity variance. For the two-dimensional calculation, the y-averaged, large scale roll contribution is denoted by ⟨W^2⟩ and the smaller scale turbulence by ⟨$\overline{ww}$⟩.

If the closure modeling were exact, the one-dimensional (*horizontally homogeneous*) analysis of this problem, which averages over the periodic large eddy roll structure and treats the roll energy as part of the turbulent kinetic energy, would yield the same answer as obtained by horizontally averaging over the two-dimensional result. Since the two-dimensional computation allows the dominant large eddy structure to be determined, the closure modeling should be less critical in this computation than it is in the analogous one-dimensional computation. In fact, a 2-D, large eddy model using eddy viscosity by Mason and Sykes (1980) shows many of the same features demonstrated here. For this phenomenon, which has a strong two-dimensional character, our model represents an intermediate step between depending completely on closure modeling and depending on sub-grid closure modeling. Thus, the two-dimensional result can be used to check strengths and weaknesses of the one-dimensional model.

The separate components of the velocity variance are shown in Figures 5.2.6 *through* 5.2.8. *There* is a reasonable comparison between the vertical variance predicted by the one-dimensional model and the spatial average of the two-dimensional results. But the other two components show significant differences.

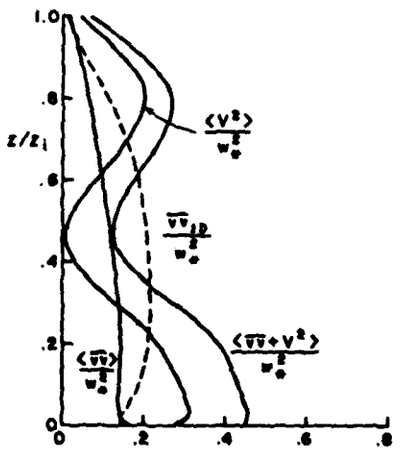

Figure 5.2.7 - Comparison between the one-dimensional and two-dimensional predictions for transverse velocity variance. For the two-dimensional calculation, the y-averaged, large scale roll contribution is denoted by ⟨V^2⟩ and the smaller scale turbulence by ⟨$\overline{vv}$⟩.

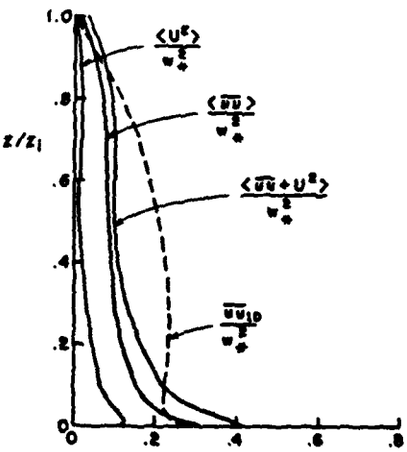

Figure 5.2.8 - Comparison between the one-dimensional and two-dimensional predictions for longitudinal velocity variance. For the two-dimensional calculation, the y-averaged, large scale roll contribution is denoted by ⟨U^2⟩ and the smaller scale turbulence by ⟨$\overline{uu}$⟩.

The analogous comparisons of the vertical momentum flux and the vertical heat flux are shown in Figures 5.2.9 and 5.2.10. In the middle of the mixed layer, a major portion of the turbulent transport is carried by the large roll structure. Both models predict a heat flux which is counter gradient over approximately one-half of the mixed layer depth. The two-dimensional model predicts a larger undershoot in the heat flux near the inversion. This undershoot in the heat flux is forced by the large eddies overshooting their thermal equilibrium position. The two-dimensional model can resolve this motion but the one-dimensional model must rely on the third-order modeled terms to correctly incorporate the results of these large eddies. The two-dimensional model is also able to account for more influence of the wave motion in the stable region than is represented in the one-dimensional model. This large difference in the two models is also apparent in Figure 5.2.11 which shows the temperature variance. By far, the largest contribution to temperature variance at the top of the mixed layer is the wave motions induced by the large rolls. However, even the small scale turbulent variance is approximately a factor of two larger than that predicted by the one-dimensional model at $z/z_i = 1$.

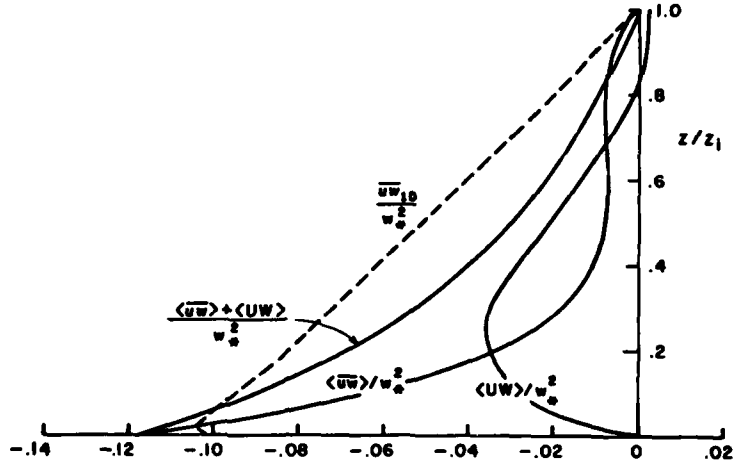

Figure 5.2.9 - Comparison between the one-dimensional and two-dimensional predictions for the vertical longitudinal momentum flux. The y-averaged roll contribution is denoted by <UW> and the turbulent transport by <uw>.

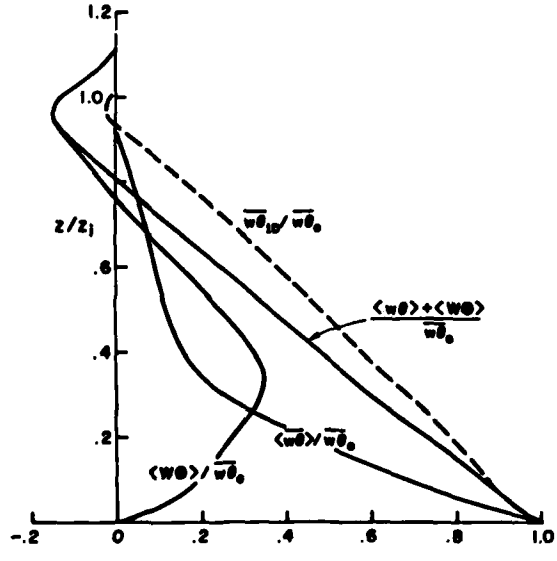

Figure 5.2.10 - Comparison between the one-dimensional and two-dimensional predictions for the vertical heat flux. The y-averaged roll contribution is denoted by <Wθ> and the turbulent transport by <wθ>.

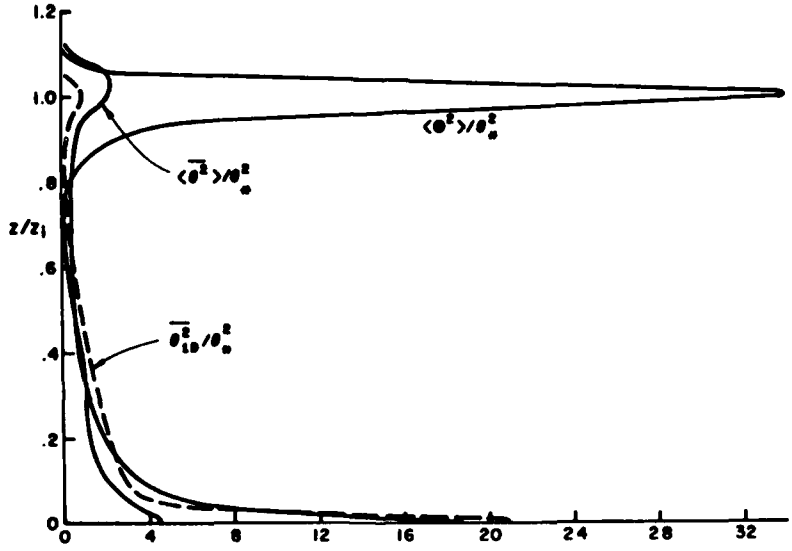

Figure 5.2.11 - Comparison between the one-dimensional and two-dimensional predictions for the temperature variance. The y-averaged roll contribution is denoted by $\langle\theta^4\rangle$ and the turbulent contribution by $\langle\theta^2\rangle$.

Figures 5.2.6 through 5.2.11 show that although the turbulent transport compares quite favorably for these two models, there is considerably more kinetic energy near the surface and near the inversion in the more correct two-dimensional model. The deficiencies of the one-dimensional model appear to reflect the difficulty of modeling with an anisotropic turbulent macroscale. It is clear from the two-dimensional simulation as it is from field observations, that at both the top and bottom of the domain, the characteristic horizontal scale of the turbulence is much larger than the characteristic vertical scale. It appears that the next step in improving the model calls for incorporating some structural shape in the scale representation, as discussed in Section 3.3.

The roll structure shown in Figure 5.2.2 should be expected to be a function of z_i/L. The exact dependence remains to be unraveled, but I would expect it to lead to some modification in the aspect ratio of the rolls and their alignment with respect to the mean wind. A better definition of this dependency can possibly permit satellite pictures of this commonly visible boundary layer feature to yield useful information about the concurrent boundary-layer structure. Figure 5.2.12 shows the winter time obervations of roll clouds over the Bering Sea. As reported by Walter (1980), such pictures may be analyzed to obtain quantitative information about the boundary layer thickness and its rate of growth.

Figure 5.2.12 - (a) NOAA-4 satellite photograph of the Bering Sea showing the ice edge and roll clouds (2127 GMT 19 March 1975). Walter (1980).

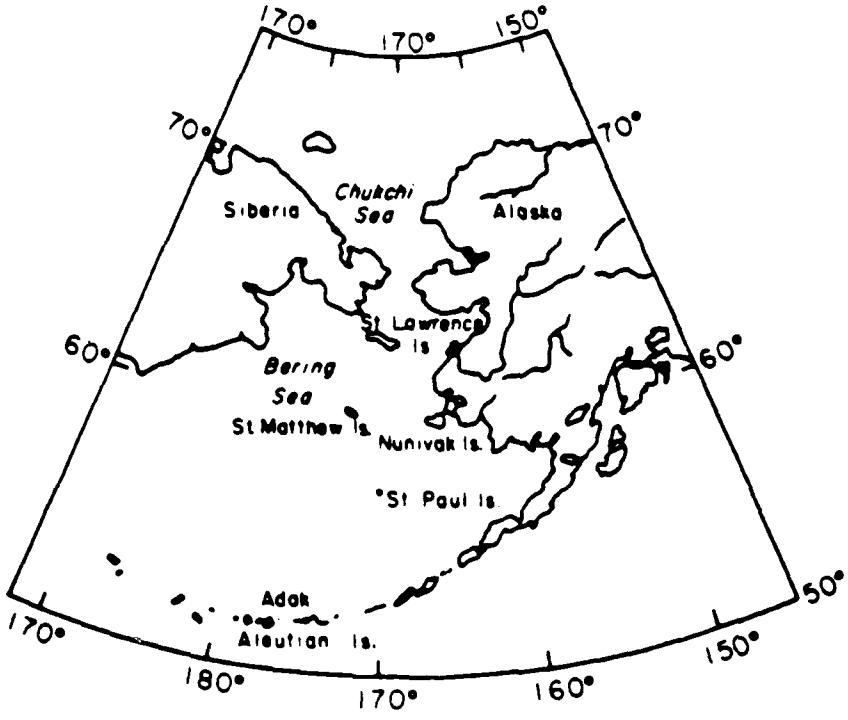

(b) Map of the Bering Sea area.

5.3. The Thunderstorm Downdraft and Associated Gust Front

If convection is much stronger than advection locally, then the dominant eddy may appear as a combination of ring vortices about the same vertical axis. Natural cumulus clouds and plumes from large heat sources are examples of such vertical plumes driven by buoyancy. We consider here an example of such an axisymmetric eddy driven by negative buoyancy. This downdraft leads to horizontal divergence in the boundary layer. The positively buoyant plume leads to horizontal convergence, which will amplify any ambient vertical vorticity. Thus strong upward plumes may be expected to strongly interact with the vertical vorticity component. The extreme example of this type of flow, the tornado, will be considered in Section 5.4.

The gust front caused by the cold outflow emanating from a thunderstorm has been modeled by Mitchell (1975) using a constant eddy viscosity model and by Teske and Lewellen (1977) using an axisymmetric implementation of the second-order turbulence model given in Chapter 2. The simulated flowfield is illustrated in Figure 5.3.1. The outflow from the thunderstorm is idealized as a cold jet of temperature $\theta(r)$ impinging normal to the ground, released at a height z_{max} with vertical velocity $W(r)$. The temperature defect below the ambient temperature is caused by evaporation of falling rain by relatively dry air at some altitude $z > z_{max}$.

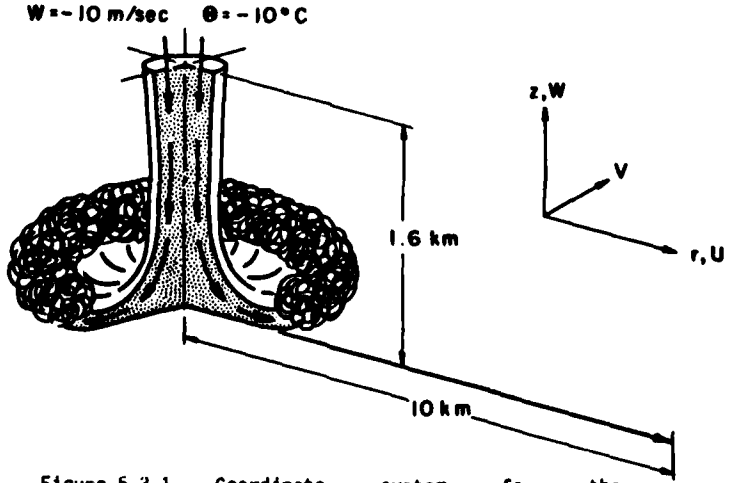

Figure 5.3.1 - Coordinate system for the axisymmetrical thunderstorm downdraft interacting with the surface to form a gust front.

The primary variables in this simulation are the temperature defect (below ambient) of the jet, its diameter, and the height at which it is released. The larger scale updraft within which the downdraft is embedded plays a role in retarding the late-time gust front within the computational domain, but should not be a critical factor as long as the inflow velocity is smaller than the resulting internal simulated velocities. The other critical parameters are the surface temperature, the surface roughness, and the stability of the ambient atmosphere.

One way to follow the structure of the developing gust is to observe the movement of a temperature isopleth, in this case θ = -2°C, as shown in Figure 5.3.2, for the simulation sketched in Figure 5.3.1. At t = 0, the initial linear profile is shown, but by t = 200 sec, the structure has developed into a moving front. At t = 340 sec, the front has torn away from the downdraft region. At later times, the strength of the gust decreases as the effect of the area change becomes more important. However, the height of the gust appears to grow slowly, so that by t = 1000 sec, the θ = -2°C line reaches nearly 1 Km in altitude at a distance of nearly 8 Km from the source centerline. The front is still quite strong at this point, and is moving outward at approximately 2.6 m/sec with maximum horizontal winds within the outflow of approximately 25 m/sec.

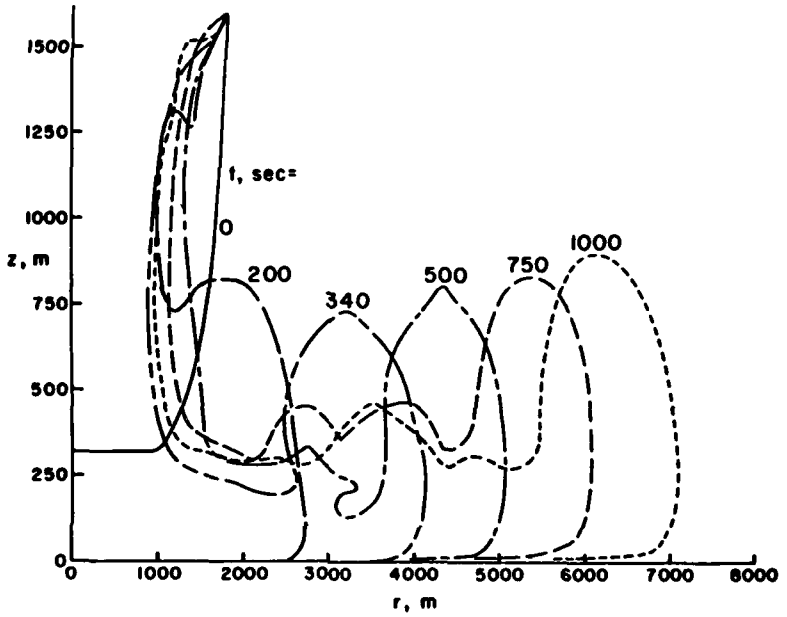

Figure 5.3.2 - The evaluation of a simulated gust front as shown by isopleths of constant temperature defect (θ = -2°C) at several times after initialization. (Teske and Lewellen, 1977).

When this numerically simulated front is visualized in terms of the temperature defect intensity, the leading edge appears as shown in Figure 5.3.3. There is a very strong qualitative similarity between this

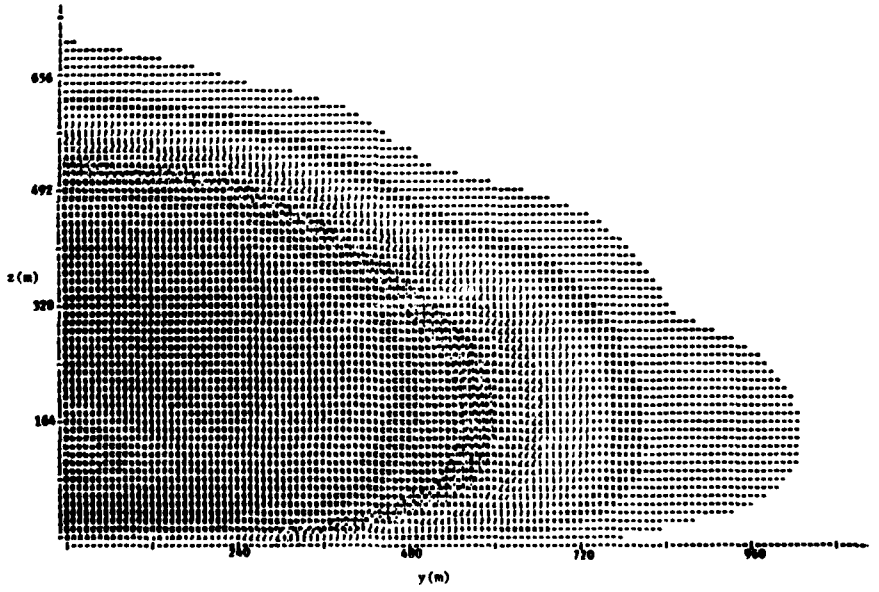

Figure 5.3.3 - The leading edge of the gust front shown in Figure 5.3.2 when visualized in terms of temperature defect intensity.

picture and the gust front as visualized by dust in Figure 5.3.4 (also see Turner, 1973). The quantitative predictions of maximum mean velocity, velocity shear and variance also appear consistent with available observations. As part of a study to evaluate hazardous conditions for aircraft operations, a sensitivity analysis has been performed on the gust front as a function of five different dimensionless physical parameters (Teske and Lewellen, 1978). We will return to this in Section 6.2.

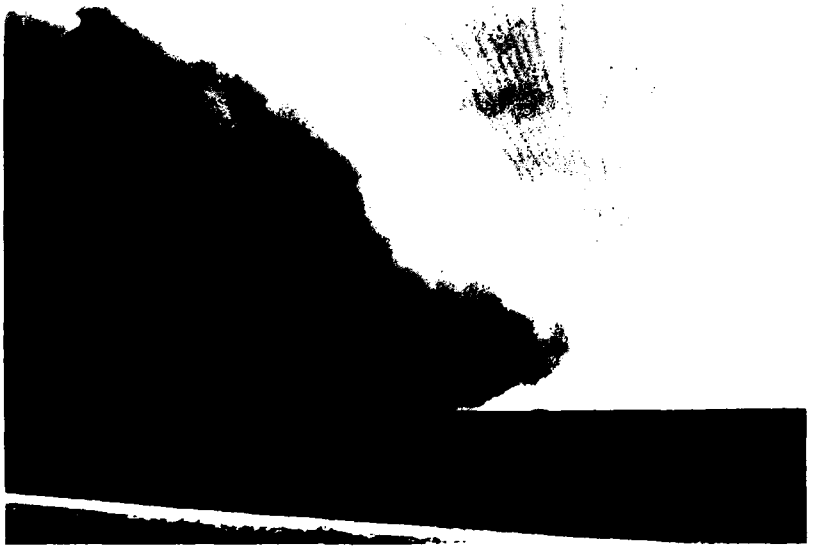

Figure 5.3.4 - The leading edge of a thunderstorm gust front as marked by dust. (Photo by Andrew Watson, Miami, Florida, 1975).

5.4. Tornado Boundary Layer

The horizontal convergence induced by positively buoyant plumes or updrafts generally leads to some amplification of ambient vorticity. At the barely discernable level this leads to the small whirls in the steam fog rising from a warm water pond on a cold morning. The common dust devil provides a somewhat larger, and more impressive demonstration of this phenomenon. Generally larger and still more impressive is the water spout. Finally, the most awesome example of this type of flow is the mature tornado.

Recent reviews of tornado dynamics have been given by Davies-Jones (1980) and Lewellen and Sheng (1980b). Although the precise conditions necessary for the birth of a tornado are still subject to some speculation, the two essential ingredients are: (1) an ambient conditional instability generated by abundant moisture in the boundary layer capped by a dry air mass in the mid troposphere; and (2) ambient vertical vorticity in the form of a mesocyclone which may be generated by the amplification of the vorticity associated with the earth's rotation. Numerical simulations (e.g., Klemp and Wilhelmson, 1978) and dual Doppler radar observations (e.g., Brandes, 1977) also demonstrate a critical role for vertical shear of the ambient horizontal winds in organizing the most severe storms.

The ambient conditional instability is released through condensational heating in the uplifting of the moist surface layer air and evaporative cooling in the sinking of the dry mid-tropospheric air. The vertical shear in the horizontal wind allows both the updraft and downdraft to become well developed before they interfere with each other. Both the Doppler observations and the numerical simulations also suggest that the tilting of the ambient horizontal vorticity is as important in the generation of vorticity as the convergence term.

A vertical jet or plume issuing into a horizontal crossflow generates a pair of vortices with equal magnitude and opposite sign circulation. The magnitude of the vorticity generated in this manner should be of the order of the product of the distance between the vortex pair and the relative velocity between the plume and the crossflow divided by the square of the radius of the region of concentrated vorticity. Thus a 10 m/sec relative velocity, a 10 Km distance between the pair, and a 3 Km region of concentrated vorticity lead to a value of vorticity of the same order as that found in the mesocyclone ($\sim 10^{-2}\text{sec}^{-1}$). As long as the vorticity generated by this tilting process is of the same order as that resulting from the convergence of the ambient vorticity due to the earth's rotation, the cyclonic member of the vortex pair is essentially doubled while the anticyclonic member is nearly eliminated. The remaining single mesocyclone tends to bear to the right of the ambient wind direction.

A fully 3-D model is required to simulate the total storm, including all the important vorticity generating terms. However, a restricted region about the central core of the tornado may appropriately be modeled as axisymmetric, with flow into and out of the boundaries of the computational domain. An axisymmetric version of the basic turbulent transport model presented in Chapter 2 has been used to simulate this tornado core boundary layer (Lewellen and Teske, 1977). Figures 5.4.1 through 5.4.3 show the results of a computer simulation chosen to show a resemblance to the 1974 Xenia, Ohio tornado. For this simulation, the domain's outer radius and top are both placed at 400 m. The surface roughness is taken to be large (0.4 m) to correspond to a relatively urban area. All components of the velocity are specified at the outer radius inflow boundary and relatively free zero slope conditions are applied at the top of the domain.

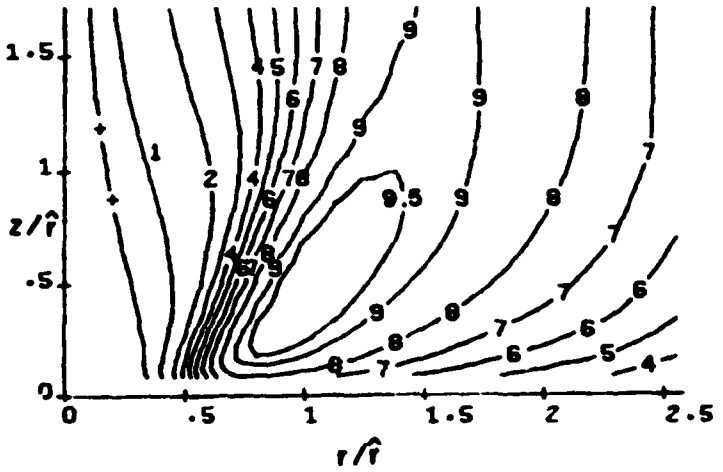

Figure 5.4.1 - Mean tangential velocity contours as predicted by an axisymmetric tornado model. Contours labeled in tenths of maximum V, and radial and vertical coordinates normalized by the radius at which V_{max} occurs.

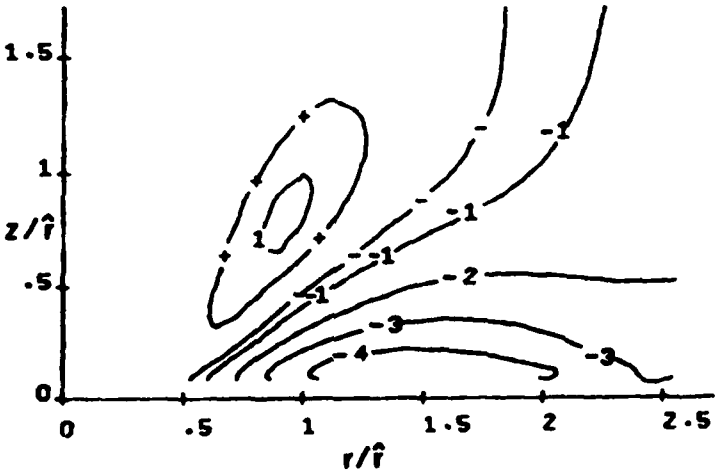

Figure 5.4.2 - Mean radial velocity contours as predicted by an axisymmetric tornado model. Contours labeled in tenths of maximum V, and radial and vertical coordinates normalized by the radius at which V_{max} occurs.

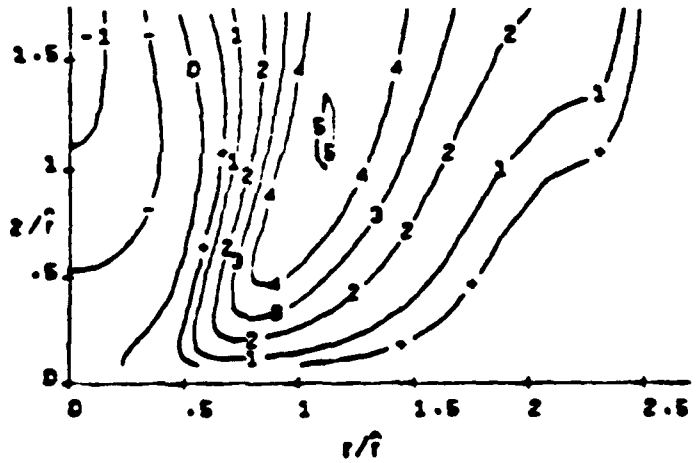

Figure 5.4.3 - Mean vertical velocity isopleths for the simulated tornado. Contour notation is the same as in Figure 5.4.1, except normalization is by 0.510 V_{max}.

The mean tangential, radial, and vertical velocity fields given in Figures 5.4.1 through 5.4.3 are normalized by the maximum tangential velocity which occurs at r ≈ 180 m, z ≈ 100 m. The absolute value of the maximum velocity depends strongly on the relatively uncertain inflow and outflow boundary conditions. However, when the model result is scaled to give a V_{max} in agreement with the photogrammetric analyses of Umenhofer and Fujita (1977), the vertical distribution of tangential velocity at r = 180 m is given in Figure 5.4.4. Although the wind scale is set by the observations, the vertical distribution and the fluctuations about the mean are predicted by the model. Figure 5.4.5 shows a similar representation of the vertical velocity. With the velocity scale set in the previous figure there is no arbitrariness in the predictions of Figure 5.4.5.

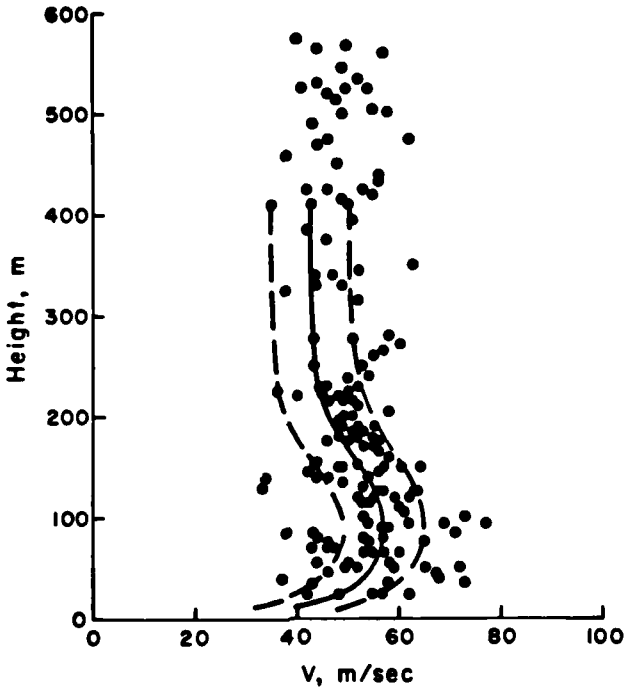

Figure 5.4.4 - Comparison between the swirl velocity profile predicted by A.R.A.P.'s model at r = 180 m (Lewellen and Teske, 1977) and the observations of Umenhofer and Fujita (1977). Dashed line represents the predicted r.m.s. fluctuation about the mean solid curve.

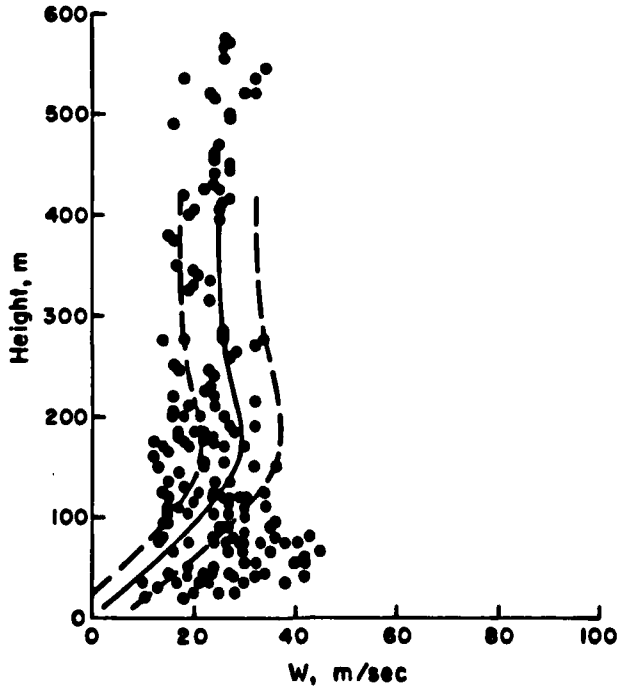

Figure 5.4.5 - Vertical velocity distribution at the same radius and for the same conditions as Figure 5.4.4.

Model sensitivity analyses show the flowfield to be most dependent on the ambient vertical vorticity and horizontal convergence occurring in the parent thunderstorm, and on the surface roughness. When dual Doppler observations (Brandes, 1979) are used to impose the boundary values of vorticity and convergence at 1 Km radius and 1 Km height, the model is consistent with the estimate that velocities within a tornado will very rarely, if ever, exceed 125 m/sec (Lewellen and Sheng, 1980).

A dominant feature of all of the flowfields computed (Lewellen, et al., 1979; and Lewellen and Sheng, 1979, 1980) is that the maximum winds occur at quite low altitudes. The surface layer plays the rather paradoxical role of increasing the velocity in the neighborhood of the ground at small radii, before actually reducing the velocity to zero at the surface. The strong radial inflow in the surface layer permits the streamlines to penetrate to smaller radii here than at higher altitudes. Even without total conservation of angular momentum, this permits higher swirling velocities to develop. The simulation also predicts that the r.m.s. average of the velocity fluctuations reaches values as high as $0.3\ V_{max}$. The time scale of the eddies is such that the average strong eddy should have a life span somewhat less than one period of revolution for the tornado. This large magnitude of the fluctuating velocities indicates that they should be considered in setting design criteria. The maximum damage will occur in swaths where the instantaneous fluctuating velocities add to the local mean velocity. Such damage patterns are often observed (Fujita, et al., 1976).

VI. Example Applications of Particular Interest

6.1. Dispersal of Industrial Plumes

As noted in the introduction, one of the vital services that the atmosphere provides is the dispersal of waste products from the machines man has invented to serve himself. The capacity of the low-level atmosphere to perform this function varies strongly with meteorological and specific site conditions. A large number of semi-empirical models have been developed to predict this capacity as part of the process of deciding what facilities may be built where. The status of the most standard of these models have been reviewed by Turner (1980). Our purpose herein is not to review the excellent expositions given on atmospheric diffusion by Pasquill (1974), Csanady (1973), and Dobbins (1979), but rather to briefly discuss the subject in the context of turbulence modeling.

As must be evident from the preceeding chapters, the motion of the lower atmosphere has a rich variety of modes for transporting and intermixing species. Practical methods of predicting dispersal necessarily aim at greatly simplifying these mixing processes rather than attempt to solve for the motion in minute detail. In attempting to describe an effluent plume of a nonreacting conserved species, the most important features are the mean wind which determines where the plume will go, and the rate of spread of the plume in the plane perpendicular to its mean trajectory. The spread of the plume may be measured by

$$\sigma_r^2 = \frac{\int_{-\infty}^{\infty} Cr^2\,dA}{\int_{-\infty}^{\infty} C\,dA} = \frac{\langle Cr^2\rangle}{\langle C\rangle} \tag{6.1.1}$$

where the integrals are carried out over the plane perpendicular to the mean trajectory of the plume. An equation for the rate of spread may be obtained by multiplying Eq. (2.1.9) by r^2 and integrating, i.e.,

$$\frac{D\sigma_r^2}{Dt} = \frac{1}{\langle C\rangle}\frac{D\langle Cr^2\rangle}{Dt} - \frac{\sigma_r^2}{\langle C\rangle}\frac{D\langle C\rangle}{Dt} \tag{6.1.2}$$

and thus

$$\frac{D\sigma_r^2}{Dt} = -\frac{1}{\langle C\rangle}\left\langle r^2\left(\frac{\partial\overline{wc}}{\partial z}+\frac{\partial\overline{vc}}{\partial y}\right)\right\rangle + \frac{\sigma_r^2}{\langle C\rangle}\left\langle\frac{\partial\overline{wc}}{\partial z}+\frac{\partial\overline{vc}}{\partial y}\right\rangle \tag{6.1.3}$$

When the flux goes to zero on all the boundaries of the region, this last equation reduces to

$$\frac{D\sigma_r^2}{Dt} = \frac{2\langle x_i\overline{u_i c}\rangle}{\langle C\rangle} \tag{6.1.4}$$

From Eq. (2.3.21)

$$\frac{D\langle x_i\overline{u_i c}\rangle}{Dt} = \left\langle -\overline{u_i u_j}\,x_i\frac{\partial C}{\partial x_j} - \overline{u_j c}\,x_i\frac{\partial U_i}{\partial x_j} + g_i x_i\frac{\overline{c\theta}}{\theta_o} - \frac{Aq}{\Lambda}x_i\overline{u_i c}\right\rangle \tag{6.1.5}$$

and when $\langle x_i\overline{u_i c}\rangle$ is eliminated between Eqs. (6.1.4 and 6.1.5) a second-order differential equation for σ_r^2 is obtained

$$\langle C\rangle\frac{D^2\sigma_r^2}{Dt^2} = \left\langle -\overline{u_i u_j}\,x_i\frac{\partial C}{\partial x_j} - \overline{u_j c}\,x_i\frac{\partial U_i}{\partial x_j} + g_i x_i\frac{\overline{c\theta}}{\theta_o}\right\rangle - \frac{\langle(Aq/\Lambda)\,x_i\overline{u_i c}\rangle}{\langle x_i\overline{u_i c}\rangle}\frac{\langle C\rangle}{2}\frac{D\sigma_r^2}{Dt} \tag{6.1.6}$$

It is instructive to look at Eq. (6.1.6) under different limiting conditions. First consider the simplest limiting condition when the mean wind and turbulence quantities are homogeneous, and the gravitational term is negligible. In this limit

$$\frac{D^2\sigma_r^2}{Dt^2} = -\frac{2\overline{u_i u_j}}{\langle C\rangle}\left\langle x_i\frac{\partial C}{\partial x_j}\right\rangle - \frac{Aq}{\Lambda}\frac{D\sigma_r^2}{Dt} \tag{6.1.7}$$

which is satisfied by the expression

$$\sigma_f^2 = 2 \frac{\Lambda}{Aq} \overline{u_i u_i} t \tag{6.1.8}$$

since

$$\left\langle x_i \frac{\partial C}{\partial x_j} \right\rangle = - \delta_{ij} \langle C \rangle \tag{6.1.9}$$

Equation (6.1.8) corresponds to the classic constant diffusivity solution with $K = (4/3)\Lambda q$ and the plume spreading as $t^{1/2}$.

The initial time behavior of dispersion from a point source does not generally agree with that given by Eq. (6.1.8) even when the ambient atmospheric turbulence is stationary and homogeneous. Deardorff (1978) noted that there is an explicit dependence of Λ/q on time after release whether closure is made at first, second, or third order. In order for the q and Λ in the last term in Eq. (6.1.5) to be the same characteristic velocity and length scale as utilized for the ambient atmospheric turbulence, it is necessary for the plume spread to be larger than the ambient atmospheric turbulent length scale. This is generally not the case in the initial stages of a release. When the plume spread is less than the length scale of the most energetic turbulent eddies, then both the velocity and length scale of the plume may be significantly smaller than the comparison scales for the turbulent velocity field. Lewellen and Teske's (1976) approach to this difficulty was to take the plume turbulent scale proportional to the spread of the species plume

$$\Lambda_p = d\sigma \tag{6.1.10}$$

subject to the constraint

$$\Lambda_p \leq \Lambda_t \tag{6.1.11}$$

The proportionality factor d is a model input coefficient of the order of 1. To set the plume velocity scale q_p, they assumed that most of the interval between Λ_t and Λ_p would fall within the inertial subrange of the turbulent kinetic energy spectrum so that the rate of energy dissipation is constant as the energy cascades from the larger eddies to the smaller. From Eq. (2.3.5) energy dissipation is modeled as

$$\varepsilon \sim \frac{q^3}{\Lambda} \tag{6.1.12}$$

so that it is appropriate to take

$$q_p = q_t \left(\frac{\Lambda_p}{\Lambda_t} \right)^{1/3} \tag{6.1.13}$$

Equation (6.1.7) can then be written as

$$\frac{D^2 \sigma_f^2}{Dt^2} = 2\overline{u_i u_i} - \frac{A q_t}{\Lambda_p} \left(\frac{\Lambda_p}{\Lambda_t} \right)^{1/3} \frac{D\sigma_f^2}{Dt} \tag{6.1.14}$$

The late-time plume is appropriately described by Eq. (6.1.8), but in the initial phase when $\Lambda_p/\Lambda_t \ll 1$, the last term in Eq. (6.1.14) can be neglected and

$$\sigma_f^2 = \overline{u_i u_i} t^2 \tag{6.1.15}$$

This corresponds to the early time behavior predicted by statistical theory (Pasquill, 1974). Thus Eq. (6.1.7) provides a smooth transition from hyperbolic, wave-like dispersion of the plume when the plume spread is very small compared to the turbulent scale, to simple parabolic diffusion when the plume is large enough to contain the motion of the most energetic eddies.

The influence of buoyancy enters dispersion in two ways. First it has a strong effect on the turbulent velocity components. But as seen in Eq. (6.1.6), it also has a separate effect depending upon the covariance between the temperature and the species concentration.

To exhibit the influence of the buoyancy term more clearly, let us consider dispersion in the free convection layer in the absence of any mean velocity. Then the equation for the vertical flux of any species Eq. (2.3.4) may be written as

$$\frac{\partial}{\partial t}\overline{wc} = -\overline{ww}\frac{\partial C}{\partial z} + \frac{g}{\theta_0}\overline{c\theta} + \nu_c\frac{\partial}{\partial z}\left(q_p \Lambda_p \frac{\partial \overline{wc}}{\partial z}\right) - \frac{Aq_p}{\Lambda_p}\overline{wc} \tag{6.1.16}$$

In the absence of significant diffusion contributions from the third term on the r.h.s. of Eq. (6.1.16), a zero occurring in $\overline{wc}$ in coincidence with a zero in $\partial C/\partial z$ cannot be maintained unless the buoyancy term is also negligible. Conversely, it is possible for a vertical gradient in mean concentration to be maintained in response to the buoyancy term even in the absence of any vertical species flux. If the covariance of species and temperature is positive then Eq. (6.1.16) shows that a positive $\partial C/\partial z$ can be maintained while a negative covariance would lead to a negative $\partial C/\partial z$. A pulsed surface release into the free convection layer should yield a positive $\overline{c\theta}$ and consequently a positive $\partial C/\partial z$ in the immediate vicinity of a nonabsorbing surface. This leads to the position of the maximum mean concentration rising from the surface, as observed in Figure 6.1.1 experimentally by Deardorff and Willis (1974), and in Figure 6.1.2 as numerically calculated by Lewellen and Teske (1976). Conversely, a pulsed release near the top of the convectively mixed layer will yield at least a temporary negative $\overline{c\theta}$ and the position of the maximum concentration will tend to fall. Such a behavior could not be predicted by a two-equation turbulence model as long as

$$\overline{wc} \sim q\Lambda\frac{\partial C}{\partial z} \tag{6.1.17}$$

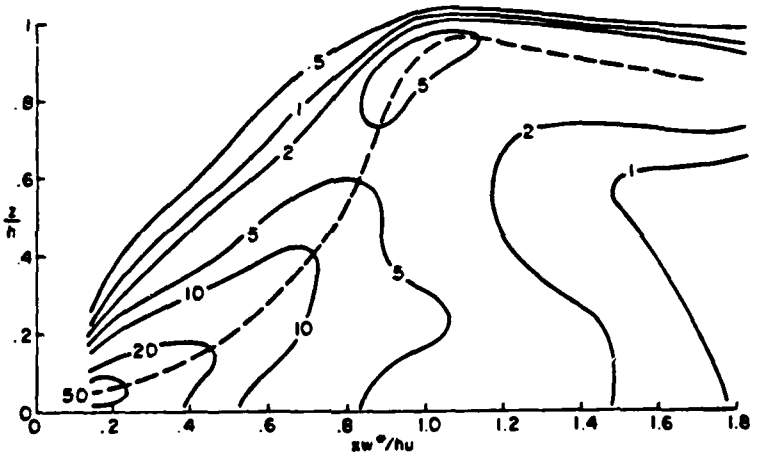

Figure 6.1.1 - Centerline concentration isopleths downwind of a continuous point-source release into a free convective layer; the results of Experiment A of Deardorff and Willis (1974).

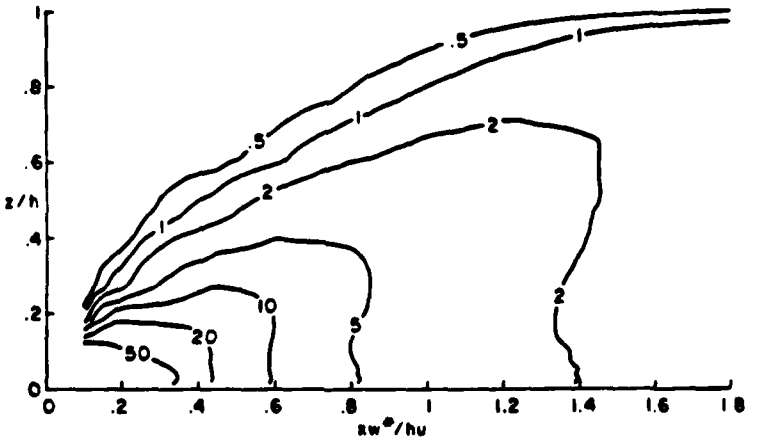

Figure 6.1.2 - Ensemble average of the centerline concentration isopleths downwind of a continuous point-source release into a free convective layer, as calculated by Lewellen and Teske (1976).

The popular Gaussian plume models described by Turner (1980) depend upon an empirical solution to Eq. (6.1.6). The spread σ is generally tabulated as a varying power-law of t (or x) for five different stability classes. Some of the better methods provide for allowing at least the horizontal variance to be directly measured at the site. Equation (6.1.6) appears to potentially provide the basis for using turbulence data measured at the specific site of a release for predicting the dispersal of that plume downwind of the site.

Sample second-order closure calculations of dispersion within the atmospheric boundary layer have been made by Lewellen and Teske (1975, 1976a and b), Yamada (1979a), and Teske, et al. (1978), but no rigorous comparisons with data have been made. Comparisons between calculations and observations of real field data are compounded by the fact that the model provides a simulation of the ensemble average plume while the field observation provides one specific realization from a number of different plumes which might be members of the simulated ensemble. These two should only be expected to coincide if (1) the meteorology is sufficiently steady for the turbulence to be stationary, and (2) the time over which the plume is averaged is long compared with the characteristic time of the large turbulent eddies. Such a long time average over a stationary plume should approximate the ensemble average of a number of individual plumes, each of which satisfy the same initial mean values. This combination provides a stringent test for any data set. As seen in the earlier chapters, the first condition severely limits the upper bound on the observation time, while the second pushes up the lower bound on the observation time.

As an example, consider the turbulence time scales likely to occur under unstable afternoon conditions. If the mixed layer height is of the order of 1 km, and w_* is of the order of 1 m/sec, then the time period for the rotation of such an eddy will be of the order of 1 hr. A time average of three hours or more would be required to provide the equivalent of an ensemble average. Samples averaged over times of one hour or less should be expected to show considerable variation from the ensemble mean value. Some indication of this difference can be obtained by calculating the plume concentration variances from Eq. (2.3.22)

$$\frac{\partial \overline{c^2}}{\partial t} + U_j \frac{\partial \overline{c^2}}{\partial x_j} = - 2\overline{u_j c} \frac{\partial C}{\partial x_j} + v_c \frac{\partial}{\partial x_j}\left(q\Lambda \frac{\partial \overline{c^2}}{\partial x_j}\right) - \frac{2bsq\overline{c^2}}{\Lambda_c} \qquad (2.3.22)$$

Numerous efforts, currently underway, to evaluate the accuracy of existing dispersion models (e.g., Hilst, 1978; Hilyer, et al. 1979; Ruff, et al. 1979; Londergan, 1980; Fox, 1981; and Pepper, 1981) may lead to the incorporation of some type of variance estimates in a new generation of dispersion models.

6.2. Wind Shear Around Airports

Wind shear and turbulence, particularly at the lower altitudes, has been identified as, at least, a contributing factor to a number of different aircraft accidents occuring during either takeoff or landing. Flowfield models such as those discussed in the preceeding five chapters are useful in evaluating the potential hazard presented by wind shear and turbulence under different conditions. A second-order closure model of the atmospheric boundary layer has been used to define the bounds on low-level wind shear under different conditions (Lewellen and Williamson, 1976), and to investigate the conditions existing at the time of a number of accidents (Williamson, et al. (1977).

Even within a one-dimensional approximation there are a rich assortment of possible wind and turbulence profiles. A rough summary of the turbulence intensity for different conditions is shown in Figure 6.2.1. Refer to Table 6.2.1 for the key to the different conditions. The turbulence is normalized by the maximum wind velocity between the ground and 1 km and plotted as a function of stability. As indicated in Chapter 3, it is not possible to reduce the detailed influences of stability to a single parameter. But for purposes of indicating only the rough dependence of stability, we have chosen a single parameter which does partially combine the influence of the surface heat flux, which controls stability in the surface layer, and the influence of the upper-level potential temperature gradient, which influences the elevation of the inversion layer which caps the boundary layer. This parameter is a bulk Richardson number based on the velocity and potential temperature differences between the surface and 1 km. The hysteresis loops presented for the different periodic cycles considered indicate the type of scatter to be expected in attempting to predict the fluctuations in this manner. As the bulk Richardson number approaches $-\infty$, corresponding to free convection, the normalized q will approach ∞. On the stable side, increasing $Ri_{(1000)}$ tends to decrease the normalized q whether the increase in stability is caused by increased surface cooling or a decrease in the upper-level inversion height.

A similar rough summary of the maximum wind shear occurring at or above 10 m altitude in the boundary layer is given in Figure 6.2.2. There is a fairly consistent trend of increasing shear with increasing stability, although there is a relatively strong influence of thermal wind which tends to mask this trend to some extent. The normalization of q by the maximum velocity within the layer tends to roughly compensate for the thermal wind influence in Figure 6.2.1. Of course, the wind shear in a profile at a given time cannot be characterized by a single number. The actual changes in airspeed which an aircraft will encounter, will also depend on the vertical depth over which this large shear exists. This must be determined by looking at the detailed profiles. Figure 6.2.2 does indicate the rough rule of thumb that as either horizontal temperature gradients increase or vertical, stable, temperature gradients increase, problems with wind shear may be expected to increase.

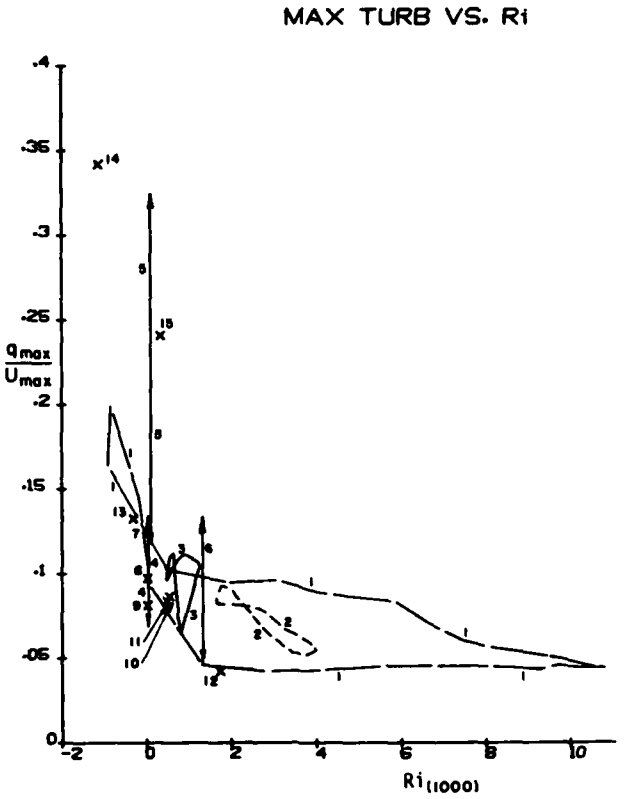

Figure 6.2.1 - Summary plot of normalized total velocity fluctuation as a function of the bulk Richardson number between the surface and 1 km altitude. Numbers refer to Table 6.2.1.

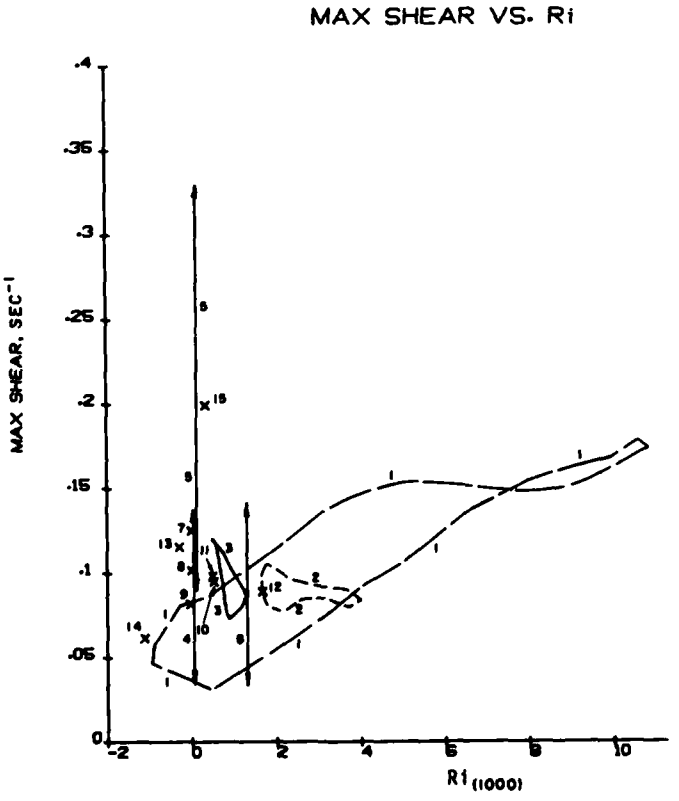

Figure 6.2.2 - Summary plot of maximum wind shear at or above 10 m altitude as a function of the bulk Richardson number between the surface and 1 km altitude. Numbers refer to Table 6.2.1.

Table 6.2.1. Key for summary plots (Figures 6.2.1 and 6.2.2).

1	For the conditions corresponding to Figures 4.1.2 and 4.1.3
4	For the conditions corresponding to Figures 4.2.1 and 4.2.2
5	Same as 4 but M_0 increased from 1.25 to 10
6	Same as 4 but upper level lapse rate increased from 3°C/km to 6°C/km
7	Neutral steady state ($R_0 = 10^5$)
8	Neutral steady state ($R_0 = 10^6$)
9	Neutral steady state ($R_0 = 10^7$)
10	Stable atmosphere ($R_0 = 10^6$, $Ri_{(10)} = 0.014$)
11	Stable atmosphere ($R_0 = 10^5$, $Ri_{(10)} = 0.0036$)
12	Stable atmosphere ($R_0 = 10^5$, $Ri_{(10)} = 0.047$)
13	Unstable atmosphere ($R_0 = 10^5$, $Ri_{(10)} = -0.013$, $z_i f/U_g = 0.22$)
14	Unstable atmosphere ($R_0 = 10^5$, $Ri_{(10)} = -0.035$, $z_i/U_g = 0.17$)

In general, the wind shear decreases with altitude in the lower portion of the boundary layer. This is shown in Figure 6.2.3 to supplement the summary information in Figure 6.2.2. The solid curve shows the distribution of wind shear with altitude for the neutral, barotropic distribution of Figure 3.2.1. The bars represent the change in wind shear caused by two orders of magnitude change in Ro. The dashed curves represent the bounds in the variation of wind shear caused by expected values of Ri. In general, increasing Ri will tend to increase wind shear, as seen in Figure 6.2.2, but the minimum wind shear need not coincide with the minimum Ri due to hysteresis effects. Baroclinicity also will, in general, increase wind shear. It is not possible to correlate the variations indicated in Figure 6.2.3 with time of day. Nocturnal hours do tend to be more stable (Ri > 0) and afternoon hours more unstable (Ri < 0), but the baroclinicity is associated with changing weather and does not correlate with time of day. A companion curve like Figure 6.2.3 for the turbulence intensity as a function of altitude would be too misleading, since there is no consistent trend of turbulence intensity with altitude over parameter space. Under stable conditions, the turbulence will decrease with altitude, but for unstable conditions at low levels, it will increase with altitude.

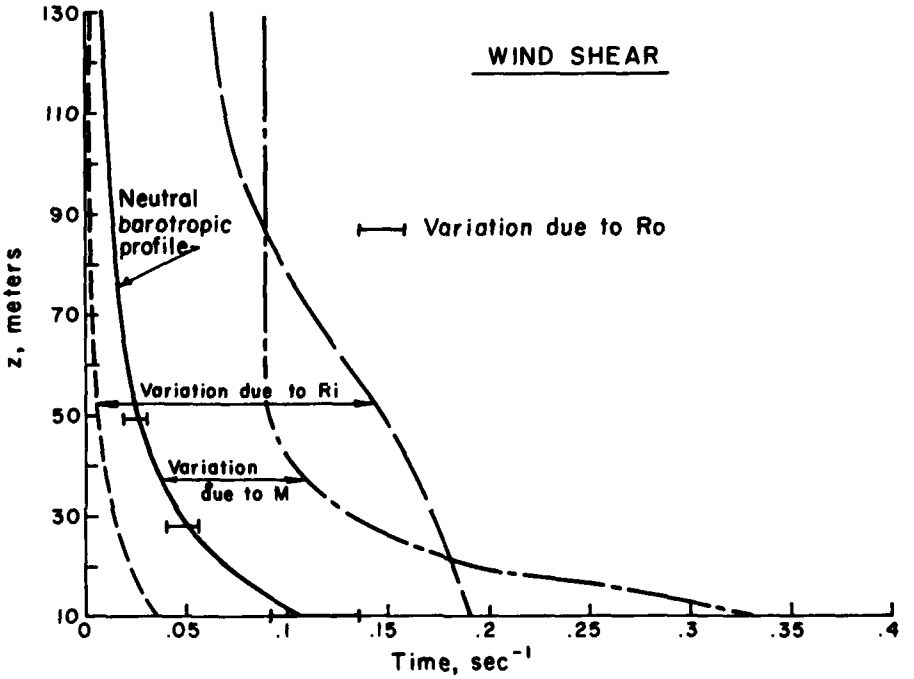

Figure 6.2.3 - Summary plot of wind shear as a function of altitude showing the influence of the expected range of variations in Ro, Ri and M.

Many cases in nature, where wind shear and turbulence are a problem to aviation, are further complicated by the added dimensionality of the phenomena. For example, the strong downdraft associated with flow from a thunderstorm discussed in Section 5.3 presents a horizontal wind shear which can be extremely hazardous. A slender downdraft can persist to a low altitude and create an outflow which has horizontal wind speed changes in excess of 30 m/sec within a few kilometers. Figure 6.2.4 shows the relation of a thunderstorm downdraft, as deduced by Fujita and Caracena (1977), to an Eastern Airlines

aircraft on its fatal final approach to JFK June 24, 1975. Analysis of the flight recorder data indicated that the combination of the downdraft and the sharp change in horizontal wind speed resulting from the outflow from the downdraft were sufficient to cause the crash approximately 1 km short of the runway. The relative contributions of the negative vertical windspeed and the sharp dropoff in the speed of the horizontal head wind are subject to question. McCarthy, et al. (1979), argue that the most critical wind shear is the change in the horizontal wind speed on a time scale of the order of the period of the phugoid oscillation for the particular aircraft.

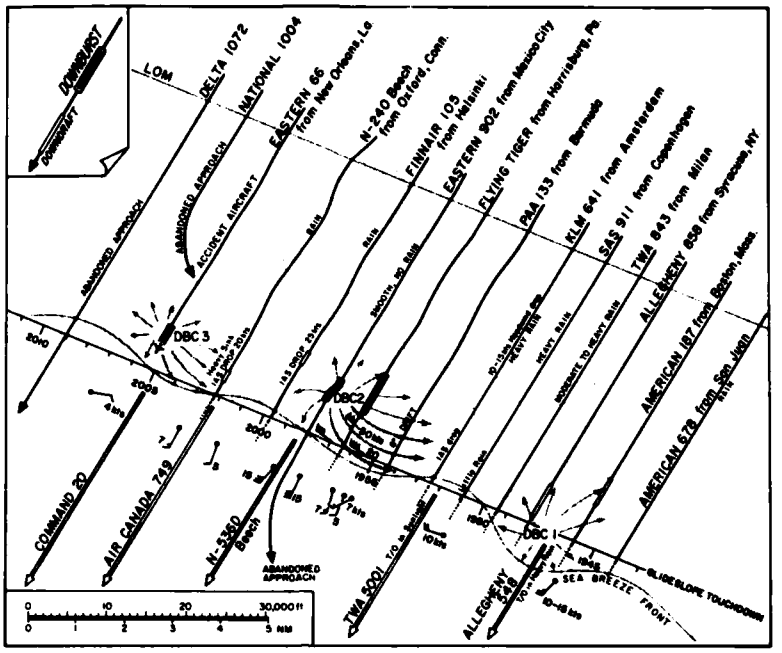

Figure 6.2.4 - Paths of 14 aircraft in 25 min at JFK Airport on 24 June, 1975, as analyzed by Fujita and Caracena (1977). Each path was shifted toward the WNW at 15 m s^{-1} (30 kt) to convert the time into the space relative to the spearhead echo. The echo, as seen by the Atlantic City radar, was 32 km (20 mi) long and 13 km (8 mi) wide, covering the entire area between LOM (Localizer Outer Marker) and the north end of runway 22-L. There were downburst cells (DBCs) along the south edge of the spearhead echo. Five aircraft took off inside the sea breeze without being affected by downbursts.

The strongest wind shear conditions associated with a thunderstorm downdraft will occur under the center of a relatively small diameter downdraft. Fujita (1980) calls such an intense narrow downdraft a "downburst" or "microburst". The downdraft needs to be sufficiently large that the core can penetrate to the surface before the potential temperature defect is eroded by turbulent mixing, yet sufficiently narrow that the maximum radial outflow occurs at a small radius. Under these conditions the horizontal wind shear will scale as $[g\Delta\theta/T_0 h]^{1/2}$ where $\Delta\theta$ is the potential temperature defect between the core of the downdraft and the surrounding ambient air, and h is the height from which the downdraft originates.

The gust front which may emanate for some distance from the downdraft presents a related, but somewhat different wind shear hazard (Goff, 1976). A detection system based on identifying the pressure signal occurring at the surface under such a discrete feature has been developed by Bedard, et al. (1979). Figure 6.2.5 compares a pressure trace they observed at Dulles Airport with the pressure pulse associated

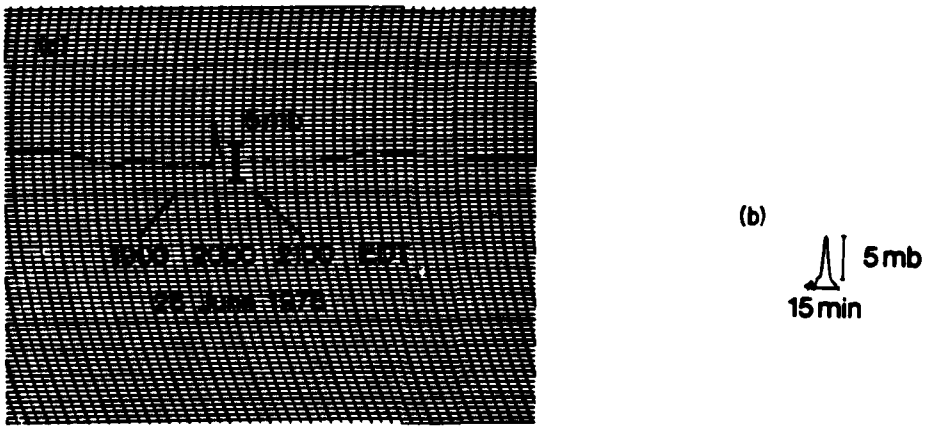

Figure 6.2.5 - Pressure field beneath a thunderstorm downdraft:
(a) as measured on 26 June 1978 by Bedard, et al. (1979); and
(b) as given in numerical simulation by Teske and Lewellen (1978).

with the model simulation discussed in Section 5.3. The traces are quite similar. In both cases there is a small rise followed by a small drop preceeding the main pressure pulse.

The results of model studies such as those discussed herein can provide a physically consistent set of wind and turbulence profiles which may be used to help understand what meteorological conditions lead to hazardous low-level wind shear and turbulence profiles, and to provide model inputs into flight simulators for pilot training. The physical constraints provided by the conservation equations should provide a valuable supplement to simulator models based on correlations of empirical data (e.g., Frost, Camp and Wang, 1978).

6.3. Refractive Index Fluctuations

Turbulent fluctuations in temperature and humidity force fluctuations in the atmospheric refractive index which can interfere with coherent propagation of optical, microwave, or acoustic radiation. These effects, although generally detrimental to communication systems, have formed the basis for remote sensing of the atmosphere. A brief review of the rapidly expanding use of these remote sensors in boundary layer meteorology is given by McBean, et al. (1979). Engineers dealing with either their beneficial results or their interference effects need methods for calculating these fluctuations in the atmospheric boundary layer.

The reflectivity of a distributed source is proportional to the refractive index structure function defined as (Tatarskii, 1971)

$$C_n^2 = \frac{\overline{[n(x) - n(x+r)]^2}}{r^{2/3}} \tag{6.3.1}$$

where n is the index of refraction, r is the separation distance and the overbar denotes an ensemble average. For many applications of interest in the atmospheric boundary layer the scattering length of the propagating wave of interest will fall within the inertial subrange scale of the turbulent spectrum Within this subrange where essentially isotropic turbulence exists, C_n^2 will be independent of r.

The basic turbulent correlations predicted by a model such as the one given in Section 2.3 can be used to predict the refractive index structure function, C_n^2. The combination of primary variables, temperature and humidity variances and covariances required to compute C_n^2 depends upon the wavelength being refracted. A formula for cm-wavelength radar was derived by Lewellen and Teske (1975)

$$C_{n(\text{radar})}^2 = 7.3 \times 10^{-3} \Lambda^{-2/3} \frac{p^2}{T^4} \left\{ \left(1 + \frac{2B\bar{H}}{T}\right) \overline{\theta_v \theta_v} - 2 \left(1 + \frac{2B\bar{H}}{T}\right) (0.61T_\infty + HB) \overline{\theta_v h} + \left[B^2 + \left(1 + \frac{2B\bar{H}}{T}\right)\left[(0.61T_\infty)^2 + 2(0.61T_\infty)B\right]\right] \overline{h^2} \right\} \tag{6.3.2}$$

where B = 7,730, p is in atmospheres, T is temperature in °K and $\bar{H}$ is water vapor mixing ratio. The dominant term in this equation for moderately moist boundary layers is proportional to the humidity fluctuations. Fluctuations in the mixing ratio of the order of a fraction of a gram/Kg across a turbulent layer of the order of ten meters thick are detectable by sensitive radars.

The corresponding formula for optical radiation is

$$C_{n(\text{optical})}^2 = 7.5 \times 10^{-3} \Lambda^{-2/3} \frac{p^2}{T^2} \left\{ \frac{\overline{\theta q}}{T^2} + 0.127 \overline{H^2} - 0.712 \frac{\overline{h\theta_v}}{T^2} \right\} \tag{6.3.3}$$

Expressions for acoustic radiation, as well as optical and microwave, have been given by Wesely (1976). His expressions relate C_n^2 to the individual temperature and water vapor pressure structure parameters, C_T^2, C_e^2, and C_{eT}. His expression for radar is slightly different than that given in Eq. (6.3.2) since he does not include the influence of a mean humidity level, which may be important in the marine boundary layer. Figure 6.3.1, taken from Burk (1981) gives the results of a calculation of C_H^2 throughout the planetary boundary layer using a model (Burk, 1977, 1980) similar to the one-dimensional model presented in Chapters II through IV.

Figure 6.3.1 also includes the mixed layer scaling variation for C_H^2 given by Wyngaard and Lemone (1980) along with their data collection. They also provide scaling relations for the structure functions in the immediate neighborhood of the inversion based on Deardorff's (1979) idealization of the structure of the interfacial layer defined as the region between the height at which the virtual potential flux first goes to zero and the height at which all the turbulence quantities vanish. These expressions may be written as:

$$C_H^2 \approx \frac{3.9(\Delta H)^2\, \theta_{v*}}{z_i^{2/3}\, \Delta\theta_v} \tag{6.3.4}$$

$$C^2_{\theta_v} \approx \frac{\Delta\theta_v\, \theta_{v*}}{2 z_i^{2/3}} \tag{6.3.5}$$

$$C_{\theta_v,H} \approx \frac{2.2(\Delta H)\, \theta_{v*}}{z_i^{2/3}} \tag{6.3.6}$$

where ΔH and $\Delta\theta_v$ are the changes in moisture and virtual potential temperature across the inversion. These relations appear to depend upon the dynamics of the inversion layer being strongly coupled to the surface dynamics through the parameters z_i and θ_{v*}. This need not always be the case. We may expect the turbulence in the inversion to often be driven by local internal wave breaking.

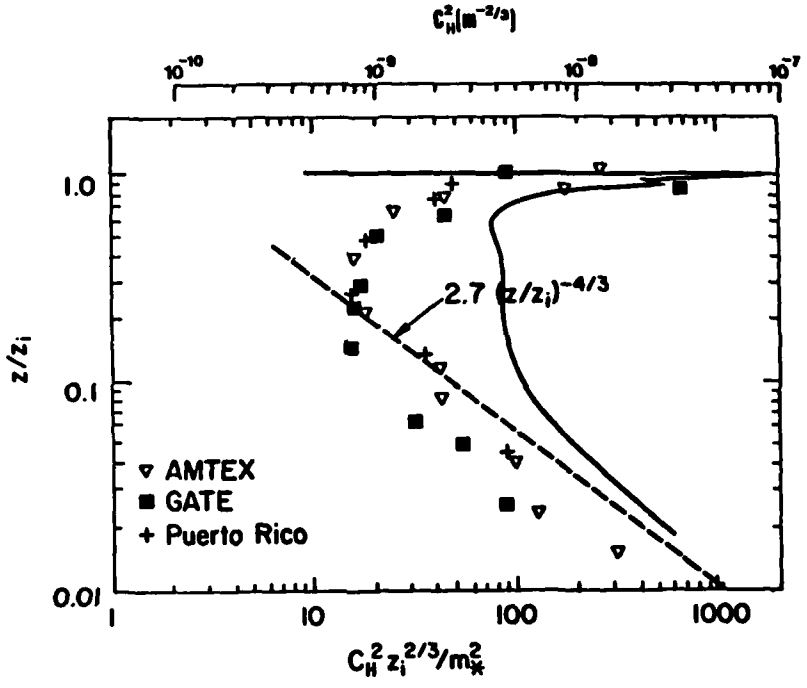

Figure 6.3.1 - Humidity structure function comparison by data and model simulation as given by Burk (1980). Data collection and dashed line, the mixed layer scaling prediction, from Wyngaard and Lemone (1980). Upper scale applies only to solid line.

Figure 6.3.2 gives the contours of C_n^2 predicted to be associated with the simulation given in Section 5.2 for one set of conditions. (Sea surface temperature = 20°C, Ug = 10 m/sec, z_i/L = -10, $\partial\theta/\partial z$ (above mixed layer) = 0.01°/m, H_∞ = 2.5 g/Kg.) This figure shows that the highest values of C_n^2 occur near the surface and in the vicinity of the inversion in agreement with the one-dimensional simulation, but there is also considerable variation across the roll. The large values near the inversion are localized in the region of the rolls where the updraft of moist air interacts most strongly with the dry air above the inversion. Under such conditions the radar return can show the convective streets exemplified in Figure 6.3.3.

The combination of remote sensors capable of looking in great detail at the structure within the atmospheric boundary layer and models able to calculate the turbulent dynamics seen by these sensors should greatly improve our understanding of the rich variety of fluid dynamical structures which occur particularly in the neighborhood of the top of the boundary layer.

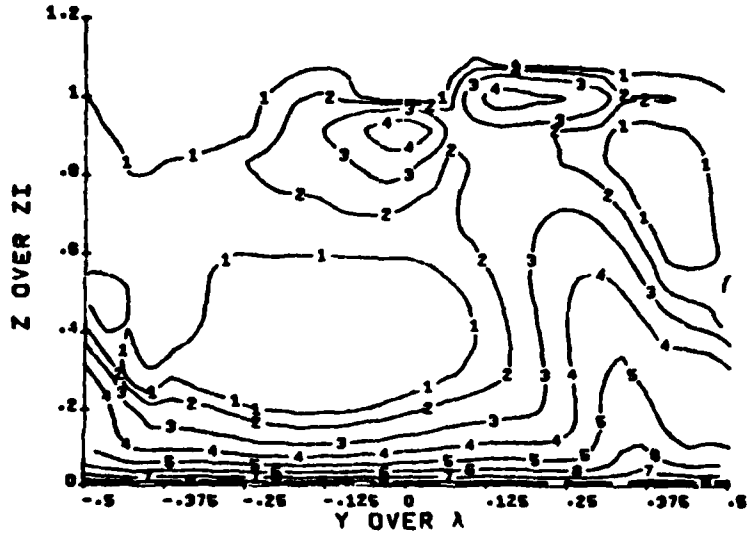

Figure 6.3.2 – Contours of the radar refractivity structure function (C_n^2) within the roll vortices predicted by a model run with T(sea surface) = 20°C, U_g = 10 m/sec, $z_i/L \approx -10$, $\alpha = -10°$, $\partial\theta/\partial z$(above inversion) = 0.01 C/m, Δh (inversion) = 2.5 g/Kg. Contours labeled n denote $2^{(n-7)} \times 10^{-12}$ so that there is a factor of 2 difference between each of the contours.

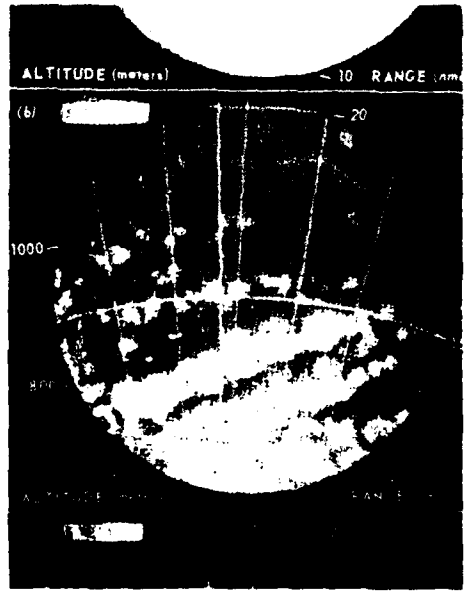

Figure 6.3.3 - PPI photograph taken with an S-band radar at Wallops Island showing alignment of convective cells at the top of the mixed layer. (Konrad, 1970).

6.4. Dry Deposition

The final application considered here is that of the deposition of a trace species from the atmosphere to the surface. This is important to the depletion of plumes transported over long distances. Deposition is the negative of surface evaporation, a phenomenon of utmost importance to agricultural meteorologists. For common industrial pollutants, approximately half of the pollutant is eventually transported to the surface directly by dry deposition with the rest of it washed out of the air by precipitation. Thus dry deposition is an important component of what has become popularly known as the "acid rain" problem.

A number of reviews of deposition have been made (e.g., Sehmel, 1980; Slinn, 1976; Chamberlain, 1979; and McMahon and Denison, 1979). In spite of the relatively large amount of data accumulated, the data can rarely be reliably extrapolated to general field conditions, due either to insufficient documentation of the ambient conditions for the experiment, or to modeling deficiencies. Our aim in the present section is to highlight some of the reasons for the uncertainties surrounding deposition values.

Gaseous and particulate removal rates from a polluted atmosphere to environmental surfaces historically have been reported as deposition velocities, v_d, defined as the flux to the surface $\overline{wc}|_o$ divided by the airborne concentration, C, i.e.,

$$v_d = -\overline{wc}|_o/C(z) \tag{6.4.1}$$

Since a concentration gradient is necessary to deliver a flux to the surface (except in the nominal case of simple gravitational settling of large particles), v_d is necessarily a function of the height at which the normalizing concentration is measured. Figure 6.4.1 gives the deposition velocities tabulated by Sehmel (1980) for a number of different surfaces as measured for one particular species. Dry deposition involves such diverse phenomena as leaf chemistry, plant structure, land use as well as all the factors involved in the turbulent transport of mass and momentum discussed in Chapters 1 through 5. It is more convenient to deal with the resistance of the surface layer to deposition which is defined as the reciprocal of the deposition velocity,

$$R_d = v_d^{-1} \tag{6.4.2}$$

This concept has the advantage that it can conveniently be divided into the resistance of the various layers through which the species of interest must pass to reach the surface.

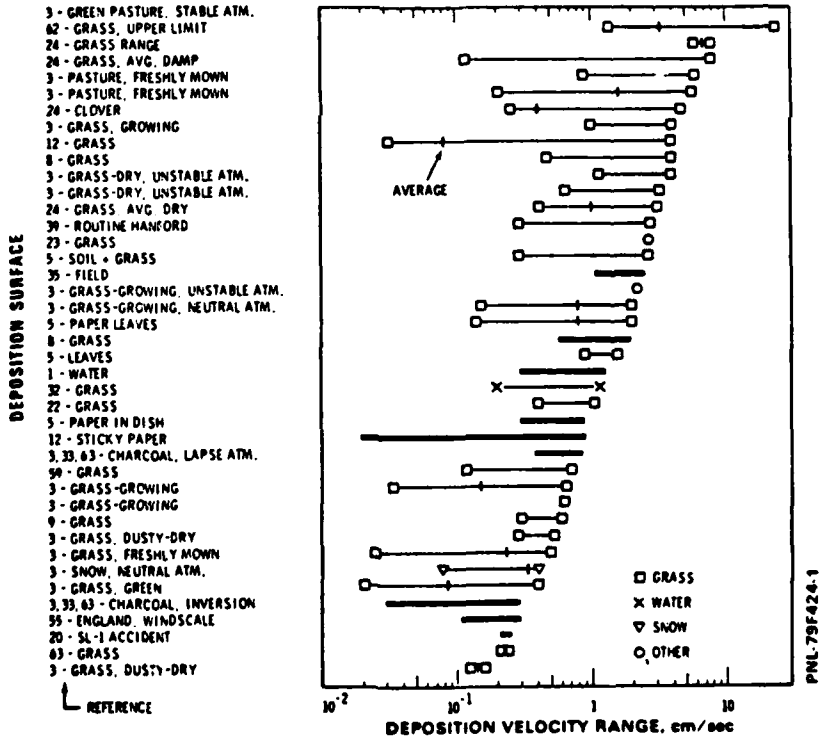

Figure 6.4.1 - Iodine deposition velocity summary as given by Sehmel (1980). Reference number refers to Sehmel's tables.

When the boundary layer is divided into four different regions as shown in Figure 6.4.2, the total resistance to deposition is the sum of resistance presented by each separate region plus a fifth resistance due to absorption or reaction at the surface.

$$v_d = (R_1 + R_2 + R_3 + R_4 + R_5)^{-1} \tag{6.4.3}$$

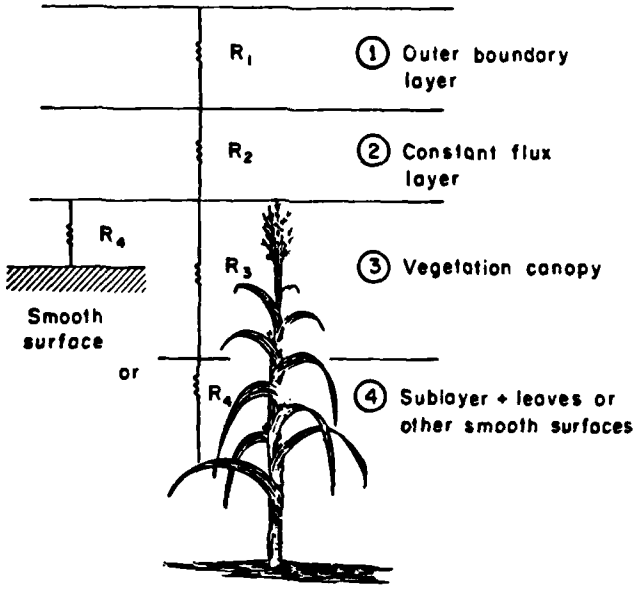

Figure 6.4.2 - Four different regions of the planetary boundary layer for study of the aerodynamic resistance to SO_2 deposition.

For flow over a smooth surface, Region 3, the canopy, does not exist and $R_3 = 0$. When a vegetal canopy exists at the surface, the effective surface area is increased, and R_4 is decreased and may be incorporated within R_3. A fifth resistance, a surface chemical or biological resistance, must be added to the four aerodynamic resistances in the most general case. Each of these layers can be considered separately.

The contribution, R_1, from Region 1, the outer boundary layer, can generally be neglected because the height at which the deposition velocity is generally desired falls within the surface layer covered by Region 2. If the contribution is desired, then the methods discussed in Section 6.1 need to be applied.

The resistance for Region 2 can be obtained directly from ϕ_h, discussed in Section 3.1, since the normalized species gradient is assumed to be the same function of z/L as the normalized temperature gradient. This assumption is based on the similarity of the fundamental heat and species diffusion equations. From Eqs. (6.4.1 and 6.4.2)

$$R_2 = + \int_{z_h}^{z_m} \frac{\phi_h}{\kappa u_*} \frac{dz}{z} \tag{6.4.4}$$

This integral was given in Eq. (3.1.4) for unstable conditions and in Eq. (3.1.11) for stable conditions. For neutral conditions it reduces simply to

$$R_2 = \frac{0.75}{\kappa u_*} \ln \frac{z}{z_h} \tag{6.4.5}$$

The departure of the resistance as a function of height and stability from the log variation is given in Figure 6.4.3. The figure shows a strong effect of both stability and height on deposition during stable conditions and very little effect during unstable conditions.

The smooth surface resistance is determined by the Schmidt number, ν/K_c, of the species diffusing in air, varying approximately as $(\nu/K_c)^{2/3}$. For real surfaces covered with some form of vegetation, this must be combined with a canopy model, such as discussed in Section 3.6, to model the resistance to deposition within the canopy. Figure 6.4.4 shows the sensitivity of the resistance of a typical forest canopy with respect to three important variables according to the model presented by Lewellen and Sheng (1980a). Everything else being equal, the canopy resistance to deposition decreases as the laminar diffusivity of the depositing species increases, as the ratio of the plant leaves' wetted area to the frontal area projected into the wind increases, and also with increasing wind speed.

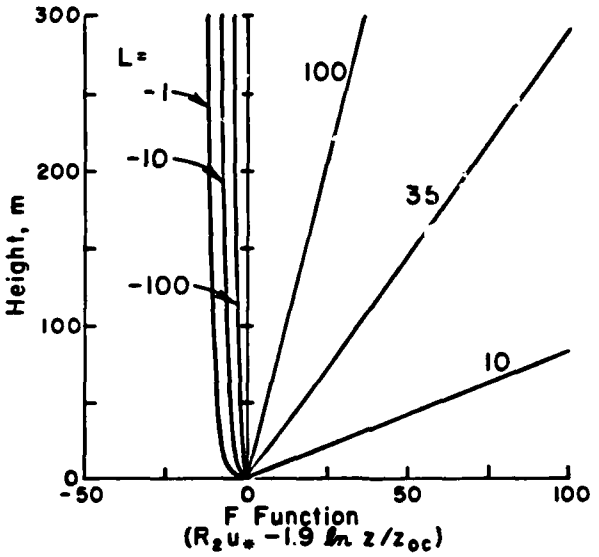

Figure 6.4.3 - Incremental resistance to deposition as a function of height and stability as given by surface layer functions.

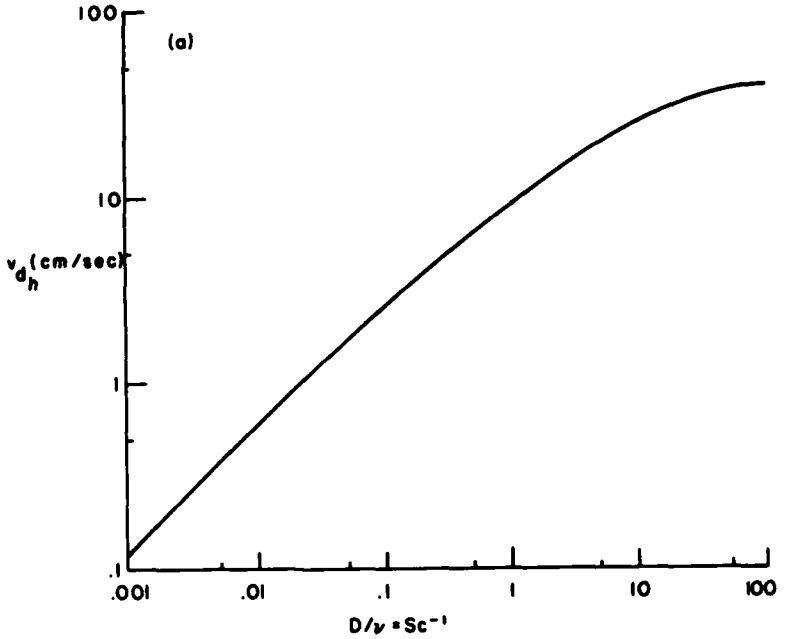

Figure 6.4.4 - Gaseous deposition velocity at the top of the summer forest as a function of three variables (Lewellen and Sheng, 1980a). Plant area index = 3, wet foliage, neutral stability.
(a) As a function of Schmidt number (u_{zh} = 5 m/sec, A_w/A_f = 10, u_* = 70 cm/sec).

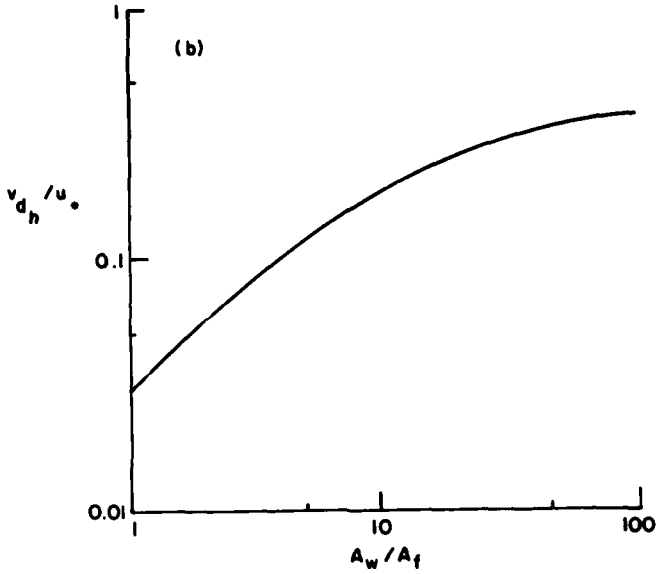

Figure 6.4.4 - (b) As a function of leaf wetted area to frontal area ($D/\nu = 1$, $u_{2h} = 5$ m/sec).

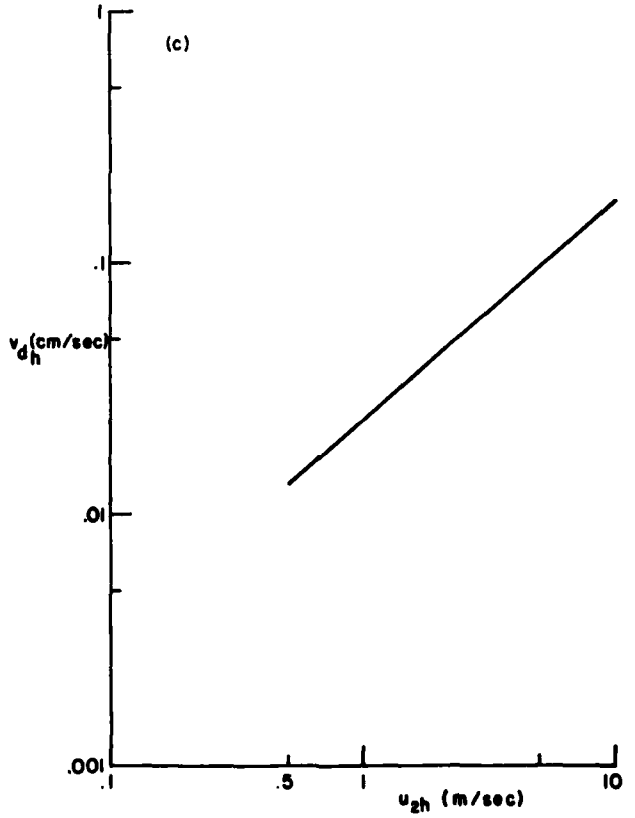

Figure 6.4.4 - (c) As a function of u_{2h} ($D/\nu = 1$, $A_w/A_f = 10$).

Different component resistances will be important in Eq. (6.4.3) under different conditions. Representative estimates for some of the terms under various conditions are given in Table 6.4.1. There are certain conditions where any one of the individual resistances may be the dominant one. In view of Eq. (6.4.3) and Table 6.4.1, it should not be surprising that such a large scatter in numerical values of deposition velocity exists as given in Figure 6.4.1 for a single species. It is also clear that models which parameterize deposition velocity as constant for a particular species are subject to large errors. An attempt at a more detailed parameterization is given by Lewellen and Sheng (1980a).

Table 6.4.1. Representative values of deposition resistance terms in Eq. 6.4.3.

(sec/cm)

	Minimum	Low	Typical	High	Maximum
(1) Aerodynamic turbulent ($R_1 + R_2$)	0.05	0.2	1	5	100
	Unstable flow over rough surface	Modest neutral winds	Light neutral winds	Stable winds	Light stable winds
(2) Laminar sublayer ($R_3 + R_4$)	0.01	0.1	1	20	1000
	Gas species transferred to pine forest	Gas species transferred to smooth surface	0.01 μm particles on pine forest	0.5 μm particles deposited on pine forest under moderate wind conditions	0.5 μm particles deposited on smooth surface
(3) Surface R_5 (for SO_2)	0.02	0.2	0.5	1	10
	(Water)	(Calcarious soil)	(Grass or wheat)	(Pine with open stomata)	(Pine with closed stomata)

VII. Concluding Remarks

Rapid improvements in techniques for predicting the dominant processes in the lower atmosphere may be expected over the next few years due to the fortunate combination of the availability of improved instrumentation for probing this layer, the availability of turbulent transport models for analyzing the sensitivity of turbulent transport in this region to particular variables, and the probable availability of continued funding due to the recognition of the importance of transport in this layer to a number of engineering applications.

A variety of remote sensors based on radio, optical or acoustic techniques are currently being tested. As some of these prove their ability to give good spatial and temporal resolution at a relatively inexpensive unit cost per observation, new applications will be found. The Phoenix Project (Hooke, 1980) is an example of the type of projects which may be expected to play a key role in this development. The interaction of modeler and observer is important to both. Although it is generally recognized that the modeler must have empirical inputs for model development and evaluation, it is equally true that the giant data bases generated by observational programs need inputs from models for guidance in determining which parameters are most critically needed. It is only slightly wastefull when extraneous information is collected and filed, but much more inefficient when the absence of an important variable severely limits the utility of a large data set. Progress is most efficient when there is continued iteration between model formulation and observational testing to determine the model's deficiencies and supply the empirical information needed for improved model parameterization.

Some of the major applications expected to provide the support to drive the continued development of transport modeling in the lower atmosphere have been discussed in some detail in the previous chapter. There are many other areas which may contribute to this support, since they will certainly benefit from the expanded capabilities. These run the spectrum from agricultural planning to zeppelin operations. Some areas which may be expected to have a particularly strong interaction with our increasing knowledge about turbulent transport in the lowest 1 km of the atmosphere are represented in the two volume Proceedings of the 5th International Conference on Wind Engineering (Cermak, 1980). Another area where improved understanding of the boundary layer should reap substantial dividends is in the parameterization of surface influences in large-scale weather forecasting models (Driedonks and Tennekes, 1981). Perhaps the strongest impetus to improved prediction techniques may come from the military. Not only is there the direct requirement of forecasting the natural micrometeorological environment in which men and weapons are called to operate, but there is the potential use of tactical modifications to this environment.

Many important problems fall under the area of the interaction between energy conversion and the environment. The dispersal of the residue from a coal-fired power plant is an obvious example. Less obvious are such things as the impact of the accuracy of dispersal models on emergency planning around nuclear power plants; the possible adverse impact of cooling towers, or ponds, on local fog episodes; and the impact of improved estimates of surface transfer coefficients on questions surrounding the global atmospheric buildup of CO_2 as a limit to our use of fossil fuels. The strong interaction extends into the areas of renewable energy sources and energy conservation. The choice of windmill sites and modes of operation depends on knowledge about the wind behavior close to the surface. The maintenance of active solar energy conversion systems depends on wind damage and dust erosion. Architects are recognizing the influence of siting and landscaping on heating and cooling requirements for buildings.

Many applications could profit from a regional boundary-layer meteorological model based on inputs from regular weather forecasts along with local topographic features, and local sources and sinks of thermal energy, humidity, and effluents of particular interest. Some research models currently are attempting this (e.g., Pielke, 1974; Tapp and White, 1976; and Anthes and Warner, 1978). One model (Long and Shaffer, 1975) attempts this on an operational basis, but on a relatively large grid (80 km between horizontal grid points) so that micrometeorological features cannot be resolved. Advancements in three specific areas are needed to make such a regional model an attractive possibility. First, efficient algorithms for providing sufficient physical constraints must be developed to allow relatively fine mesh calculations at reasonable costs. Second, and perhaps most difficult, is the problem of supplying boundary conditions with adequate resolution in time and space to drive the model. Finally, there is the requirement of processing the large flow of output data in a useful manner for prospective users. Continued reductions in unit computing costs contribute to a high probability of solving the first and third of these, but there is no assurance as to how well the second can be solved. The challenge of following the flow in real time is to provide select data such as might be available from meteorological stations within the domain or satellite remote sensing to supplement the sparse boundary data as proper constraints on the flow. The forecast capability involves this plus the basic question of the limits to predictability in a turbulent atmosphere as discussed by Haltiner and Williams (1980).

REFERENCES

André, J. C., DeMoor, G., Lacarrere, P., and DuVachat, R., (1976); "Turbulence Approximation for Inhomogeneous Flows: Part I. The Clipping Approximation.; Part II. The Numerical Simulation of a Penetrative Convection Experiment", J. Atmos. Sci. 33, 476-491.

André, J. C., DeMoor, G., Lacarrere, P., Therry, G., and DuVachat, R., (1978); "Modeling the 24-Hour Evolution of the Mean and Turbulent Structure of the Planetary Boundary Layer", J. Atmos. Sci. 35, 1861-1883.

Anthes, R. A., and Warner, T. T., (1978); "Development of Mesoscale Models Suitable for Air Pollution and Other Mesometeorological Studies", Monthly Weather Review 106, 1045-1078.

Arya, S. P. S., and Wyngaard, J. C., (1975); "Effect of Baroclinicity on Wind Profiles and the Geostrophic Drag Law for the Convective Planetary Boundary Layer", J. Atmos. Sci. 32, 767-778.

Ball, F. K., (1960); "Control of Inversion Height by Surface Heating", Quart. J. Roy. Meteor. Soc. 86, 483.

Barnes, et al., (1980); "The Structure of a Fair Weather Boundary Layer Based on the Results of Several Measurement Strategies", Monthly Weather Review 107, 349-363.

Bedard, A. J. Jr., Merrem, F. H., Simms, D., and Cairns, M. M., (1979); "A Thunderstorm Gust-Front Detection System", Federal Aviation Administration, Washington, D. C., FAA-RD-79-55.

Betts, A. K., (1973); "Non-Precipitating Cumulus-Convection and Its Parameterization", Quarterly Journal of the Royal Meteorological Society 99, 178-196.

Betts, A. K., (1974); "Further Comments on 'a comparison of the equivalent potential temperature and the static energy'", J. Atmos. Sci. 31, 1713-1715.

Bienkowski, F. S., (1979); "A Simple Semi-Empirical Theory for Turbulence in the Atmospheric Surface Layer", Atmospheric Environment 13, 247-253.

Blackadar, A. K., (1979); "High-Resolution Models of the Planetary Boundary Layer", Advances in Environmental Sciences and Engineering 1, 50-85.

Bodin, S., (1980); "Applied Numerical Modeling of the Atmospheric Boundary Layer", Atmospheric Planetary Boundary Layer Physics (edited by A. Longhetto), Elsevier Scientific Publishing Co., pp. 1-76.

Boussinesq, J., (1903); Théorie Analytique de Chaleur, Vol. 2, Gauthier-Villars, Paris, France.

Bradley, E. F., (1968); "A Micrometeorological Study of Velocity Profiles and Surface Drag in the Region Modified by a Change in Surface Roughness", QJRMS 94, 361-379.

Bradshaw, P., (1972); "The Understanding and Prediction of Turbulent Flows", Aeronaut. J. 76, 403-418.

Brandes, E. A., (1977); "Flow in Severe Thunderstorms Observed by Dual-Doppler Radar", J. Applied Meteorology 16, 333-338.

Brandes, E. A., (1979); "Tornadic Mesocyclone Finestructure and Implications for Tornadogenesis", Proceedings of the 11th AMS Conference on Severe Storms, pp. 549-556.

Brost, R. A., and Wyngaard, J. C., (1978); "A Model Study of the Stably Stratified Planetary Boundary Layer", J. Atmos. Sci. 35, 1427-1440.

Brown, R. A., (1974); Analytical Methods in Planetary Boundary-Layer Modeling, Halstead Press, New York.

Burk, S. D., (1977); "The Moist Boundary Layer with a Higher Order Turbulence Closure Model", J. Atmos. Sci. 34, 629-638.

Burk, S. D., (1980); "Refractive Index Structure Parameters: Time-Dependent Calculations Using a Numerical Boundary Layer Model", J. Applied Meteorology 19, 562-576.

Burk, S. D., (1981); "Comparison of Structure Parameter Scaling Expressions with Turbulence Closure Model Predictions", J. Atmos. Sciences 38, 751-761.

Businger, J. A., Wyngaard, J. C., Izumi, Y., and Bradley, E. F., (1971); "Flux-Profile Relationships in the Atmospheric Surface Layer", J. Atmos. Sci. 28, 181-189.

Businger, J. A., and Arya, S. P. S., (1974); "Height of the Mixed Layer in the Stably Stratified Planetary Boundary Layer", Advances in Geophysics 18A, 73-92.

Cermak, J. E., (1980) (editor); Wind Engineering, Vols. I and II, Pergamon Press.

Chamberlain, A. C., (1979); "Dry Deposition of Sulfur Dioxide", Paper presented at the Symposium on Potential Environmental and Health Effects of Atmospheric Sulfur Deposition, Oak Ridge National Laboratory, Oak Ridge, Tennessee (October).

Charnock, H., (1955); "Wind Stress on a Water Surface", Quart. J. Royal Meteorology Society 81, 639-640.

Chimonas, G., (1980); "Waves, Stability, and Turbulence", Proceedings of the American Meteorological Society Workshop on the Planetary Boundary Layer (edited by J. C. Wyngaard), pp. 67-99.

Cionco, R. M., (1972); "Intensity of Turbulence within Canopies with Simple and Complex Roughness Elements", Boundary Layer Meteorology 2, 453-465.

Clarke, R. H., Dyer, J. A., Brook, R. R., Reid, D. G., and Troup, A. J., (1971); "The Wangara Experiment Boundary Layer Data", Division of Meteorological Physics, CSIRD, Australia, Technical Paper #19.

Coantic, M. F., (1978); "An Introduction to Turbulence in Geophysics and Air-Sea Interactions", AGARDograph #232.

Csanady, G. T., (1973); Turbulent Diffusion in the Environment, Reidel Publishing Company.

Daly, B. J., andd Harlow, F. H., (1970); "Transport Equations in Turbulence", Phys. Fluids 13, 2634-2649.

Davies-Jones, R. P., (1980); "Tornado Dynamics", in Thunderstorms: A Social, Scientific, and Technological Documentary (edited by E. Kessler), to be published by the Princeton University Press, Princeton, New Jersey.

Deardorff, J. W., (1970a); "Preliminary Results from Numerical Integrations of the Unstable Planetary Boundary Layer", J. Atmos. Sci. 27, 1209-1211.

Deardorff, J. W., (1970b); "Convective Velocity and Temperature Scales for the Unstable Planetary Boundary Layer and for Rayleigh Convection", J. Atmos. Sci. 27, 1211-1213.

Deardorff, J. W., (1972); "Numerical Investigation of Neutral and Unstable Planetary Boundary Layers", J. Atmos. Sci. 29, 91-115.

Deardorff, J. W., (1974a); "Three-Dimensional Numerical Study of the Height and Mean Structure of a Heated Planetary Boundary Layer", Boundary-Layer Meteorology 1, 81-106.

Deardorff, J. W., (1974b); "Three-Dimensional Numerical Study of Turbulence in an Entraining Mixed Layer", Boundary Layer Meteorology 1, 199-226.

Deardorff, J. W., (1978a); "Closure of Second- and Third-Moment Rate Equations for Diffusion in Homogeneous Turbulence", Phys. Fluids 21, 525-530.

Deardorff, J. W., (1978b); "Efficient Prediction of Ground Surface Temperature and Moisture, with Inclusion of a Layer of Vegetation", J. Geophys. Res. 83, 1889-1903.

Deardorff, J. W., (1979); "Prediction of Convective Mixed-Layer Entrainment for Realistic Capping Inversion Structure", J. Atmos. Sci. 36, 424-436.

Deardorff, J. W., and Willis, G. E., (1974); "Physical Modeling of Diffusion in the Mixed Layer", in the Proceedings of the Symposium on Atmospheric Diffusion and Air Pollution", Santa Barbara, American Meteorological Society, Boston, pp. 387-391.

Dobbins, R. A., (1979); Atmospheric Motion and Air Pollution, Wiley-Interscience Publication, 323 pp.

Donaldson, C. duP., (1972); "Calculation of Turbulent Shear Flows for Atmospheric and Vortex Motions", AIAA J. 10, 4-12.

Donaldson, C. duP., (1973); "Atmospheric Turbulence and the Dispersal of Atmospheric Pollutants", AMS Workshop on Micrometeorology (edited by D. A. Haugen), Science Press, Boston, pp. 313-390.

Driedonks, A. G. M., and Tennekes, H., (1981); "Parameterization of the Atmospheric Boundary Layer in Large-Scale Models", Bulletin of the American Meteorological Society 62, 594-598.

Einaudi, F., (1980); "Gravity Waves and the Atmospheric Boundary Layer", Atmospheric Boundary Layer Physics (edited by A. Longhetto), Elsevier Scientific Publishing Company, pp. 77-94.

Feigel'son, E. M., (1964); Light and Heat Radiation in Stratus Clouds, Nauka, (Israel Program for Scientific Translation, 1966), 245 pp.

Feigel'son, E. M., (1970); Radiant Heat Transfer in a Cloudy Atmosphere, Gidrometeor., (Israel Program for Scientific Translation, 1973), 191 pp.

Fox, D. G. (1981); "Judging Air Quality Model Performance - Summary of the AMS Woods Hole Workshop," Bulletin of the American Meteorological Society 62, 599-615.

Friedlander, S. K., (1977); Smoke, Dust and Haze, John Wiley and Sons, New York, New York, 312 pp.

Frost, W., Camp, D. W., and Wang, S. T., (1973); "Wind Shear Modeling for Aircraft Hazard Definition", Federal Aviation Administration, Washington, D. C., FAA-RD-78-3.

Fujita, T. T., (1980); "Downbursts and Microbursts - An Aviation Hazard", Preprints 19th Conference on Radar Meteorology, American Meteorological Society, Boston, Massachusetts, pp. 94-101.

Fujita, T. T., and Caracena, F., (1977); "An Analysis of Three Weather-Related Aircraft Accidents", Bull. Am. Meteor. Soc. 11, 1165-1181.

Fujita, T. T., Pearson, A. D., Forbes, T. A., Umenhofer, T. A., Pearl, E. W., and Tecson, J. J., (1976); "Photogrammetric Analyses of Tornadoes", Proceedings of the Symposium on Tornadoes: Assessment of Knowledge and Implications for Man, Texas Tech University (Edited by R. E. Peterson), pp. 43-88.

Gibson, M. M., and Launder, B. E., (1978); "Ground Effects on Pressure Fluctuations in the Atmospheric Boundary Layer", J. Fluid Mech. 86, 491-511.

Goff, R. C., (1976); "Vertical Structure of Thunderstorm Outflows", Monthly Weather Review 104, 1429-1440.

Goody, R. M., (1964); Atmospheric Radiation, Clarendon Press, 436 pp.

Haltiner, G. J., and Williams, R. T., (1980); Numerical Prediction and Dynamic Meteorology, John Wiley and Sons, New York.

Hanjalic, K., and Launder, B. E., (1972); "A Reynolds Stress Model of Turbulence and Its Application to Thin Shear Flows", J. Fluid Mech. 52, 609-638.

Harlow, F. H., and Nakayama, P. I., (1967); "Turbulence Transport Equations", Phys. Fluids 10, 2323-2332.

Haugen, D. A., (1973) (editor); Workshop on Micrometeorology, Science Press, Boston.

Herbert and Panhaus (1979); "Theoretical Studies of the Parameterization of the Non-Neutral Surface Boundary Layer. Part I: Governing Physical Concepts", Boundary Layer Meteorology 16, 155-167.

Hilst, G. R. (1978); "Plume Model Validation," EPRI EA-917-SY, October 1978.

Hilyer, M. J., et al. (1979); "Procedures for Evaluating the Performance of Air Quality Simulation Models," Systems Applications, Inc., EPA/450/4-79-033, October 1979.

Hooke, W. H., (1980); "Project PHOENIX: An Overview", Proceedings of the 19th Radar Meteorology Conference, American Meteorological Society, pp. 629-643.

Howard, L. N., (1961); "Note on a Paper by John W. Miles", J. Fluid Mech. 10, 509-512.

Hunt, J. C. R., (1980); "Wind over Hills", AMS Workshop on the Planetary Boundary Layer, (Edited by J. C. Wyngaard), pp. 107-144.

Kaimal, J. C., (1978); "Horizontal Velocity Spectra in an Unstable Surface Layer", J. Atmos. Sci. 35, 18-24.

Klemp, J. B., and Wilhelmson, R. V., (1978); "The Simulation of Three-Dimensional Convective Storm Dynamics", J. Atmos. Sci. 35, 1070-1076.

Konrad, T. G., (1970); "The Dynamics of the Convective Process in Clear Air as Seen by Radar", J. Atmos. Sci. 27, 1138-1147.

Launder, B. E., Reece, G. J., and Rodi, W., (1975); "Progress in the Development of a Reynolds-Stress Turbulence Closure", J. Fluid Mech. 68, 537-566.

Leipper, D. F., (1948); "Fog Development at San Diego, California", Sears. Found. J. Mar. Res., 337-346.

Lemone, M. A., (1976); "Modulation of Turbulence Energy by Longitudinal Rolls in an Unstable Planetary Boundary Layer", J. Atmos. Sci. 33, 1308-1320.

Lemone, M. A., (1980); "The Marine Boundary Layer", AMS Workshop on the Planetary Boundary Layer, (Edited by J. C. Wyngaard), pp. 182-231.

Lenschow, D. H., (1970); "Airplane Measurements of Planetary Boundary Layer Structure", J. Applied Meteorology 9, 874-884.

Lenschow, D. H., (1974); "Model of the Height Variation of the Turbulent Kinetic Energy Budget in the Unstable Boundary Layer", J. Atmos. Sci. 31, 465-474.

Lenschow, D. H., and Johnson, W. B., (1968); "Concurrent Airplane and Balloon Measurements of Atmospheric Boundary-Layer Structure Over a Forest", J. Applied Meteorology 7, 79-89.

Lenschow, D. H., Wyngaard, J. C., and Pennell, W. T., (1980); "Mean-Field and Second-Moment Budgets in a Baroclinic, Convective Boundary Layer", J. Atmos. Sci. 37, 1313-1326.

Lewellen, W. S., (1977a); "Influence of Body Forces on Turbulent Transport Near a Surface", J. App. Math. and Phys. (ZAMP) 28, 825-834.

Lewellen, W. S., (1977b); "Use of Invariant Modeling", in Handbook of Turbulence, (edited by Walter Frost and Trevor H. Moulden), Plenum Publishing Corporation, Vol. 1, pp. 237-280.

Lewellen, W. S., Oliver, D. A., Teske, M. E., Segur, H., and Coté, (1977); "1977 Status Report on Low-Level, Atmospheric Turbulence Model for Marine Environments", A.R.A.P. Report #320, A.R.A.P., Inc., Princeton, New Jersey.

Lewellen, W. S., and Teske, M. E., (1973); "Prediction of the Monin-Obukhov Similarity Functions from an Invariant Model of Turbulence", J. Atmos. Sci. 30, 1340-1345.

Lewellen, W. S., and Teske, M. E., (1975); "Development of a Low Level Atmospheric Turbulence Model for Marine Environments", A.R.A.P. Report No. 255, A.R.A.P., Inc., Princeton, New Jersey.

Lewellen, W. S., and Teske, M., (1976a); "Second-Order Closure Modeling of Diffusion in the Atmospheric Boundary Layer", Boundary Layer Meteorol. 10, 69-90.

Lewellen, W. S., and Teske, M., (1976b); "A Second-Order Closure Model of Turbulent Transport Diffusion in the Coastal Planetary Boundary Layer", Proceedings of the AMS Conference on Coastal Meteorology.

Lewellen, W. S., Teske, M., Contiliano, R. M., Hilst, G. R., and Donaldson, C. duP., (1974); "Invariant Modeling of Turbulent Diffusion in the Planetary Boundary Layer", Environmental Protection Agency Report No. EPA-650/4-74-035.

Lewellen, W. S., Teske, M., and Donaldson, C. duP., (1974); "Turbulence Model of Diurnal Variations in the Planetary Boundary Layer", Proceedings of the 1974 Heat Transfer and Fluid Mechanics Institute (edited by L. R. Davies and R. E. Wilson), Stanford University Press, Stanford, California, pp. 301-319.

Lewellen, W. S., Teske, M. E., and Donaldson, C. duP., (1976); "Variable Density Flows Computed by a Second-Order Closure Description of Turbulence", AIAA J. 14, 382-387.

Lewellen, W. S., Teske, M. E., Oliver, D. A., Sheng, Y. P., and Segur, H., (1979); "1979 Status Report on the Development of a Low-Level Atmospheric Turbulence Model for Marine Environments", A.R.A.P. Report No. 385, A.R.A.P., Inc., Princeton, New Jersey.

Lewellen, W. S., and Sandri, G., (1980); "Incorporation of an Anisotropic Scale into Second-Order Closure Modeling of the Reynolds Stress Equation", A.R.A.P. Tech Memo No. 80-11, A.R.A.P., Inc., Princeton, New Jersey.

Lewellen, W. S., and Sheng, Y. P., (1980a); "Modeling of Dry Deposition of SO_2 and Sulfate Aerosols", EPRI Report No. EA-1452, Electric Power Research Institute, Palo Alto, California.

Lewellen, W. S., and Sheng, Y. P., (1980b); "Modeling Tornado Dynamics", Nuclear Regulatory Commission, NUREG/CR-1585, 227 pp.

Lewellen, W. S., Teske, M. E., and Sheng, Y. P., (1980); "Micrometeorological Applications of a Second-Order Closure Model of Turbulent Transport", in Turbulent Shear Flows 2, Selected Papers from the Second International Symposium on Turbulent Shear Flows, Imperial College London, July 2-4, 1979, Springer-Verlag (New York), pp. 366-378.

Lewellen, W. S., and Williamson, G. G., (1976); "Wind Shear Around Airports", National Aeronautics and Space Administration, Washington, D. C., NASA Contractor Report No. NASA CR-2752.

Lilly, D. K., (1968); "Models of Cloud-Topped Mixed Layers Under a Strong Inversion", QJRMS 94, 292-309.

Lilly, D. K., (1969); "The Representation of Small-Scale Turbulence in Numerical Simulation Experiments", Proceedings of the IBM Scientific Computing Symposium on Environmental Sciences, pp. 195-209.

Londergan, R. J., Mangano, J. J., Bowne, N. E., Murray, D. R., and Borenstein, N., (1980); "An Evaluation of Short-Term Air Quality Models Using Tracer Study Data", American Petroleum Institute Report #4333, Vols. I and II.

Long, R. R., (1970); "A Theory of Turbulence in Stratified Fluids", J. Fluid Mech. 42, 349-365.

Long, P. E., and Shaffer, W. A., (1975); "Some Physical and Numerical Aspects of Boundary Layer Modeling", NOAA Tech. Memo NWS TDL-56.

Longhetto, A., (1980); Atmospheric Planetary Boundary Layer Physics, Elsevier Scientific Publishing Company.

Lumley, J. L., and Khajeh-Nouri, B., (1974); "Computational Modeling of Turbulent Transport", Advances in Geophysics, Vol. 18A, Academic Press, New York, pp. 169-192.

Lumley, J. L., (1978); "Computational Modeling of Turbulent Flows", Advances in Applied Mechanics 18, 123-176.

Lumley, J. L., (1979); "Simulating Turbulent Transport in Urban Air-Pollution Models", Advances in Environmental Science and Engineering 1, 103-127.

Lumley, J. L., (1980); "A New Kind of Realizability in Turbulence Modeling of the Planetary Boundary Layer", Proceedings of the AMS Workshop on the Planetary Boundary Layer, (Edited by J. C. Wyngaard), pp. 158-181.

Lumley, J. L., Zeman, O., and Siess, J., (1978); "The Influence of Buoyancy on Turbulent Transport", J. Fluid Mech. 84, 581-597.

Lyons, W. A.,, (1975); "Turbulent Diffusion and Pollutant Transport in Shoreline Environments", Lectures on Air Pollution and Environmental Impact Analyses (Edited by D. A. Haugen) American Meteorological Society, pp. 136-208.

Mack, E. J., Katz, U., Rogers, C., and Pilié, R., (1974); "The Microstructure of California Coastal Stratus and Fog at Sea", Calspan Corporation Report No. CJ-5405-M-1.

Mack, E. J., Pilié, R., and Kockmond, W. C., (1973); "An Investigation of the Microphysical and Micrometeorological Properties of Sea Fog", Calspan Corporation Report No. CJ-5237-M-1.

Manabe, S., and Strickler, R. F., (1964); "On the Thermal Equilibrium of the Atmosphere with a Convective Adjustment", J. Atmos. Sci. 21, 361-385.

Mason, P. J., and Sykes, R. I., (1980); "A Two-Dimensional Numerical Study of Horizontal Roll Vortices in the Neutral Atmospheric Boundary Layer", Quarterly Journal of the Royal Meteorological Society 106, 351-366.

McBean, G. A., Bernhardt, K., Bodin, S., Litynska, A., Van Ulden, A. P., and Wyngaard, J. C., (1979); "The Planetary Boundary Layer", World Meteorological Organization, Technical Note #165.

McCarthy, J., Blick, E. F., and Bensch, R. R., (1979); "Jet Transport Performance in Thunderstorm Wind Shear Conditions", NASA, Washington, D. C., NASA CR-3207, 53 pp.

McMahon, T. A., and Denison, P. J., (1979); "Empirical Atmospheric Deposition Parameters - A Survey", Atmospheric Environment 13, 571-585.

Mellor, G. L., (1973); "Analytic Prediction of the properties of stratified planetary surface layers", J. Atmos. Sci. 30, 1061-1069.

Mellor, G. L., (1977); "The Gaussian Cloud Model Relations", J. Atmos. Sci. 34, 356-358.

Mellor, G. L., and Herring, H. J., (1973); "A Survey of the Mean Turbulent Field Closure Models", AIAA J. 11, 590-599.

Mellor, G. L., and Yamada, T., (1974); "A Hierarchy of Turbulence Closure Models for Planetary Boundary Layers", J. Atmos. Sci. 31, 1791-1806.

Mellor, G. L., and Yamada, T., (1978); "A Turbulence Model Applied to Geophysical Fluid Problems", Symposium on Turbulent Shear Flows (April 1977), Pennsylvania State University, University Park, Pennsylvania, pp. 6.1-6.14.

Miles, J. W., (1961); "On the Stability of Heterogeneous Shear Flow", J. Fluid Mech. 10, 496-508.

Mitchell, K. E., (1975); "A Numerical Investigation of Severe Thunderstorm Gust Fronts", NASA CR-2635, National Aeronautics and Space Administration, Washington, D. C.

Moeng, C. H., and Arakawa, A., (1980); "A Numerical Study of a Marine Subtropical Stratus Cloud Layer and Its Stability", J. Atmos. Sci. 37, 2661-2676.

Monin, A. S., and Obukhov, A. M., (1953); "Dimensionless Characteristics of Turbulence in the Atmospheric Surface Layer", Dokl. Akad. Nauk. SSSR 93, 223-226.

Montieth, J. L. (ed.), (1975); Vegetation and the Atmosphere, Academic Press.

Naot, D., Shavit, A., and Wolfshtein, M., (1973); "Two-Point Correlation Model and the Redistribution of Reynolds Stresses", Phys. Fluids 16, 738-743.

Neiberger, M., (1944); "Temperature Changes During Formation and Dissipation of West Coast Stratus", J. Meteor. 1, 29-41.

Neiberger, M., Johnson, D. S., Ehnien, C., (1961); "Studies Over the Eastern Pacific Ocean in Summer, I. The Inversion Over the Eastern North Pacific Ocean", University of California Publication Meteorology, No. 1.

O'Brien, J. J., (1970); "A Note on the Vertical Structure of Eddy Exchange Coefficients in the Planetary Boundary Layer", J. Atmos. Sci. 27, 1213-1215.

Oliver, D. A., Lewellen, W. S., and Williamson, G. G., (1978); "The Interaction between Turbulent and Radiative Transport in the Development of Fog and Low-Level Stratus", J. Atmos. Sci. 35 (2), 301-316.

Panhaus, W. G., and Herbert, F., (1979); "Theoretical Studies of the Parameterization of the Non-Neutral Surface Boundary Layer. Part II: An Improved Similarity Model", Boundary-Layer Meteorology 16, 169-179.

Pasquill, F., (1974); Atmospheric Diffusion, Second Edition, Halstead Press, John Wiley and Sons, New York.

Paulson, C. A., (1970); "The Mathematical Representation of Wind Speed and Temperature Profiles in the Unstable Atmospheric Surface Layer", J. Appl. Meteorology 9, 857-861.

Pepper, D. W. (1981); Results from the Savannah River Laboratory Model Validation Workshop, 19-21 November 1980," AMS 5th Symposium on Turbulence, Diffusion, and Air Pollution, March 1981.

Pielke, R. A., (1974a); "A 3-D Numerical Model of the Sea Breezes", Monthly Weather Review 102, 115-139.

Pielke, R. A., (1974b); "A Comparison of Three-Dimensional and Two-Dimensional Numerical Predictions of Sea Breezes", J. Atmos. Sci. 31, 1577-1585.

Plate, E. J., (1971); Aerodynamic Characteristics of the Atmospheric Boundary Layer, AEC Critical Review Series, 190 pp.

Pruppacher, H. R., and Klett, J. D., (1978); Microphysics of Clouds and Precipitation, D. Reidel, 714 pp.

Rao, K. S., and Snodgrass, H. F., (1979); "Some Parameterizations of the Nocturnal Boundary Layer", Boundary Layer Meteorology 17, 15-28.

Rao, K. S., Wyngaard, J. C., and Coté, O. R., (1974); "The Structure of the Two-Dimensional Internal Boundary Layer Over a Sudden Change of Surface Roughness", J. Atmos. Sci. 31, 738-746.

Raupach, M. R., and Thom, A. S., (1981); "Turbulence in and above Plant Canopies", Annual Review of Fluid Mechanics 13, 97-130.

Reynolds, W. C., (1976); "Computation of Turbulent Flows", Ann. Rev. Fluid Mech. 8, 183-208.

Rodi, W., (1972); "The Prediction of Free-Turbulent Boundary Layers by Use of a Two-Equation Model of Turbulence", Ph.D. dissertation, Mechanical Engineering Department, Imperial College, London, December.

Rotta, J. C., (1951); "Statische Theorie Nichthomogener Tubulenz", Z. Phys. 129, 547-572.

Rotta, J. C., (1972); Turbulence Strömungen, Teubner Press, Stuttgart, West Germany.

Ruff, R. E., Javitz, H. S., and Irwin, J. S. (1979); "Development and Application of a Statistical Methodology to Evaluate the Realtime Air Quality Model (RAM), AMS/APCA Second Joint Conference on Applications of Air Pollution Meteorology, 1980; (also see 4 volume SRI report on Project 6868, "Evaluation of the Real-Time Air-Quality Model using the RAPS Data Base, April 1979).

Schubert, W. H., (1976); "Experiments with Lilly's Cloud-Topped Mixed Layer Model", J. Atmos. Sci. 33, 436-446.

Schumann, U., (1977); "Realizability of Reynolds-Stress Turbulence Models", The Physics of Fluids 20, 721-725.

Sehmel, G. A., (1980); "Particle and Gas Dry Deposition: A Review", Atmospheric Environment 14, 983-1011.

Shaw, R. H., Silversides, R. H., and Thurtell, G. W., (1974); "Some Observations of Turbulence and Turbulent Transport within and above Plant Canopies", Boundary-Layer Meteorology 5, 429-449.

Shir, C. C., (1973); "A Preliminary Numerical Study of Atmospheric Turbulent Flows in the Idealized Planetary Boundary Layer", J. Atmos. Sci. 30, 1327-1339.

Slinn, W. G. N., (1976); "Dry Deposition and Resuspension of Aerosol Particles - A New Look at Some Old Problems. Atmospheric Surface Exchange of Particulate and Gaseous Pollutants", ERDA Symposium, Series 38, pp. 1-40.

Sommeria, G., (1976); Three-Dimensional Simulation of Turbulent Processes in an Undisturbed Trade Wind Boundary Layer", J. Atmos. Sci. 33, 216-241.

Sommeria, G., and Deardorff, J. W., (1977); "Subgrid-Scale Condensation in Models of Nonprecipitating Clouds", J. Atmos. Sci. 34, 344-355.

Sommeria, G., and Lemone, M. A., (1978); "Direct Testing of a Three-Dimensional Model of the Planetary Boundary Layer Against Experimental Data", J. Atmos. Sci. 35, 25-39.

Sun, W. Y., and Ogura, Y., (1980); "Modeling the Evolution of the Convection Planetary Boundary Layer", J. Atmos. Sci. 37, 1558-1572.

Tapp, M. C., and White, P. W., (1976); "A Nonhydrostatic Meso-Scale Model", QJRMS 102, 277-296.

Tatarskii, V. I., (1971); "The Effects of the Turbulent Atmosphere on Wave Propagation", NOAA TT 68-50464, 471 pp, (available from NTIS, Springfield, Vermont).

Taylor, G. I., (1917); "The Formation of Fog and Mist", QJRMS 43, 241-268.

Telford, J. L., and Warner, J., (1964); "Fluxes of Heat and Vapor in the Lower Atmosphere Derived from Aircraft Measurements", J. Atmos. Sci. 21, 539-548.

Tennekes, H., (1973); "Similarity Laws and Scale Relations in Planetary Boundary Layers", AMS Workshop on Micrometeorology (edited by D. A. Haugen) Science Press, pp. 177-216.

Teske, M. E., and Lewellen, W. S., (1977); "Turbulent Transport Model of a Thunderstorm Gust Front", Proceedings of the 10th Conference on Severe Local Storms (Omaha, Nebraska; Oct. 18-21), AMS, pp. 457-462.

Teske, M. E., Lewellen, W. S., and Segur, H., (1978); "The Prediction of Turbulence and Wind Shear Associated with Thunderstorm Gust Fronts", Proceedings of the Conference on Atmospheric Environment of Aerospace Systems and Applied Meteorology, American Meteorological Society, New York, New York, (November 14-16), pp. 118-123.

Teske, M. E., and Lewellen, W. S., (1979); "Horizontal Roll Vortices in the Planetary Boundary Layer", Proceedings of the 4th Symposium on Turbulence, Diffusion and Air Pollution, American Meteorological Society, pp. 456-463.

Teske, M. E., and Lewellen, W. S., (1978); "Turbulence Modeling Applied to Buoyant Plumes", Environmental Protection Agency, EPA Report #EPA-600/4-78-050.

Turner, D. B., (1979); "Atmospheric Dispersion Modeling - A Critical Review", Journal of the Air Pollution Control Association 29, 502-519.

Turner, J. S., (1973); Buoyancy Effects in Fluids, Cambridge University Press, Great Britain, 367 pp.

Umenhofer, T. A., and Fujita, T. T., (1977); "Great Bend Tornadoes of August 30, 1974", Proceedings of the 10th Conference on Severe Local Storms (Omaha, Nebraska; Oct. 18-21), AMS, pp. 457-462.

Walter, B. A., (1980); "Wintertime Observations of Roll Clouds over the Bering Sea", Monthly Weather Review 12, 2024-2031.

Wesely, M. L., (1976); "The Combined Effect of Temperature and Humidity Fluctuations on Refractive Index", J. Appl. Meteor. 15, 43-49.

Wilcox, D. C., and Alber, I. E., (1972); "A Turbulence Model for High Speed Flows", Proceedings of the 1972 Heat Transfer and Fluid Mechanics Institute, Stanford University Press, Stanford, California, pp. 231-252.

Willis, G. E., and Deardorff, J. W., (1974); "A Laboratory Model of the Unstable Planetary Boundary Layer", J. Atmos. Sci. 31, 1297-1307.

Williamson, G. G., Lewellen, W. S., and Teske, M. E., (1977); "Model Predictions of Wind and Turbulence Profiles Associated with an Ensemble of Aircraft Accidents", NASA CR-2884, National Aeronautics and Space Administration, Washington, D. C.

Wilson, N. R., and Shaw, R. H., (1977); "A Higher Order Closure Model for Canopy Flow", J. App. Meteoro. 16, 1197-1205.

Wippermann, F., (1973); The Planetary Boundary-Layer of the Atmosphere, Deutscher Wetterdienst, 346 pp.

Wu, J., (1969); "Froude Number Scaling of Wind-Stress Coefficients", J. Atmos. Sci. 26, 408-413.

Wyngaard, J. C., (1975); "Modeling the Planetary Boundary Layer - Extension to the Stable Case", Boundary Layer Meteorology 9, 441-460.

Wyngaard, J. C., (1980a); "The Atmospheric Boundary Layer-Modeling and Measurements", Turbulent Shear Flows II, Selected Papers from the Second Symposium on Turbulent Shear Flows, Imperial College, London, (July 1979), Springer-Verlag.

Wyngaard, J. C., (1980b) (Editor); "Proceedings of a Workshop on the Planetary Boundary Layer", American Meteorological Society, Boston, Massachusetts, 321 pp.

Wyngaard, J. C., and Coté, O. R., (1974); "The Evolution of a Convective Planetary Boundary Layer - A Higher Order-Closure Model Study", Boundary Layer Meteorol. 7, 289-308.

Wyngaard, J. C., Coté, O. R., and Izumi, Y., (1971); "Local Free Convection, Similarity and the Budgets of Shear Stress and Heat Flux", J. Atmos. Sci. 28, 1171-1182.

Wyngaard, J. C., Coté, O. R., and Rao, K. S., (1974); "Modeling the Atmospheric Boundary Layer", Advances in Geophysics, Vol. 18A, Academic Press, New York, pp. 193-212.

Wyngaard, J. C., and Lemone, M. A., (1980); "Behavior of the Refractive Index Structure Parameter in the Entraining Convective Boundary Layer", J. Atmos. Sci. 37, 1573-1585.

Wyngaard, J. C., Pennell, W. T., Lenschow, D. H., and LeMone, M. A., (1978); "The Temperature-Humidity Covariance Budget in the Convective Boundary", J. Atmos. Sci. 35, 47-58.

Yamada, T., (1978); "A Three-Dimensional, Second-Order Closure Numerical Model of Mesoscale Circulations in the Lower Atmosphere", Argonne National Laboratory, ANL/RER-78-1, 67 pp.

Yamada, T., (1979a); "An Application of a Three-Dimensional Simplified Second-Moment Closure Model to Study Atmospheric Effects of a Large Cooling-Pond", J. Atmospheric Environment, 693-704.

Yamada, T., (1979b); "Prediction of the Nocturnal Surface Inversion Height", J. Appl. Meteor. 18, 526-531.

Yamada, T., and Mellor, G. L., (1975); "A Simulation of the Wangara Atmospheric Boundary Layer Data", J. Atmos. Sci. 32, 2309-2329.

Yamada, T., and Mellor, G. L., (1979); "A Numerical Simulation of BOMEX Data Using a Turbulence Closure Model Coupled with Ensemble Cloud Relation", Quarterly Journal of the Royal Meteorological Society 105, 915-944.

Zeman, O., (1981); "Progress in the Modeling of Planetary Boundary Layers", Annual Review of Fluid Mechanics 13, 253-272.

Zeman, O., and Lumley, J. L., (1976); "Modeling Buoyancy Driven Mixed Layers", J. Atmos. Sci. 33, 1974-1988.

Zilitinkevich, S. S., (1972); "On the Determination of the Height of the Ekman Boundary Layer", Boundary Layer Meteorology 3, 141-145.

Zilitinkevich, S. S., (1975); "Resistance Laws and Prediction Equations for the Depth of the Planetary Boundary Layer", J. Atmos. Sci. 32, 741-752.

REPORT DOCUMENTATION PAGE

1. Recipient's Reference	2. Originator's Reference	3. Further Reference	4. Security Classification of Document
	AGARD-AG-267	ISBN 92-835-1407-6	UNCLASSIFIED

5. Originator Advisory Group for Aerospace Research and Development
North Atlantic Treaty Organization
7 rue Ancelle, 92200 Neuilly sur Seine, France

6. Title

MODELING THE LOWEST 1 KM OF THE ATMOSPHERE

7. Presented at

8. Author(s)/Editor(s)

W.S.Lewellen

9. Date

November 1981

10. Author's/Editor's Address

Aeronautical Research Associates of Princeton, Inc.
50 Washington Road, P.O. Box 2229
Princeton, New Jersey 08540, USA

11. Pages

88

12. Distribution Statement This document is distributed in accordance with AGARD policies and regulations, which are outlined on the Outside Back Covers of all AGARD publications.

13. Keywords/Descriptors

Lower atmosphere
Mathematical models
Micrometeorology
Turbulence

14. Abstract

The interdependence between the turbulent transport of mass, momentum, and energy through the lower levels of the atmosphere, and the distribution of wind, temperature, and species within this layer are reviewed. Particular emphasis is placed on models, either analytical or numerical, which have a basic theoretical foundation in turbulent transport modeling. The results of example model solutions are used to discuss such micrometeorological problems as: wind shear and turbulence around airports; the prediction of low-level clouds and fog; the dispersion of industrial pollutants; the interaction of electromagnetic radiation with turbulent fluctuations in humidity and temperature; and the evolution of organized features within the boundary layer.

This AGARDograph was prepared at the request of the Fluid Dynamics Panel of AGARD.

AGARDograph No.267 Advisory Group for Aerospace Research and Development, NATO MODELING THE LOWEST 1 KM OF THE ATMOSPHERE by W.S.Lewellen Published November 1981 88 pages The interdependence between the turbulent transport of mass, momentum, and energy through the lower levels of the atmosphere, and the distribution of wind, temperature, and species within this layer are reviewed. Particular emphasis is placed on models, either analytical or numerical, which have a basic theoretical foundation in turbulent transport modeling. The results P.T.O.	AGARD-AG-267 Lower atmosphere Mathematical models Micrometeorology Turbulence	AGARDograph No.267 Advisory Group for Aerospace Research and Development, NATO MODELING THE LOWEST 1 KM OF THE ATMOSPHERE by W.S.Lewellen Published November 1981 88 pages The interdependence between the turbulent transport of mass, momentum, and energy through the lower levels of the atmosphere, and the distribution of wind, temperature, and species within this layer are reviewed. Particular emphasis is placed on models, either analytical or numerical, which have a basic theoretical foundation in turbulent transport modeling. The results P.T.O.	AGARD-AG-267 Lower atmosphere Mathematical models Micrometeorology Turbulence
AGARDograph No.267 Advisory Group for Aerospace Research and Development, NATO MODELING THE LOWEST 1 KM OF THE ATMOSPHERE by W.S.Lewellen Published November 1981 88 pages The interdependence between the turbulent transport of mass, momentum, and energy through the lower levels of the atmosphere, and the distribution of wind, temperature, and species within this layer are reviewed. Particular emphasis is placed on models, either analytical or numerical, which have a basic theoretical foundation in turbulent transport modeling. The results P.T.O.	AGARD-AG-267 Lower atmosphere Mathematical models Micrometeorology Turbulence	AGARDograph No.267 Advisory Group for Aerospace Research and Development, NATO MODELING THE LOWEST 1 KM OF THE ATMOSPHERE by W.S.Lewellen Published November 1981 88 pages The interdependence between the turbulent transport of mass, momentum, and energy through the lower levels of the atmosphere, and the distribution of wind, temperature, and species within this layer are reviewed. Particular emphasis is placed on models, either analytical or numerical, which have a basic theoretical foundation in turbulent transport modeling. The results P.T.O.	AGARD-AG-267 Lower atmosphere Mathematical models Micrometeorology Turbulence

of example model solutions are used to discuss such micrometeorological problems as: wind shear and turbulence around airports; the prediction of low-level clouds and fog; the dispersion of industrial pollutants; the interaction of electromagnetic radiation with turbulent fluctuations in humidity and temperature; and the evolution of organized features within the boundary layer. This AGARDograph was prepared at the request of the Fluid Dynamics Panel of AGARD. ISBN 92-835-1407-6	of example model solutions are used to discuss such micrometeorological problems as: wind shear and turbulence around airports; the prediction of low-level clouds and fog; the dispersion of industrial pollutants; the interaction of electromagnetic radiation with turbulent fluctuations in humidity and temperature; and the evolution of organized features within the boundary layer. This AGARDograph was prepared at the request of the Fluid Dynamics Panel of AGARD. ISBN 92-835-1407-6
of example model solutions are used to discuss such micrometeorological problems as: wind shear and turbulence around airports; the prediction of low-level clouds and fog; the dispersion of industrial pollutants; the interaction of electromagnetic radiation with turbulent fluctuations in humidity and temperature; and the evolution of organized features within the boundary layer. This AGARDograph was prepared at the request of the Fluid Dynamics Panel of AGARD. ISBN 92-835-1407-6	of example model solutions are used to discuss such micrometeorological problems as: wind shear and turbulence around airports; the prediction of low-level clouds and fog; the dispersion of industrial pollutants; the interaction of electromagnetic radiation with turbulent fluctuations in humidity and temperature; and the evolution of organized features within the boundary layer. This AGARDograph was prepared at the request of the Fluid Dynamics Panel of AGARD. ISBN 92-835-1407-6

[redacted]

AGARD

NATO OTAN

7 RUE ANCELLE · 92200 NEUILLY-SUR-SEINE

FRANCE

Telephone 745[illegible] 26 · Telex 610176

[redacted]

AGARD does NOT hold stocks of AGARD publications at the above address for general distribution. Initial distribution of AGARD publications is made to AGARD Member Nations through the following National Distribution Centres. Further copies are sometimes available from these Centres, but if not may be purchased in Microfiche or Photocopy form from the Purchase Agencies listed below.

NATIONAL DISTRIBUTION CENTRES

BELGIUM
Coordonnateur AGARD – VSL
Etat-Major de la Force Aérienne
Quartier Reine Elisabeth
Rue d'Evere, 1140 Bruxelles

CANADA
Defence Science Information Services
Department of National Defence
Ottawa, Ontario K1A 0K2

DENMARK
Danish Defence Research Board
Østervoldgades Kaserne
Copenhagen Ø

FRANCE
O.N.E.R.A. (Direction)
29 Avenue de la Division Leclerc
92320 Châtillon sous Bagneux

GERMANY
Fachinformationszentrum Energie,
Physik, Mathematik GmbH
Kernforschungszentrum
D-7514 Eggenstein-Leopoldshafen 2

GREECE
Hellenic Air Force General Staff
Research and Development Directorate
Holargos, Athens

ICELAND
Director of Aviation
c/o Flugrad
Reykjavik

ITALY
Aeronautica Militare
Ufficio del Delegato Nazionale all'AGARD
3, Piazzale Adenauer
Roma/EUR

LUXEMBOURG
See Belgium

NETHERLANDS
Netherlands Delegation to AGARD
National Aerospace Laboratory, NLR
P.O. Box 126
2600 A.C. Delft

NORWAY
Norwegian Defence Research Establishment
Main Library
P.O. Box 25
N-2007 Kjeller

PORTUGAL
Direcção do Serviço de Material
da Força Aérea
Rua da Escola Politécnica 42
Lisboa
Attn: AGARD National Delegate

TURKEY
Department of Research and Development (ARGE)
Ministry of National Defence, Ankara

UNITED KINGDOM
Defence Research Information Centre
Station Square House
St. Mary Cray
Orpington, Kent BR5 3RE

UNITED STATES
National Aeronautics and Space Administration (NASA)
Langley Field, Virginia 23365
Attn: Report Distribution and Storage Unit

THE UNITED STATES NATIONAL DISTRIBUTION CENTRE (NASA) DOES NOT HOLD STOCKS OF AGARD PUBLICATIONS, AND APPLICATIONS FOR COPIES SHOULD BE MADE DIRECT TO THE NATIONAL TECHNICAL INFORMATION SERVICE (NTIS) AT THE ADDRESS BELOW.

PURCHASE AGENCIES

Microfiche or Photocopy

National Technical
Information Service (NTIS)
5285 Port Royal Road
Springfield
Virginia 22161, USA

Microfiche

Space Documentation Service
European Space Agency
10, rue Mario Nikis
75015 Paris, France

Microfiche

Technology Reports
Centre (DTIC)
[illegible]
St. Mary Cray
Orpington, Kent BR5 3RF
England

Requests for microfiche or photocopies of AGARD documents should include the AGARD serial number, title, author or editor, and publication date. Requests to NTIS should include the NASA accession report number. Full bibliographical references and abstracts of AGARD publications are given in the following journals:

Scientific and Technical Aerospace Reports (STAR)
published by NASA Scientific and Technical
[illegible]
[illegible] International Airport
[illegible], USA

Government Reports Announcements (GRA)
published by the National Technical
Information Services, Springfield
Virginia 22161, USA

Printed by Technical Editing and Reproduction Ltd
Harford House, 7–9 Charlotte St, London W1P 1HD

ISBN 92-835-1407-8